Effective toughness of heterogeneous materials

Thesis by
Chun-Jen Hsueh

In Partial Fulfillment of the Requirements for the
degree of
Doctor of Philosophy

CALIFORNIA INSTITUTE OF TECHNOLOGY
Pasadena, California

2017
Defended May 15, 2017

Chun-Jen Hsueh
ORCID: 0000-0001-6522-4505

ACKNOWLEDGEMENTS

First, I would like to express my deep appreciation for my advisor, Prof. Kaushik Bhattacharya, for his guidance and support. I learned a lot on doing research, finding good problems, and setting goals. His creative thinking always makes our discussions on research fruitful. In addition to his guidance in academy, he is also a mentor in my life. He shares his valuable life experience such as being a husband and father and it really helps me a lot. I am very thankful to my chair of committee, Prof. Guruswami Ravichandran. He helps me a lot on my research especially on the experimental side. He always encourages me to try any idea I have. Although he is not officially my advisor, I always feel like I have two advisors. I would like to thank Prof. Blaise Bourdin for his help on numerical studies. I have learned lots of numerical and coding skills from him. He also makes me feel at home when I work at Louisiana State University. I would like to thank Prof. Katherine Faber for her insightful suggestions on material science perspective. I really enjoyed working with her and her lab members. I would like to thank Prof. Chiara Daraio for being my committee and providing valuable feedback on my work.

I have been very blessed to work in the fracture mechanics group and the Kaushik-Ravi group. I want to thank the members of fracture mechanics group and Kaushik-Ravi group: Neal Brodnik, Matthew Johnson, Louisa Avellar, Kimberley A. Mac Donald, Stella Brach, Nha V. Tran, Erwan Tanné, Andrew W. Richards, Bharat P. Penmecha, Jacob K. Notbohm, Ha T. Giang, Charles S. Wojnar, Xin C. Wang, Michael B. Rauls, Srivatsan Hulikal Sampath Kumaran, Victoria Stolyar Richmond, Vinamra Agrawal, Lincoln Collins, Hayden Burgoyne, Dingyi Sun, Paul Plucinsky, Jin Yang, Paul Mazur, Christian Kettenbeil, Matthew Newman, Zach Sternberger, Victoria (Tori) Lee, Ying Shi Teh, Tomoyuki Oniyama, M. Zubaer Hossain, Aaron Stebner, Likun Tan, Mauricio Ponga, Pierre-Luigi Cesano, Dipankar Ghosh, Gal Shmuel, Owen Kingstedt, Nikhil Karanjgaokar, Noy Cohen, Swarnava Ghosh, Michael Mello, and Petros Arakelian. Thank you all for your help and insightful discussions throughout my PhD.

I also want to thank all my friends in the Association of Caltech Taiwanese (ACT). I had a lot of good times with my friends in ACT, especially Hsieh-

Chen Tsai, Ho-Cheng Tsai, Yu-Hung Lai, Albert Chern, and Ying-Yu Ho. My life at Caltech is more enjoyable and unforgettable because of you guys.

Finally and the most importantly, I am deeply grateful to my family for their support especially my wife, Chen-Yi (Jessie) Chang. I could not had the achievements I have right now without her patience and endless support.

ABSTRACT

Composite materials are widely used because of their extraordinary performance. It is understood that the heterogeneity / microstructure can dramatically affect the effective behavior of materials. Although there is a well-developed theory for this relation in elasticity, there is no similar theory in fracture mechanics. Therefore, we use theoretical, numerical, and experimental approaches to study the relationship between heterogeneity / microstructure and the effective fracture behavior in this thesis.

We use the surfing boundary condition, a boundary condition that ensures the macroscopic steady crack growth, and then define the effective toughness of heterogeneous materials as the peak energy release rate during crack propagation. We also use the homogenization theory to prove that the effective J-integral in heterogeneous materials is well defined, and that it can be calculated by the homogenized stress and strain field.

In order to study the relationship between heterogeneities and effective toughness, we first use the semi-analytical method under the assumption of small elastic contrast to study selected examples. For strong heterogeneities, we use the phase field fracture method to study the crack propagation numerically. We then optimize the microstructure with respect to effective stiffness and effective toughness in a certain class of microgeometries. We show that it is possible to significantly enhance toughness without significant loss of stiffness. We also design materials with asymmetric toughness.

We develop a new experimental configuration that can measure the effective toughness of specimens with arbitrary heterogeneities. We confirm through preliminary tests that the heterogeneities can enhance the effective toughness.

Besides study the effective toughness of heterogeneous materials, we also study a model problem of peeling a thin sheet from a heterogeneous substrate. We develop a methodology to systematically optimize microstructure.

PUBLISHED CONTENT AND CONTRIBUTIONS

[1] C.-J. Hsueh and K. Bhattacharya. "Optimizing microstructure for toughness: The model problem of peeling". In: *To be submitted* (2017).
C.-J. Hsueh proposed the original idea and performed the algorithm.

[2] C.-J. Hsueh, N. Brodnik, and M. T. Johnson. "A novel method to perform the grid method in order to reduce the measurement bias". In: *To be submitted* (2017).
C.-J. Hsueh performed the experiments and analyzed the data.

[3] C.-J. Hsueh, G. Ravichandran, and K. Bhattacharya. "Investigating the Effective Fracture Toughness of Heterogeneous Materials". In: *Fracture, Fatigue, Failure and Damage Evolution, Volume 8*. Springer, 2017, pp. 15–20. DOI: 10.1007/978-3-319-42195-7_3. URL: http://link.springer.com/chapter/10.1007/978-3-319-42195-7_3.
C.-J. Hsueh performed the experiments and analyzed the data.

[4] C.-J. Hsueh and K. Bhattacharya. "Homogenization and Path Independence of the J-Integral in Heterogeneous Materials". In: *Journal of Applied Mechanics* 83.10 (2016), p. 101012. DOI: 10.1115/1.4034294. URL: http://appliedmechanics.asmedigitalcollection.asme.org/article.aspx?articleid=2540451.
C.-J. Hsueh derived the main result of this paper.

[5] C.-J. Hsueh, G. Ravichandran, and K. Bhattacharya. "Measuring the Effective Fracture Toughness of Heterogeneous Materials". In: *Fracture, Fatigue, Failure and Damage Evolution, Volume 8*. Springer, 2016, pp. 151–155. DOI: 10.1007/978-3-319-21611-9_19. URL: http://link.springer.com/chapter/10.1007/978-3-319-21611-9_19.
C.-J. Hsueh performed the experiments and analyzed the data.

[6] M. Z. Hossain, C.-J. Hsueh, B. Bourdin, and K. Bhattacharya. "Effective toughness of heterogeneous media". In: *Journal of the Mechanics and Physics of Solids* 71 (2014), pp. 15–32. DOI: http://dx.doi.org/10.1016/j.jmps.2014.06.002. URL: http://www.sciencedirect.com/science/article/pii/S0022509614001215.
C.-J. Hsueh done the calculation of the semi-analytical method.

CONTENTS

LIST OF FIGURES

LIST OF TABLES

Number *Page*

Chapter 1

INTRODUCTION

Brittle fracture can lead to sudden, unexpected, and catastrophic failures. One of the most famous examples is the failure of the warship SS Schenectady in 1943 where brittle fracture broke the hull almost in two halves [70]. The field of fracture mechanics seeks to understand the causes of such failures and design strategies to engineer around them.

Fracture mechanics in homogeneous materials has been well-developed in the early and mid 20th century. In 1921, Alan A. Griffith studied brittle fracture propagation and proposed a criteria that states that a crack propagates in homogeneous materials when the energy release rate $G := -\frac{\partial \Pi}{\partial a}$ reaches the material toughness G_c, where Π is the potential energy and a is the crack length [37]. This idea is the cornerstone of fracture mechanics. In 1957, George R. Irwin introduced the stress intensity factor K, which is one of the most widely used parameters in fracture mechanics [42]. This stress intensity factor can be related to the energy release rate by $G = \frac{K^2}{E}$ in homogeneous materials. In 1968, James R. Rice proposed an integral (the J-integral) that can be used to calculate the energy release rate [74]. Moreover, this integral is particularly useful because it is path-independent in homogeneous materials so one can choose the integral path which is most convenient to evaluate the integrand.

In the late 20th century, many composite materials were developed because of their outstanding performance. As a result, there is extensive literature on fracture toughness of composite materials [10, 15, 23–25, 27, 40, 51, 81]. However, these works generally focus on particular microstructures, there is no general theory for fracture mechanics in heterogeneous materials yet. Additionally, while there are well-developed homogenization and optimization theories in fields such as elasticity, there are no similar approaches in fracture mechanics. For example, the J-integral is path-independent in homogeneous materials. However, most of the materials are heterogeneous at the microscale. Typically, the scale of heterogeneities is small compared to the engineering object of interest. Therefore, a com-

mon approach is the use of the homogenization theory to define an effective (macroscopic homogeneous) elastic material, then apply elasticity theory and the J-integral to this effective material. Unfortunately, it is not clear whether the J-integral computed with the stress and the strain associated with the heterogeneous medium will converge to the J-integral computed with the stress and the strain associated with the effective medium as the contour becomes very large.

Measuring crack propagation in arbitrary heterogeneous specimens is a challenging problem. Most fracture tests are designed for homogeneous specimens, for example, the compact tension (CT) test [79], a pre-crack rectangular specimen with two circular holes where the concentrate loads apply on it. The center cracked tension (CCT) test [22], a rectangular specimen with a horizontal pre-crack in the center subject to uniform loading on the top and the bottom, and the single edge notch tension (SENT) test [78], a rectangular specimen with a horizontal pre-crack on the side subject to uniform loading on the top and the bottom. These test methods use specimens with particular dimension so the relationship between the measured force and the stress intensity factor is pre-determined. Thus, one can easily calculate the stress intensity factor from the measured force. There are also some test methods that work for particular heterogeneous specimens, such as double cantilever beam (DCB) test for the laminar materials [52]. This method uses the double cantilever beam test to study the delamination of heterogeneous laminar specimens. However, general methods for measuring the toughness of arbitrary heterogeneous specimens remain open.

More recently, the improvement of 3D printing and other additive manufacturing methods gives engineers and scientists the ability to carefully control the microstructure of materials [56, 60, 76]. Therefore, it is urgent to understand the relation between microstructure of materials and effective fracture toughness because it can lead the design of microstructure and accelerate the development of better engineering materials. Fortunately, the numerical methods to study fracture mechanics in heterogeneous materials have developed rapidly in the last two decades [5–7, 26, 29, 30, 53, 64, 66, 69]. As computers have become faster and inexpensive, it is useful to use these numerical methods to assist in the study of the relation between the

microstructure of the material and effective toughness. All of these issues motivate this thesis.

We begin in Chapter 2 by recalling some background and reviewing the literature in fracture mechanics. We introduce the surfing boundary condition (a boundary condition that ensures a macroscopic steady crack growth in heterogeneous materials) and give a robust definition of the effective toughness of arbitrary heterogeneous materials in Chapter 3. We prove the existence of effective J-integral in heterogeneous materials and show that it can be calculated by the homogenized stress and strain field in Chapter 4. We study the toughening mechanism in elastic heterogeneous materials by using the semi-analytical method in Chapter 5. We use the phase field fracture method to study the toughening mechanism in heterogeneous material numerically and optimize the microstructure in a certain class in Chapter 6. We study the toughening mechanism experimentally in Chapter 7. We then propose an adjoint method to topologically optimize the microstructure in a model problem (the peeling problem) in Chapter 9. We recall the main results of this thesis and point out the future directions in Chapter 10.

Chapter 2

BACKGROUND

In this chapter, we review some important background in linear elastic fracture mechanics. In section 2.1, we start by reviewing the important development in linear elastic fracture mechanics. In section 2.2, we recall the asymptotic analysis of the elastic field in the vicinity of the crack front. In the section 2.3, we show that the J-integral can measure the energy release rate. In the section 2.4, we use the configurational force balance to show that J-integral is path-independent in homogeneous materials. In section 2.5, we review the literature of fracture mechanics in heterogeneous materials. In section 2.6, we discuss the numerical methods in fracture mechanics. In the last section, we introduce some of experimental methods.

2.1 A brief history of linear elastic fracture mechanics

The history of fracture mechanics can be traced back to a landmark paper in the early 20th century where Griffith proposed a criterion for the crack propagation in brittle materials based on the theorem of minimum potential energy [37]. This criteria stated that the crack propagates if it is energetically favorably, i.e., if the total energy can be decreased, the crack grows. The energy release rate G is defined as the decrease of potential energy subject to crack growth

$$G := -\frac{d\Pi}{da}, \tag{2.1}$$

where Π is the potential energy and a is the crack length. The critical energy release rate G_c is defined as the required energy to create the crack faces

$$G_c := 2\gamma, \tag{2.2}$$

where γ is the surface energy. Therefore, the Griffith's criterion can be represented as

$$G = G_c. \tag{2.3}$$

He then combined this idea with the prior analysis of Inglis to show that the critical load to break a plate with a crack in it is inversely proportional

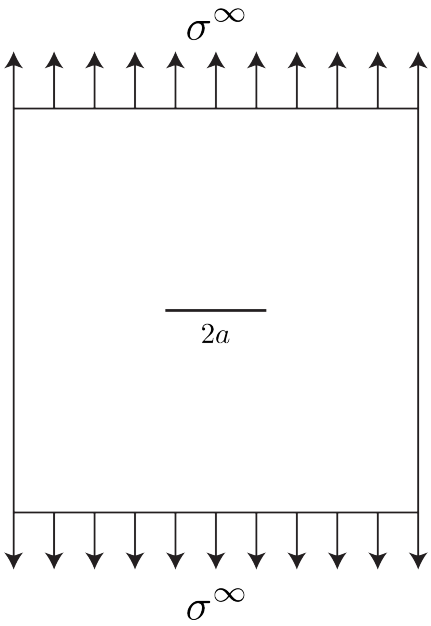

Figure 2.1: An infinite plate containing a crack with length $2a$ subject to far-field tensile stress σ^∞

to the square root of the crack length. Inglis derived the stress state at the major axis tip of an elliptical hole in an infinity plate as shown in Figure 2.2 [41]. He then took the limit of minor axis approaches zero ($b \to 0$ in Figure 2.2) and used this model to approach a sharp corner or a notch. He found that the stress concentration is singular when the minor axis approaches zero.

Instead of using an ellipse hole to approach a crack, Westergaard used complex analysis to derive the analytical solution of a crack directly [84]. He found the Airy stress function of complex numbers that is the solution for the stress field in an infinite plate containing a crack. By using his approach, the Airy stress function is amazingly compact. For example, the Airy stress potential for an infinite plate containing a crack with length $2a$ subject to far-field tensile stress σ^∞ as shown in Figure 2.1 is

$$\phi = \sigma^\infty \sqrt{z^2 - a^2} - \sigma^\infty z \iff \phi' = \frac{\sigma^\infty z}{\sqrt{z^2 - a^2}} - \sigma^\infty, \tag{2.4}$$

where $z = x_1 + ix_2$. The stress state can be derived from

$$\sigma_{11} = \mathrm{Re}\,\phi' - x_2 \mathrm{Im}\,\phi'' \tag{2.5}$$

$$\sigma_{22} = \mathrm{Re}\,\phi' + x_2 \mathrm{Im}\,\phi'' \tag{2.6}$$

$$\sigma_{12} = -\mathrm{Re}\,\phi''. \tag{2.7}$$

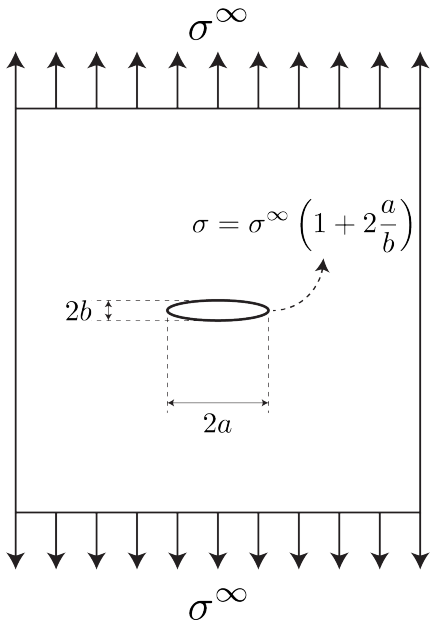

Figure 2.2: An infinite plate containing an ellipse subject to far-field tensile stress σ^∞

About two decades later, Irwin proposed the concept of the stress intensity factor [42]. Since he was interested in the region near the crack tip, he substituted

$$z = a + re^{i\theta} \tag{2.8}$$

into Westergaard solution, equation (2.4) - (2.7), and assumed that $r \ll a$. As a result, the stress near the crack tip becomes

$$\sigma_{11} = \frac{\sigma^\infty\sqrt{\pi a}}{\sqrt{2\pi r}}\cos\frac{\theta}{2}\left(1 - \sin\frac{\theta}{2}\sin\frac{3\theta}{2}\right) \tag{2.9}$$

$$\sigma_{22} = \frac{\sigma^\infty\sqrt{\pi a}}{\sqrt{2\pi r}}\cos\frac{\theta}{2}\left(1 + \sin\frac{\theta}{2}\sin\frac{3\theta}{2}\right) \tag{2.10}$$

$$\sigma_{12} = \frac{\sigma^\infty\sqrt{\pi a}}{\sqrt{2\pi r}}\cos\frac{\theta}{2}\sin\frac{\theta}{2}\cos\frac{3\theta}{2}. \tag{2.11}$$

Note that there is a common expression $\sigma^\infty\sqrt{\pi a}$ in the numerators of equation (2.9) - (2.11). Furthermore, this combination of a and σ^∞ completely determine the stress state near the crack tip. Irwin recognized this and first used the term stress intensity factor to describe the expression. Therefore,

the stress near the crack tip becomes

$$\sigma_{11} = \frac{K_I}{\sqrt{2\pi r}} \cos\frac{\theta}{2}\left(1 - \sin\frac{\theta}{2}\sin\frac{3\theta}{2}\right) \tag{2.12}$$

$$\sigma_{22} = \frac{K_I}{\sqrt{2\pi r}} \cos\frac{\theta}{2}\left(1 + \sin\frac{\theta}{2}\sin\frac{3\theta}{2}\right) \tag{2.13}$$

$$\sigma_{12} = \frac{K_I}{\sqrt{2\pi r}} \cos\frac{\theta}{2}\sin\frac{\theta}{2}\cos\frac{3\theta}{2}, \tag{2.14}$$

where $K_I = \sigma^\infty\sqrt{\pi a}$ is the stress intensity factor. According to equation (2.13), the stress intensity factor can be calculated by

$$K_I = \lim_{r\to 0}\left(\sqrt{2\pi r}\,\sigma_{22}|_{\theta=0}\right). \tag{2.15}$$

Moreover, this stress intensity factor can be related to the energy release rate in equation (2.1) by

$$G = \frac{K_I^2}{E}, \tag{2.16}$$

where E is the stiffness. This stress intensity factor has emerged as one of the most widely used parameters in fracture mechanics.

Later, in 1968, Rice introduced the J-integral, which is a path-independent integral that can calculate the energy release rate [74]. The J-integral can be written as

$$J = \int_\Gamma t_i\left(W\delta_{ij} - \frac{\partial u_k}{\partial x_i}\sigma_{kj}\right)n_j\,ds, \tag{2.17}$$

where W is the elastic energy density, δ the Kronecker delta function, $\frac{\partial u}{\partial x}$ the displacement gradient, σ the stress, n the outward normal vector of the contour Γ, t is the normal vector tangential to the crack propagation direction. This integral is extremely useful because it is independent of the contour Γ in homogeneous materials and one can choose a contour which is most convenient to evaluate the integrand.

2.2 Linear elastic fracture mechanics

Although a general crack face and crack front can be curved, we focus on the vicinity of the crack front and focus on finding the solutions locally in this vicinity. Mathematically, this operation is the asymptotic analysis of the elastic solution near the crack front. First, we set the coordinate as shown in Figure 2.3. The x_1 direction is the crack propagation direction and the x_3 direction is tangential to the crack front.

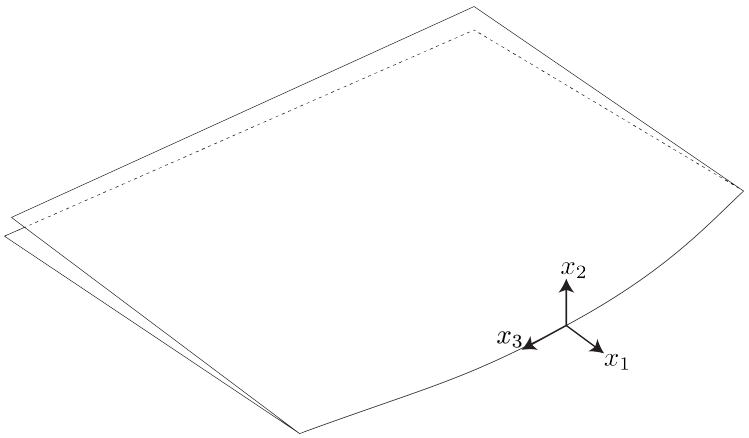

Figure 2.3: Coordinates on the crack tip

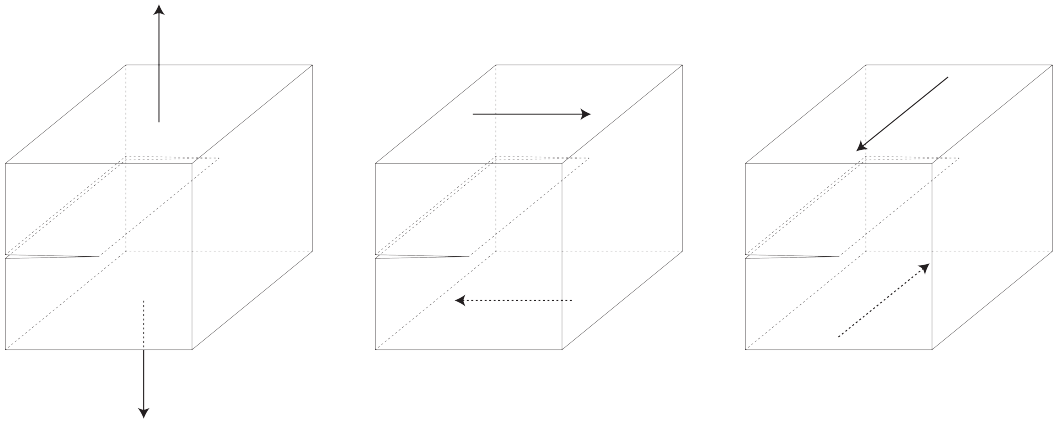

(a) mode-I (b) mode-II (c) mode-III

Figure 2.4: Modes of fracture

In the asymptotic approach, the crack becomes a semi-infinite crack with a straight front in an infinite solid deforming in plane strain. Typically, one can decouple the loading into the following three modes as shown in Figure 2.4: mode-I (in plane symmetric loading), mode-II (in plane anti-symmetric loading), and mode-III (out of plane loading).

We first represent the stress by the Airy stress potential in polar coordinates.

$$\sigma_{rr} = \frac{1}{r}\frac{\partial \phi}{\partial r} + \frac{1}{r^2}\frac{\partial^2 \phi}{\partial \theta^2} \tag{2.18}$$

$$\sigma_{\theta\theta} = \frac{\partial^2 \phi}{\partial r^2} \tag{2.19}$$

$$\sigma_{r\theta} = -\frac{\partial}{\partial r}\left(\frac{\partial \phi}{\partial \theta}\right). \tag{2.20}$$

The traction-free boundary condition on the crack face is

$$\sigma_{\theta\theta}\Big|_{r,\theta=\pm\pi} = \sigma_{r\theta}\Big|_{r,\theta=\pm\pi} = 0. \tag{2.21}$$

We use the William's expansion ansatz [85]

$$\phi(r,\theta) = r^{\lambda+2} f(\theta). \tag{2.22}$$

Substitute equation (2.22) into the Airy stress biharmonic equation gives

$$\lambda^2(\lambda+1)^2 f(\theta) + \left[\lambda^2 + (\lambda+2)^2\right] f''(\theta) + f''''(\theta) = 0. \tag{2.23}$$

The general solution of equation (2.23) is

$$A_1 \cos\lambda\theta + A_2 \cos(\lambda+2)\theta + B_1 \sin\lambda\theta + B_2 \sin(\lambda+2)\theta, \tag{2.24}$$

where A_1, A_2, B_1, and B_2 are unknown constants. For the mode-I loading (symmetric loading), the solution is symmetric. Thus, it requires that $B_1 = B_2 = 0$. Since the stress can be represented as

$$\sigma_{rr} = r^{\lambda}\left[(\lambda+2)f(\theta) + f''(\theta)\right] \tag{2.25}$$

$$\sigma_{\theta\theta} = r^{\lambda}(\lambda+2)(\lambda+1)f(\theta) \tag{2.26}$$

$$\sigma_{r\theta} = -r^{\lambda}(\lambda+1)f(\theta), \tag{2.27}$$

the traction free condition gives

$$\sigma_{\theta\theta}\Big|_{r,\theta=\pm\pi} = 0 \quad \Longrightarrow \quad (A_1 + A_2)\cos\lambda\pi = 0 \tag{2.28}$$

$$\sigma_{r\theta}\Big|_{r,\theta=\pm\pi} = 0 \quad \Longrightarrow \quad (\lambda A_1 + (\lambda+2)A_2)\sin\lambda\pi = 0. \tag{2.29}$$

In order to satisfy equation (2.28), we need

$$A_1 + A_2 = 0 \quad \text{or} \quad \lambda = \cdots, -\frac{3}{2}\pi, -\frac{1}{2}\pi, \frac{1}{2}\pi, \cdots. \tag{2.30}$$

Similarly, equation (2.29) gives

$$(\lambda A_1 + (\lambda+2)A_2) = 0 \quad \text{or} \quad \lambda = \cdots, -2\pi, -1\pi, +1\pi, \cdots. \tag{2.31}$$

However, there is an additional restriction on λ. Since we know that the stress and strain are $\sigma \sim r^{\lambda}$ and $\varepsilon \sim r^{\lambda}$, the energy in a disk of radius R centered at the crack tip is

$$\int_0^R \int_0^{2\pi} \frac{1}{2}\sigma_{ij}\varepsilon_{ij} r\, d\theta dr \sim R^{2\lambda+2}. \tag{2.32}$$

Therefore, the requirement that the energy be bounded gives

$$\lambda > -1. \tag{2.33}$$

Finally, using equation (2.30), (2.31), and (2.33) gives the general solution of mode-I fracture which is

$$\begin{aligned}\phi(r,\theta) = C_{-\frac{1}{2}} r^{\frac{3}{2}} \left(\cos\frac{\theta}{2} + \frac{1}{3}\cos\frac{3\theta}{2}\right) + C_0 r^2 (1-\cos 2\theta) \\ + C_{\frac{1}{2}} r^{\frac{5}{2}} \left(\cos\frac{\theta}{2} - \frac{1}{5}\cos\frac{5\theta}{2}\right) + \cdots,\end{aligned} \tag{2.34}$$

where $C_{-\frac{1}{2}}, C_0, C_{\frac{1}{2}}, \cdots$ are undetermined constants. The corresponding stress is

$$\begin{aligned}\begin{bmatrix}\sigma_{rr}\\ \sigma_{\theta\theta}\\ \sigma_{r\theta}\end{bmatrix} = \frac{C_{-\frac{1}{2}}}{4}\frac{1}{\sqrt{r}}\begin{bmatrix}-\cos\frac{3\theta}{2} + 5\cos\frac{\theta}{2}\\ \cos\frac{3\theta}{2} + 3\cos\frac{\theta}{2}\\ \sin\frac{\theta}{2} + \sin\frac{3\theta}{2}\end{bmatrix} + 4C_0\begin{bmatrix}\cos^2\theta\\ \sin^2\theta\\ -\sin\theta\cos\theta\end{bmatrix} \\ + \frac{3C_{\frac{1}{2}}}{4}\sqrt{r}\begin{bmatrix}3\cos\frac{\theta}{2} + \cos\frac{5\theta}{2}\\ 5\cos\frac{\theta}{2} - \cos\frac{5\theta}{2}\\ \sin\frac{\theta}{2} - \sin\frac{5\theta}{2}\end{bmatrix} + \cdots.\end{aligned} \tag{2.35}$$

Since we are interested in the vicinity of the crack front, the leading term in equation (2.35) dominates. Therefore, we can neglect the high order terms. Furthermore, the stress intensity factor is defined as $K_I = \lim_{r\to 0}\sqrt{2\pi r}\sigma_{\theta\theta}\Big|_{\theta=0}$. Thus, we have $C_{-\frac{1}{2}} = \frac{K_I}{\sqrt{2\pi}}$. Finally, equation (2.35) becomes

$$\begin{bmatrix}\sigma_{rr}\\ \sigma_{\theta\theta}\\ \sigma_{r\theta}\end{bmatrix} = \frac{K_{II}}{\sqrt{2\pi r}}\frac{1}{4}\begin{bmatrix}-\cos\frac{3\theta}{2} + 5\cos\frac{\theta}{2}\\ \cos\frac{3\theta}{2} + 3\cos\frac{\theta}{2}\\ \sin\frac{\theta}{2} + \sin\frac{3\theta}{2}\end{bmatrix}. \tag{2.36}$$

We can use similar procedures to derive the stress state in mode-II where $A_1 = A_2 = 0$ and $K_{II} = \lim_{r\to 0}\sqrt{2\pi r}\sigma_{r\theta}\Big|_{\theta=0}$. The stress state for mode-II is

$$\begin{bmatrix}\sigma_{rr}\\ \sigma_{\theta\theta}\\ \sigma_{r\theta}\end{bmatrix} = \frac{K_I}{\sqrt{2\pi r}}\frac{1}{4}\begin{bmatrix}-5\sin\frac{\theta}{2} + 3\sin\frac{3\theta}{2}\\ -3\sin\frac{\theta}{2} - 3\sin\frac{3\theta}{2}\\ \cos\frac{\theta}{2} + 3\cos\frac{3\theta}{2}\end{bmatrix}. \tag{2.37}$$

Note that the energy release rate can be represented by stress intensity factor

$$G = \frac{K_I^2 + K_{II}^2}{E'} + \frac{K_{III}^2}{2\mu}, \tag{2.38}$$

where $E' = \frac{E}{1-\nu^2}$ for plane strain and $E' = E$ for plane stress.

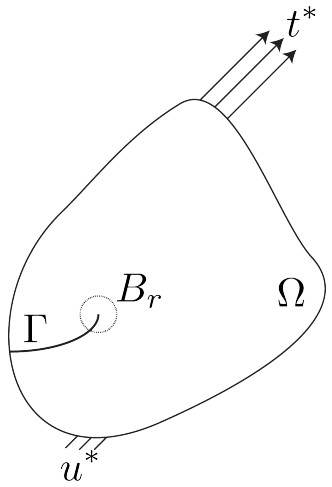

Figure 2.5: An elastic solid Ω containing a crack Γ

2.3 J-integral

Consider an elastic solid Ω containing a crack Γ of length a as shown in Figure 2.5. The energy of this system is

$$\Pi = \lim_{r\to 0} \int_{\Omega\setminus B_r} W(\nabla u) dV - \int_{\partial_2\Omega} t_i^* u_i dA, \tag{2.39}$$

where W is the elastic energy density. We wish to vary the crack length a and observe the energy change:

$$\frac{d\Pi}{da} = \frac{d}{da}\left\{\lim_{r\to 0} \int_{\Omega\setminus B_r} W(\nabla u) dV - \int_{\partial_2\Omega} t_i^* u_i dA\right\}. \tag{2.40}$$

By applying the Reynolds Transportation Theory ($\frac{d}{dt}\int_\Omega f\ dV = \int_\Omega \dot{f}\ dV + \int_{\partial\Omega} f(\dot{\mathbf{s}}\cdot\mathbf{n})dA$) to the equation above, we obtain

$$\begin{aligned}\frac{d\Pi}{da} = \lim_{r\to 0}\Bigg\{ &\int_{\partial(\Omega\setminus B_r)} \frac{\partial W}{\partial u_{i,j}} n_j u_i' dA - \int_{\Omega\setminus B_r} \left(\frac{\partial W}{\partial u_{i,j}}\right)_{,j} u_i' dV \\ &+ \int_{\partial(\Omega\setminus B_r)} W\xi_p n_p dA - \int_{\partial_2\Omega} t_i^* u_i' dA\Bigg\},\end{aligned} \tag{2.41}$$

where $(\ )' := \frac{d(\ )}{da}$, ξ_i is the normal vector parallel to the crack propagation directio as shown in Figure 2.6 and n is the outward normal vector. Since the system is in equilibrium, we have

$$\left(\frac{\partial W}{\partial u_{i,j}}\right)_{,j} = 0 \quad \text{in } \Omega\setminus\Gamma, \tag{2.42}$$

$$\frac{\partial W}{\partial u_{i,j}} n_j = t_i^* \quad \text{on } \partial_2\Omega. \tag{2.43}$$

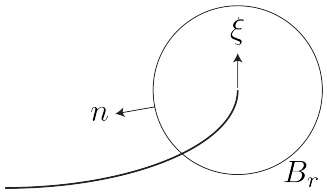

Figure 2.6: The tangential vector and normal vector

Therefore, equation (2.41) becomes

$$\frac{d\Pi}{da} = \lim_{r\to 0}\int_{\partial B_r} -W\xi_p n_p - \frac{\partial W}{\partial u_{i,j}} n_j u_i' dA \tag{2.44}$$

$$= \lim_{r\to 0}\int_{\partial B_r} -W\xi_p n_p + \frac{\partial W}{\partial u_{i,j}} n_j u_{i,k}\xi_k dA. \tag{2.45}$$

Finally, the J-integral is defined as

$$J := -\frac{d\Pi}{da} = \lim_{r\to 0}\int_{\partial B_r} \left[W\delta_{pq} - u_{k,p}\frac{\partial W}{\partial u_{k,q}}\right]\xi_p n_q dA, \tag{2.46}$$

where δ is the Kronecker delta function. Note that the terms between square brackets in equation (2.46) are the configurational stress tensor (Eshelby stress tensor).

2.4 Path-independency of J-integral

Suppose we have the elasticity energy as follow:

$$I(u) = \int_\Omega W(\nabla u, x)dx, \tag{2.47}$$

where $W(\nabla, x)$ is the inhomogeneous elastic energy density. By using the inner variation (variation of independent variable $z = z^s(x)$), we define the function

$$f(s) := I(u(z^s)) = \int_\Omega W(\nabla_x u(z^s), x)dx = \int_\Omega W\left(F_{ik}\Big|_{z^s}\frac{\partial z_k^s}{\partial x_j}, x\right)dx, \tag{2.48}$$

where $F := \nabla_x u(x)$. Assume $z = z^s(x)$ is invertible so we can have $x = x^s(z)$. Thus, we use the change the independent variable technique to get

$$f(s) = \int_\Omega W\left(F_{ik}\Big|_{z^s}\frac{\partial z_k^s}{\partial x_j}, x\right)dx = \int_\Omega W\left(F_{ik}\Big|_z\left[(\nabla_z x^s)^{-1}\right]_{kj}, x^s(z)\right)Jdz, \tag{2.49}$$

where $J := \det(\nabla_z x^s)$. Then,

$$\dot{J} = \frac{\partial(\det\nabla_z x^s)}{\partial s} = (\det\nabla_z x^s)(\nabla_z x^s)^{-T} : \frac{\partial(\nabla_z x)}{\partial s} = J\frac{\partial z_j}{\partial x_i}\frac{\partial}{\partial s}\left(\frac{\partial x_i^s}{\partial z_j}\right), \tag{2.50}$$

where $\dot{(\,)} := \frac{\partial}{\partial s}(\,)$. We also know that

$$\frac{\partial}{\partial s}\left(A^{-1}\right) = -A^{-1}\dot{A}A^{-1}. \tag{2.51}$$

Therefore, the first derivative is

$$\begin{aligned} f'(s) = \int_\Omega \Bigg\{ & \frac{\partial W}{\partial F_{ij}} F_{ik}\Big|_z \frac{\partial}{\partial s}\left[(\nabla_z x^s)^{-1}\right]_{kj} + \frac{\partial^* W}{\partial^* x_i^s}\frac{\partial x_i^s}{\partial s} \\ & + W\left[(\nabla_z x^s)^{-1}\right]_{ji} \frac{\partial}{\partial s}\left(\frac{\partial x_i^s}{\partial z_j}\right)\Bigg\} J dz \qquad (2.52) \\ = \int_\Omega \Bigg\{ & -\frac{\partial W}{\partial F_{ij}} F_{ik}\Big|_z \left[(\nabla_z x^s)^{-1}\right]_{kp}\left(\frac{\partial \dot{x}_p^s}{\partial z_q}\right)\left[(\nabla_z x^s)^{-1}\right]_{qj} + \frac{\partial^* W}{\partial^* x_i^s}\dot{x}_i^s \\ & + W\left[(\nabla_z x^s)^{-1}\right]_{ji}\left(\frac{\partial \dot{x}_i^s}{\partial z_j}\right)\Bigg\} J dz \qquad (2.53) \\ = \int_\Omega \Bigg\{ & \frac{\partial}{\partial z_q}\left(\frac{\partial W}{\partial F_{ij}} F_{ik}\Big|_z \left[(\nabla_z x^s)^{-1}\right]_{kp}\left[(\nabla_z x^s)^{-1}\right]_{qj}\right) + \frac{\partial^* W}{\partial^* x_p^s} \\ & - \frac{\partial}{\partial z_j}\left(W\left[(\nabla_z x^s)^{-1}\right]_{jp}\right)\Bigg\}\dot{x}_p^s J dz, \qquad (2.54) \end{aligned}$$

where $\frac{\partial^*}{\partial^* x}$ is the explicit derivative due to x. Therefore, the first order variation is

$$\begin{aligned} f'(0) &= \int_\Omega \left\{\frac{\partial}{\partial z_j}\left(\frac{\partial W}{\partial F_{ij}}F_{ik}\right) + \frac{\partial^* W}{\partial^* x_k} - \frac{\partial W}{\partial z_k}\right\}\dot{x}_k dz \qquad (2.55) \\ &= \int_\Omega \left\{\frac{\partial}{\partial x_j}\left(\frac{\partial W}{\partial F_{kj}}F_{ki}\right) + \frac{\partial^* W}{\partial^* x_i} - \frac{\partial}{\partial x_j}\left(W\delta_{ij}\right)\right\}\dot{x}_i dx \qquad (2.56) \\ &= \int_\Omega \left\{\frac{\partial}{\partial x_j}\left(\frac{\partial W}{\partial F_{kj}}F_{ki} - W\delta_{ij}\right) + \frac{\partial^* W}{\partial^* x_i}\right\}\dot{x}_i dx. \qquad (2.57) \end{aligned}$$

Finally, the Euler-Lagrange equation is

$$\frac{\partial}{\partial x_j}\left(W\delta_{ij} - \frac{\partial W}{\partial F_{kj}}F_{ki}\right) = \frac{\partial^* W}{\partial^* x_i}. \tag{2.58}$$

Note that equation (2.58) is the configurational force balance. Now consider the J-integral taking two different integration paths Γ_1 and Γ_2. Without loss of generality, we assume that Γ_2 is inside Γ_1. The difference between the different integration paths is

$$\begin{aligned} & \int_{\Gamma_1}\left(W\delta_{ij} - \frac{\partial W}{\partial F_{kj}}F_{ki}\right)\xi_i n_j ds - \int_{\Gamma_2}\left(W\delta_{ij} - \frac{\partial W}{\partial F_{kj}}F_{ki}\right)\xi_i n_j ds \qquad (2.59) \\ &= \int_{A(\Gamma_1,\Gamma_2)} \xi_i \frac{\partial}{\partial x_j}\left(W\delta_{ij} - \frac{\partial W}{\partial F_{kj}}F_{ki}\right) dA \qquad (2.60) \\ &= \int_{A(\Gamma_1,\Gamma_2)} \xi_i \frac{\partial^* W}{\partial^* x_i} dA, \qquad (2.61) \end{aligned}$$

where $A(\Gamma_1, \Gamma_2)$ is the area between the contours Γ_1 and Γ_2. From equation (2.61) we see that if the material between two contours is homogeneous, the J-integral evaluate on these two contours have the same value. Therefore, J-integral is path independent in homogeneous materials.

2.5 Fracture mechanics in heterogeneous materials

It is widely recognized that heterogeneity can have an influence on fracture toughness. This has motivated a significant body of work in the late 20th century.

Faber and Evans focused on the toughening mechanism by the second-phase particles which is pretty common in ceramics. They first studied the microcracking in the crack process zone and proposed an approximate analysis of the toughening mechanism by the microcracking [23]. Later, they studied the toughening mechanism due to the crack deflection (crack tilt or crack front twist) around second phase particles [24, 25]. He and Hutchinson studied a crack approaching the interface of elastically dissimilar materials [59]. They compared the energy release rate of a deflected crack and a penetrated crack. Gao and Rice used first-order perturbation analysis to study crack trapping by arrays of tough obstacles in two dimension [28]. Later, Gao studied the crack propagation in elastic heterogeneous materials [27] by the moduli-perturbation approach with the weight function [12]. Bower and Ortiz investigated the crack trapping and bridging by tough particles in three dimension [10]. They found out the crack can be trapped by tough particles. Moreover, the toughness may be further enhanced by the pinning particles on crack faces or frictional energy dissipation as particles are pulled out in the wake of the crack. In 1992, Hutchinson and Suo published a comprehensive study of the mixed mode cracking in layered materials [40].

Although there is a massive amount of literature analyzing the toughening mechanism due to heterogeneities, this literature usually focuses on particular microstructures. A general theory of fracture mechanics in heterogeneous materials is still absent.

2.6 Numerical methods

A crack is an evolving surface of discontinuity in the displacement field. The many numerical methods can mainly be classified into three cate-

gories.

The first category is the discontinuous Galerkin approach such as extended finite element methods. The feature of this category is that it has enhancements to the Galerkin method to embed the discontinuity. A common treatment is to add more basis function in the approximation space. In addition of classical polynomial shape function, a Heaviside step function can that adapt to the crack / discontinuity is common [3, 17, 20, 55]. However, the discontinuous displacement field is limited by the basis in the approximation space.

The second category is the cohesive zone models. The separation of cohesive zone model takes place across an extended crack tip or cohesive zone [2, 19, 21, 39, 67]. This model uses cohesive zone elements to describe the cohesive forces which occur when material elements are being pulled apart. An advantage of the cohesive zone model is that it can handle and predict the behavior of uncracked structures such as blunt notches. However, since the crack can only propagate along the cohesive zone elements, the crack is not completely free to evolve.

The last category is the phase field fracture methods. The methods in this category introduce an additional damage parameter which indicates the material state (a cracked or intact material). In 1998, Francfort and Marigo proposed a variation model of quasi-static crack evolution [26]. This variation fracture model follows the spirit of Griffith's theory in brittle fracture [37]. In addition, it frees itself from the constraint of Griffith's theory where pre-existing cracks and pre-determined crack path is no longer needed. Furthermore, this variation fracture model Gamma-converges to a sum of elastic energy and fracture energy [1]. Later, Bourdin, Francfort and Marigo developed various numerical methods to implement the variation fracture model numerically [6]. Since then, there has been an extensive literature on the phase field methods [4, 5, 7–9, 54, 58, 71, 77].

2.7 Experimental methods

There are well-developed testing methods for toughness in homogeneous materials such as the compact tension (CT) [79], center cracked tension (CCT) [22], single edge notch tension (SENT) [78], three point bending (single edge notch bend, SENB) [79], four point bending [80], and the Chevron-

Notch method [65], etc. These methods use the specimens with particular dimensions so the relationship between the stress intensity factor and the measured force is known. Therefore, one can easily use the load cell data to calculate the stress intensity factor. However, these methods only work on homogeneous materials.

There are some experimental methods that can work for heterogeneous specimens, for example, double cantilever beam method for laminar composite [52] or r-curve measurement for ceramics [50]. However, there are no robust test methods that apply to arbitrary heterogeneous specimens yet.

Chapter 3

SURFING BOUNDARY CONDITIONS AND EFFECTIVE TOUGHNESS

[1] M. Z. Hossain, C.-J. Hsueh, B. Bourdin, and K. Bhattacharya. "Effective toughness of heterogeneous media". In: *Journal of the Mechanics and Physics of Solids* 71 (2014), pp. 15–32. DOI: http://dx.doi.org/10.1016/j.jmps.2014.06.002. URL: http://www.sciencedirect.com/science/article/pii/S0022509614001215.

Fracture mechanics in heterogeneous media is a fascinating problem. The cracks can deflect, bifurcate, and form complex crack paths. The propagation of cracks can also be trapped and suddenly jump. There are more interesting behaviors for crack propagation in heterogeneous materials. However, these behaviors make the crack propagation in heterogeneous materials interesting but also difficult. In order to study crack propagations in heterogeneous materials, two requirements are needed: (macroscopic) steady crack propagation and a tool to characterize the (macroscopic) driving force on the crack. With these two requirements, one can investigate the relationship between the microstructure and the effective toughness. In this chapter, we introduce the *surfing boundary condition*, which ensures that the crack can steadily propagate macroscopically, but this boundary condition also allows the crack to explore itself microscopically. We also define the effective toughness of heterogeneous materials from the (macroscopic) J-integral. The idea of the surfing boundary condition is first proposed by Prof. Blaise Bourdin and rest of the work presented in this chapter is primarily due to M. Zubaer Hossain and included for completeness.

3.1 Surfing boundary condition

We are interested in the scenario where the scale of the heterogeneity is small compared to the scale of the engineering object of interest as shown in Figure 3.1. Therefore, we seek to find an effective homogeneous materials with effective elastic modulus and effective toughness. As a result, one can use these heterogeneous materials in their engineering application without resolving the microscale details. Furthermore, we wish to have

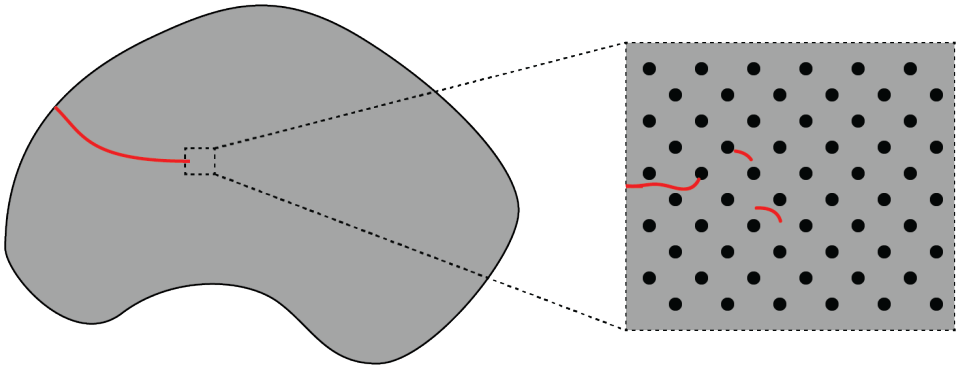

Figure 3.1: The idea of the surfing boundary condition

a steady and defined crack propagation at the macroscopic scale, but the crack is completely free to evolve in any manner that it chooses at the microscopic scale.

In order to achieve this, we introduce a boundary condition that we called the surfing boundary condition. It is a time-dependent steadily translating crack opening displacement field. Suppose the macroscopic crack propagation direction is the x_1-direction. The surfing boundary condition to achieve it is

$$u^*(x_1, x_2, t) = U(x_1 - vt, x_2), \tag{3.1}$$

where U is the crack opening displacement field. A common choice of the crack opening displacement field is the K_I displacement field [90]

$$U(x_1, x_2) = \frac{K_I}{2\mu}\sqrt{\frac{r}{2\pi}}\,(\kappa - \cos\theta)\left(\cos\frac{\theta}{2}\hat{e}_1 + \sin\frac{\theta}{2}\hat{e}_2\right), \tag{3.2}$$

where K_I is the stress intensity factor, μ the Lamé constant, κ the bulk modulus, $r = \sqrt{x_1^2 + x_2^2}$ is the distance to the origin, and θ is the angle to the x_1-axis.

3.2 Effective toughness

The J-integral is an integral which can measure the driving force on the crack. When a crack propagates in homogeneous materials, the driving force and the J-integral is constant during crack propagation. The toughness of the homogeneous materials is defined as that constant because the crack cannot propagate and break entire material unless the driving force reaches that constant. However, the driving force and the J-integral is usually oscillating when a crack propagates in heterogeneous materials. Thus,

we define the effective toughness as the peak of the J-integral because the crack cannot propagate over a long distance and further breaks the material unless the applied driving force exceeds that peak value. We justify the use of the J-integral in heterogeneous media in Chapter 4.

3.3 Validation

We use the phase field model (the details of this model are in Chapter 6) to validate the concept of surfing boundary condition. We use the mode-I asymptotic fracture displacement field as the surfing boundary condition

$$\begin{bmatrix} U_1 \\ U_2 \end{bmatrix} = \frac{K_I}{2\mu}\sqrt{\frac{r}{2\pi}}(\kappa - \cos\theta)\begin{bmatrix} \cos\frac{\theta}{2} \\ \sin\frac{\theta}{2} \end{bmatrix}, \tag{3.3}$$

where K_I is the stress intensity factor, μ the Lamé constant, and κ the bulk modulus. We first apply this surfing boundary with $K_I = 1$ on a homogeneous material as shown in Figure 3.2(a). The J-integral increases at the beginning. When the J-integral reaches the value of the material toughness, the crack starts propagating as shown in Figure 3.2(b). We also test with different K_I value and we found that no matter which surfing boundary condition we use, the crack starts to propagate when the J-integral reaches the material toughness, as shown in Figure 3.2(c). We also use different material toughness and the crack starts to propagate when the J-integral reaches the material toughness as shown in Figure 3.2(d).

We also tested the surfing boundary condition on heterogeneous materials. We set that the heterogeneous materials have uniform toughness and Poisson ratio. The elastic modulus distribution is

$$E = E_0 - E_1 \cos\left(\frac{2\pi x_1}{\lambda}\right) \tag{3.4}$$

as shown in Figure 3.3(a). Gao had studied this problem in the low contrast regime [27]. We compare the numerical results with Gao's results as shown in Figure 3.3. We found good agreement between the results.

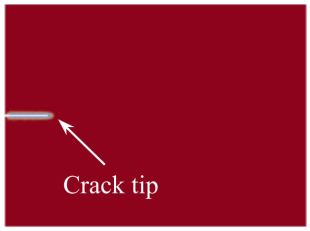

(a) The simulation domain

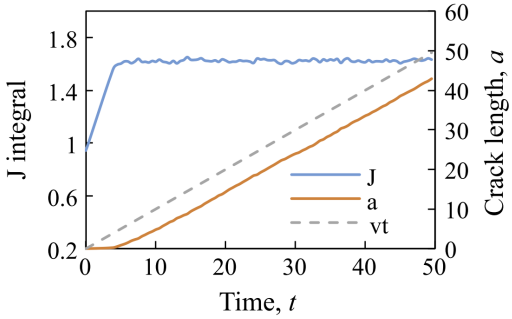

(b) Computed J-integral and crack length

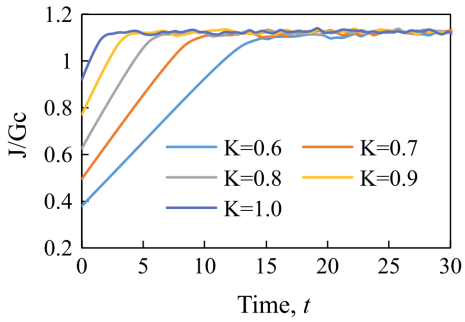

(c) Change surfing boundary condition

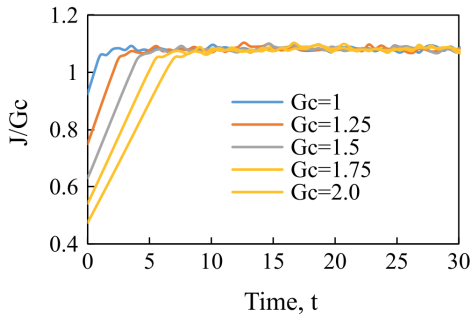

(d) Change material toughness

Figure 3.2: Verification on homogeneous materials

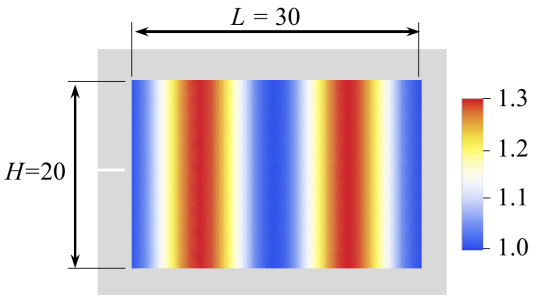

(a) Elastic modulus distribution

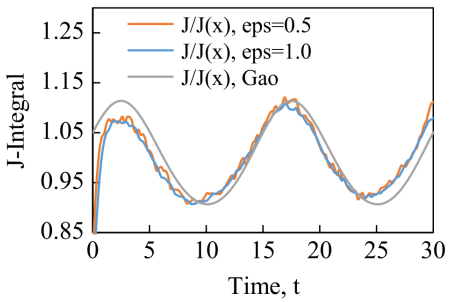

(b) Computed J-integral

Figure 3.3: Verification on heterogeneous materials

Chapter 4

EFFECTIVE J-INTEGRAL IN HETEROGENEOUS MATERIALS

[1] C.-J. Hsueh and K. Bhattacharya. "Homogenization and Path Independence of the J-Integral in Heterogeneous Materials". In: *Journal of Applied Mechanics* 83.10 (2016), p. 101012. DOI: 10.1115/1.4034294. URL: http://appliedmechanics.asmedigitalcollection.asme.org/article.aspx?articleid=2540451.

The J-integral that determines the driving force on a crack-tip is a central concept of fracture mechanics. It is useful because of its path-independency in homogeneous materials. However, most of the materials are heterogeneous at a microscale and the J-integral is not necessarily path independent in heterogeneous materials. In this chapter, we use homogenization theory in a quasi-periodic setting to show the existence of a macroscopic J-integral. We prove that this is path-independent in a macroscopically homogeneous material if the integral path is large compared to the size of the heterogeneities. This result justifies the common engineering use of the J-integral. More immediately, this result justifies the use of the J-integral in our definition of effective toughness in Chapter 3.

4.1 Effective J-integral

The propagation of cracks is driven by the energy release rate [37, 43], i.e., the rate of change of energy with respect to crack extension. Furthermore, this energy release rate may be described by the J-integral [74]

$$J = \int_\Gamma t_i \left(W\delta_{ij} - \frac{\partial u_k}{\partial x_i}\sigma_{kj} \right) n_j ds, \tag{4.1}$$

where W is the stored energy density, u the displacement, $\sigma = \frac{\partial W}{\partial F}$ the stress, n the normal to the contour Γ enclosing the crack tip, and t the tangent to the crack at the crack tip. The J-integral is extremely useful because it is path-independent, i.e., it does not depend on the contour Γ as long as the medium is homogeneous. As a result, the J-integral is widely used because one can choose a contour which is most convenient to evaluate the integrand.

However, the path-independency of J-integral no longer holds in heterogeneous materials. And most materials are heterogeneous at a microscopic scale. Typically, one uses homogenization theory to define an effective elastic medium which is homogeneous at the engineering scale if the scale of heterogeneities is small compared to the engineering object of interest as shown in Figure 4.1. Then one applies the J-integral on the effective homogeneous medium. Unfortunately, it is not clear that the J-integral has such homogenized properties, i.e., the relation between a 'microscopic' and 'macroscopic' J-integral remains open. The J-integral computed with the stress and the strain associated with the heterogeneous medium is not guaranteed to converge to the J-integral computed with the stress and the strain associated with the effective homogeneous medium as the contour becomes very large. In other words, it is not clear whether one can use the solutions to the homogenized equation to compute an effective J-integral.

Indeed, a casual examination of the expression for the J-integral in (4.1) suggests that the microscopic J-integral will in general be different from the macroscopic or homogenized J-integral. According to the homogenization theory [38], the average of the microscopic stored energy density is equal to the macroscopic stored energy density. However, this does not appear to be true for the second term in the parenthesis in the integrand of equation (4.1). In other words, the product of the stress and the displacement gradient fluctuate at the microscopic scale is not necessarily equal to the average of their products.

$$\left\langle \frac{\partial u_k}{\partial x_i} \right\rangle \left\langle \sigma_{kj} \right\rangle = \left\langle \frac{\partial u_k}{\partial x_i} \sigma_{kj} \right\rangle ? \tag{4.2}$$

This raises an issue of using the J-integral in engineering practice.

4.2 Periodic homogenization

Homogenization is a method to study a system with a rapid oscillating modulus. Consider a domain Ω (a bounded open set in $\mathbb{R}^N$) with a heterogeneous elastic medium where the heterogeneities have a length-scale $\varepsilon \ll 1 = \text{diam}(\Omega)$ in dimensionless units. This domain may contain a smooth crack whose length is $O(1)$. Specifically, we assume that the medium is quasiperiodic so that the stored energy density

$$\widetilde{W}^{\varepsilon}(F, x) = W\left(F, x, \frac{x}{\varepsilon}\right), \tag{4.3}$$

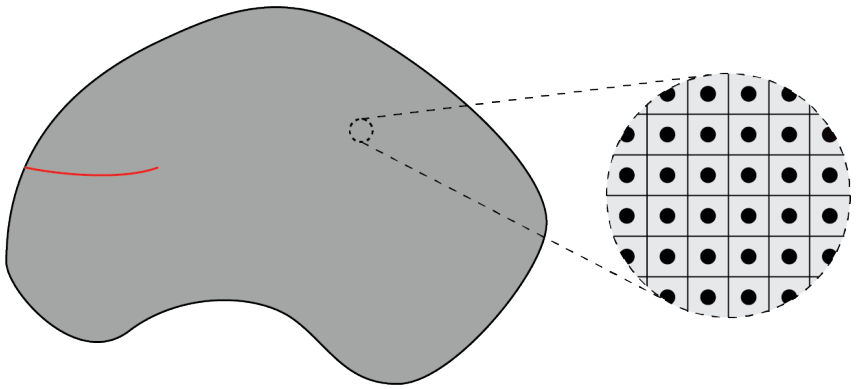

Figure 4.1: Fracture in a homogenized material

where F is the displacement gradient, $W : \mathbb{R}^{N\times N} \times \Omega \times Y \to \mathbb{R}$, Y is the unit cube in $\mathbb{R}^N$ and $W(F, x, y)$ is periodic in y for each x, F. This is shown schematically in Figure 4.1: the medium appears periodic if we look closely at some point $x \in \Omega$. In the case of linear elasticity,

$$W(F, x, y) = \frac{1}{2} F_{ij} \mathbb{C}_{ijkl}(x, y) F_{kl}, \tag{4.4}$$

where $\mathbb{C} : \Omega \times Y \to \mathbb{R}^{N^4}$ is the elastic modulus satisfying major and minor symmetries, and $\mathbb{C}(x, y)$ is periodic in y for each x.

We seek solutions of the equations of elasticity by seeking to minimize the total energy

$$\mathcal{E}^\varepsilon[u] = \int_\Omega \widetilde{W}^\varepsilon(\nabla u, x) dx - \mathcal{L}[u] = \int_\Omega W\left(\nabla u, x, \frac{x}{\varepsilon}\right) dx - \mathcal{L}[u], \tag{4.5}$$

where $\mathcal{L}$ depends on the body-force and boundary tractions amongst all displacements $u : \Omega \to \mathbb{R}^N$ that satisfy the imposed displacement boundary conditions. This problem is difficult because W and consequently the solution oscillates on the scale of the heterogeneities ε. Homogenization theory [11, 63] states that if ε is small enough and if $W(F, x, y)$ is convex in F for each x, y, then we can replace the problem above with the following effective problem: minimize

$$\mathcal{E}[u] = \int_\Omega \overline{W}(\nabla u, x) dx - \mathcal{L}[u] \tag{4.6}$$

amongst all displacements that satisfy the imposed displacement boundary conditions where $\overline{W} : \mathbb{R}^{N\times N} \times \Omega \to \mathbb{R}$ is the effective elastic energy density and may be obtained by solving the following problem for each

F, x: minimize

$$\overline{W}(F,x) = \int_Y W(F + \nabla\varphi(y), x, y)dy \tag{4.7}$$

overall periodic displacement fields $\varphi : Y \to \mathbb{R}^N$. Note that the integrand of (4.6) is smooth on the scale of ε and thus the solution is also expected to be smooth at that scale. It is also true that the effective stress is given by

$$\overline{\sigma}_{ij} = \frac{\partial \overline{W}}{\partial F_{ij}}. \tag{4.8}$$

Further, under suitable growth and strict convexity conditions on W, the minimum is attained and unique up to an inessential translation. We call the minimum $\varphi^{F,x}$. Thus,

$$\mathcal{E}[u] = \int_\Omega \int_Y W\left(\nabla_x u + \nabla_y \varphi^{\nabla_x u, x}, x, y\right) dydx - \mathcal{L}[u]. \tag{4.9}$$

4.3 Configurational force balance

We use the effective functional (4.9) to derive an effective configurational force balance. We take $\mathcal{L} = 0$ for convenience (i.e., no body force, and traction-free and displacement boundary conditions), but the treatment is easily modified otherwise.

Let $\bar{u}$ minimize $\mathcal{E}$ defined in (4.9) for some given boundary conditions. Recall that it is smooth on the scale of ε. We now consider the inner variation of the minimized total energy. Consider a family of rearrangments $z^s : \Omega \to \Omega$ one to one and onto for $s \in [0,1]$ that satisfy $z = x$ on $\partial\Omega$, $\det \nabla_x z > 0 \ \forall x \in \Omega$, and $z^0(x) = x$. Set $\overline{u}^s(x) = \overline{u}(z^s(x))$. Note that $\overline{u}^s$ is a family of perturbations of the minimizer $\overline{u}$ with $\overline{u}^0 = \overline{u}$. Therefore, the function

$$f(s) := \mathcal{E}[\overline{u}(z^s)] \tag{4.10}$$

has a minimum at $s = 0$ and therefore

$$f'(0) = 0. \tag{4.11}$$

We now compute $f'(0)$.

Set $\psi^s = \varphi^{\nabla_x \overline{u}^s, x}$ and $\overline{F}(x) = \nabla_x \overline{u}(x)$, and note that

$$\nabla_x \overline{u}^s = \nabla_x \left(\overline{u}(z^s(x))\right) = \overline{F}(z^s(x))\nabla_x z^s(x). \tag{4.12}$$

So,

$$f(s) = \int_\Omega \int_Y W(\overline{F}(z^s(x))\nabla_x z^s + \nabla_y \psi^s, x, y) dy dx \tag{4.13}$$

$$= \int_\Omega \int_Y W(\overline{F}(z)(\nabla_z x^s)^{-1} + \nabla_y \psi^s, x^s, y) J dy dz, \tag{4.14}$$

where we have changed integration variables from x to z by inverting z^s to obtain $x = x^s(z)$, and set $J = \det(\nabla_z x^s)$. Now, set

$$\overline{F}^s = \overline{F}(z)(\nabla_z x^s)^{-1}, \quad G^s = \overline{F}^s + \nabla_y \psi^s = \overline{F}^s + \nabla_y \varphi^{\overline{F}^s, x^s}. \tag{4.15}$$

We can now calculate

$$f'(s) = \int_\Omega \int_Y \left(\frac{\partial W}{\partial F_{ij}} \dot{G}^s_{ij} + \frac{\partial^* W}{\partial^* x_i} \dot{x}_i + W \frac{\dot{J}}{J} \right) J dy dz, \tag{4.16}$$

where we use $\frac{\partial^*}{\partial^* x_i}$ to represent the explicit derivative with respect to x_i and $(\dot{q}) = \frac{dq}{ds}$ to denote the total derivative of q with respect to s. Recalling the identities

$$\dot{\overline{A^{-1}}} = -A^{-1}\dot{A}A^{-1}, \quad \dot{\overline{\det A}} = (\det A) A^{-T}_{ij} \dot{A}_{ij}, \tag{4.17}$$

we obtain

$$\dot{G}^s_{ij} = \dot{\overline{F}}^s_{ij} + \frac{\partial \dot{\psi}^s_i}{\partial y_j} = -\overline{F}_{ik}(z) \left(\frac{\partial x^s_k}{\partial z_l} \right)^{-1} \frac{\partial \dot{x}^s_l}{\partial z_m} \left(\frac{\partial x^s_m}{\partial z_j} \right)^{-1} + \frac{\partial \dot{\psi}^s_i}{\partial y_j}, \tag{4.18}$$

$$\frac{\dot{J}}{J} = \left(\frac{\partial x^s_i}{\partial z_j} \right)^{-T} \left(\frac{\partial \dot{x}^s_i}{\partial z_j} \right)^{-1}. \tag{4.19}$$

Further, from the unit cell problem of minimizing (4.7), we can infer that

$$\int_Y \frac{\partial W}{\partial F_{ij}} \frac{\partial \dot{\psi}^s_i}{\partial y_j} dy = 0. \tag{4.20}$$

We substitute (4.18) through (4.20) into (4.16), set $s = 0$ (so that $\frac{\partial x^s_i}{\partial z_j} = \delta_{ij}$) and change integration variables back to x:

$$f'(0) = \int_\Omega \int_Y \left(\left(W\delta_{ik} - \frac{\partial W}{\partial F_{ij}} \overline{F}_{ik} \right) \frac{\partial \dot{x}_k}{\partial x_j} + \frac{\partial^* W}{\partial^* x_k} \dot{x}_k \right) dy dx, \tag{4.21}$$

where $\dot{x} = \dot{x}^s(z)|_{s=0}$. We note that $\overline{F}$ and $\dot{x}$ are independent of y and therefore we can integrate with respect to y. We obtain by recalling (4.7),

$$f'(0) = \int_\Omega \left(\left(\overline{W}\delta_{ik} - \frac{\partial \overline{W}}{\partial F_{ij}} \overline{F}_{ik} \right) \frac{\partial \dot{x}_k}{\partial x_j} + \frac{\partial^* \overline{W}}{\partial^* x_k} \dot{x}_k \right) dx \tag{4.22}$$

$$= \int_\Omega \left(-\frac{\partial}{\partial x_j} \left(\overline{W}\delta_{ik} - \frac{\partial \overline{W}}{\partial F_{ij}} \overline{F}_{ik} \right) + \frac{\partial^* \overline{W}}{\partial^* x_k} \dot{x}_k \right) \dot{x}_k dx, \tag{4.23}$$

where we have used the divergence theorem and the fact that $\dot{x} = 0$ on $\partial\Omega$ (since $x = z^s(x)$ on $\partial\Omega$). Now, since $f'(0) = 0$ for all z^s and thus arbitrary $\dot{x}$, we obtain the macroscopic configurational force balance

$$\frac{\partial \overline{C}_{ij}}{\partial x_j} = \frac{\partial^* \overline{W}}{\partial^* x_i}, \tag{4.24}$$

where

$$\overline{C}_{ij} = \overline{W}\delta_{ij} - \overline{F}_{ki}\frac{\partial \overline{W}}{\partial F_{kj}} = \overline{W}\delta_{ij} - \overline{F}_{ki}\overline{\sigma}_{kj} \tag{4.25}$$

is the effective configurational stress tensor.

Finally, if the material is macroscopically homogeneous, i.e., W and consequently $\bar{W}$ is independent of x, then we see from (4.24) that

$$0 = \int_D \frac{\partial \overline{C}_{ij}}{\partial x_j} dx = \int_{\partial D} \overline{C}_{ij} n_j dA \tag{4.26}$$

using the divergence theorem where D is any domain that is large compared to the size of the heterogeneities (ε). Now, consider a domain with a crack in two dimensions. Given any two contours Γ_1 and Γ_2 that contain the crack tip, set D to be the annular region between the contours. Now, take $\partial D = \Gamma_1 \cup \Gamma_2$ with the outward normal $-n$ and n on the two segments of the boundary. Taking the inner product of the equation above with the tangent to the crack tip, we obtain

$$\int_{\Gamma_1} t_i \left(\overline{W}\delta_{ij} - \frac{\partial \overline{u}_k}{\partial x_i}\overline{\sigma}_{kj}\right) n_j ds = \int_{\Gamma_2} t_i \left(\overline{W}\delta_{ij} - \frac{\partial \overline{u}_k}{\partial x_i}\overline{\sigma}_{kj}\right) n_j ds, \tag{4.27}$$

or the path-independence of the macroscopic $J-$integral.

Chapter 5

ELASTIC HETEROGENEITY AND EFFECTIVE TOUGHNESS

[1] M. Z. Hossain, C.-J. Hsueh, B. Bourdin, and K. Bhattacharya. "Effective toughness of heterogeneous media". In: *Journal of the Mechanics and Physics of Solids* 71 (2014), pp. 15–32. DOI: http://dx.doi.org/10.1016/j.jmps.2014.06.002. URL: http://www.sciencedirect.com/science/article/pii/S0022509614001215.

In this chapter, we examine the role of elastic heterogeneity on effective toughness. We consider the small contrast limit and use a semi-analytic method. We show through examples that elastic heterogeneity can significantly enhance the effective toughness, and that effective toughness can be asymmetric.

5.1 Background

Fracture mechanics is an important field in solid mechanics where the concern focuses on the nucleation and propagation of cracks in various materials. The discipline was founded during World War I by A.A. Griffith when he conducted a study on brittle materials [37]. Subsequent research by G.R. Irwin connected the energy release rate with infinitesimal crack propagation and successfully defined the stress intensity factor [42]. Since then there have been significant advances both in our theoretical understanding and in practice.

In particular, engineers have pursued achieving a level of performance greater than typical materials. Therefore, many types of composites have been developed in the past few decades. Due to better performance, many researchers began to investigate the behavior of heterogeneous materials in fracture mechanics. However, fracture mechanics in heterogeneous materials has not been fully understood yet. There are massive literatures, which study this problem with different approaches. Faber and Evans studied toughening induced by the second-phase particles subject to microcracking and deflection [23–25]. Gao assumed that the elastic contrast is

small and used linear expansion to study the stress intensity contribution of elastic modulus heterogeneity [27]. Hutchinson and Suo studied fracture in layer material [40]. Bower and Ortiz investigated when a crack is trapped by tough inclusions [10]. In a related field, Xia et al have shown both theoretically and experimentally that without change in adhesive, the bending heterogeneity dramatically increases the peeling force in adhesive film [86, 88]. All these studies show that the cracks can have complex behavior in heterogeneous materials and the toughening mechanism is also complex.

5.2 Semi-analytical method

We consider a situation on where the elastic modulus is heterogeneous but the contrast is small. Specifically, we assume that $\mathbb{C}(x) = \mathbb{C}^0 + \mathbb{C}^1(x)$ and $|\mathbb{C}^1| \ll |\mathbb{C}^0|$. We first consider an infinite homogeneous body with a semi-infinite straight crack in it. Consider a polar coordinate system where $\theta = 0$ is in the direction of crack propagation and the origin is on the crack tip. The traction-free boundary condition on the crack face is

$$\sigma_{r\theta} = \sigma_{\theta\theta} = 0 \quad \text{at} \quad \theta = \pm\pi. \tag{5.1}$$

By assuming no body force and following William's procedure [85], we can calculate the asymptotic mode-I displacement field [90].

$$\begin{bmatrix} u_r^0 \\ u_\theta^0 \end{bmatrix} = K_I \frac{1+\nu}{E}\sqrt{\frac{r}{2\pi}} \begin{bmatrix} \left(\frac{5}{2} - 4\nu\right)\cos\frac{\theta}{2} - \frac{1}{2}\cos\frac{3\theta}{2} \\ -\left(\frac{7}{2} - 4\nu\right)\sin\frac{\theta}{2} + \frac{1}{2}\sin\frac{3\theta}{2} \end{bmatrix}. \tag{5.2}$$

We define this displacement field of a semi-infinite crack in a homogeneous body as the base solution u^0. We now consider the heterogeneous body. The displacement field would be the base solution with a perturbation field $u^1(x)$.

$$u_i(x) = u_i^0(x) + u_i^1(x). \tag{5.3}$$

Therefore, the equilibrium equation becomes

$$\left[\left(\mathbb{C}_{ijkl}^0 + \mathbb{C}_{ijkl}^1\right)\left(u_{k,l}^0 + u_{k,l}^1\right)\right]_{,j} = 0, \tag{5.4}$$

where

$$u_{i,j} := \frac{\partial u_i}{\partial x_j}. \tag{5.5}$$

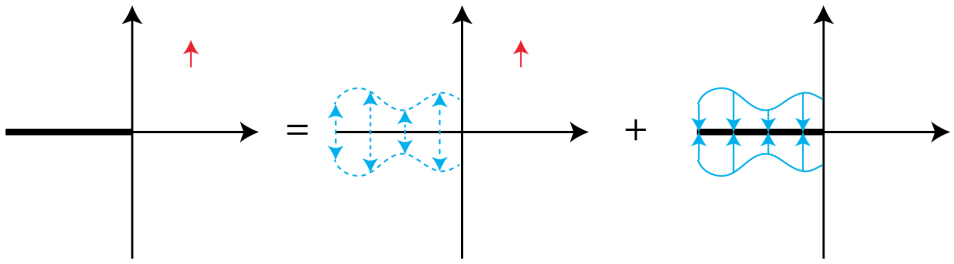

Figure 5.1: Superposition of a system with crack

Since the contrast of on the elastic modulus is small, we would except that the perturbation of the displacement field is also small. Therefore, we drop the high order term in equation (5.4) to obtain the approximation

$$\left(\mathbb{C}^0_{ijkl}u^0_{k,l}\right)_{,j} + \left(\mathbb{C}^1_{ijkl}u^0_{k,l}\right)_{,j} + \left(\mathbb{C}^0_{ijkl}u^1_{k,l}\right)_{,j} = 0. \tag{5.6}$$

The first term in equation (5.6) is identical to the equilibrium equation of the homogeneous material. Thus, equation (5.6) can be written as

$$\left(\mathbb{C}^0_{ijkl}u^1_{k,l}\right)_{,j} = -\left(\mathbb{C}^1_{ijkl}u^0_{k,l}\right)_{,j}. \tag{5.7}$$

Equation (5.7) shows that the perturbed displacement field induced by the elastic modulus perturbation can be treated as the displacement field induced by a body force

$$b_i := \left(\mathbb{C}^1_{ijkl}u^0_{k,l}\right)_{,j}. \tag{5.8}$$

By using this approach, the elastic heterogeneity in a system is equivalent to a homogeneous system subject to some body forces (the left figure in Figure 5.1).

In order to calculate the contribution of this equivalent body force, we use the weight function theory [12]. Consider a system subject to some body forces with a crack in it. We use the superposition principle to decompose this system with crack into two systems as shown in Figure 5.1. One system is the domain subject to body forces without a crack. The other system has no body forces but some tractions are applied on the crack faces. These tractions are compatible (but with the opposite sign) with the stress state in the first system. As a result, we can satisfy all the equilibrium conditions and the traction-free condition on the crack face when we combine these two systems.

For simplicity, we focus on a two phase system where each phase is a isotropic material with the same Poisson's ratio. Therefore, we have

$$\mathbb{C}^0_{ijkl} = \lambda^0 \delta_{ij}\delta_{kl} + \mu^0(\delta_{ik}\delta_{jl} + \delta_{il}\delta_{jk}) \tag{5.9}$$

and $\mathbb{C}^1(x) = \chi(x)p\mathbb{C}^0$, where $\chi(x)$ is the characteristic function of inclusions, and $p \ll 1$.

First, we consider the system subject to body forces without a crack (the center figure in Figure 5.1). By using the Papkovich-Neuber solution, we have the solution of equation (5.7), which is

$$u^1_i = \frac{1}{2\mu^0}\left[(\phi + x_k\psi_k)_{,i} - 4(1-\nu)\psi_i\right], \tag{5.10}$$

where

$$\phi = -\frac{b_i x_i}{2(1-\nu)} \tag{5.11}$$

$$\psi_i = \frac{b_i}{2(1-\nu)}. \tag{5.12}$$

By equation (5.8), (5.10), (5.11), and (5.12), we are able to calculate the perturbation field u^1 induced by the elastic modulus perturbation. Note that this system has no contribution on the crack (the stress intensity factor induced by body forces is zero).

We then consider the system with a crack subject to some traction on the crack faces (the right figure in Figure 5.1). The traction on the crack faces are

$$t_i = -\mathbb{C}^0_{ijkl}u^1_{k,l}n_j, \tag{5.13}$$

where u^1 is calculated by equation 5.10. The weight function theory provides a close-form relationship with the traction on the crack faces and the induced stress intensity factor. The relationship is the following:

$$K^* = K_I - iK_{II} = \frac{\sqrt{2}}{\pi^{\frac{3}{2}}}\int_{-\infty}^{0} -iR(t)|t|^{-\frac{1}{2}}dt, \tag{5.14}$$

where $R(x) = \sigma_{12} + i\sigma_{22}$ is the complex traction on the semi-infinite crack faces. By equation 5.14, we are able to calculate the elastic heterogeneity (or the equivalent body forces) induced stress intensity factor.

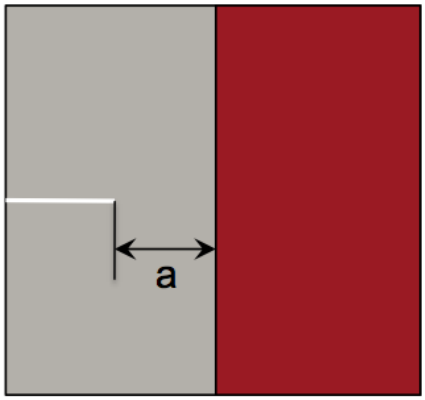

(a) Crack propagates toward an interface (red material is stiffer than the gray material)

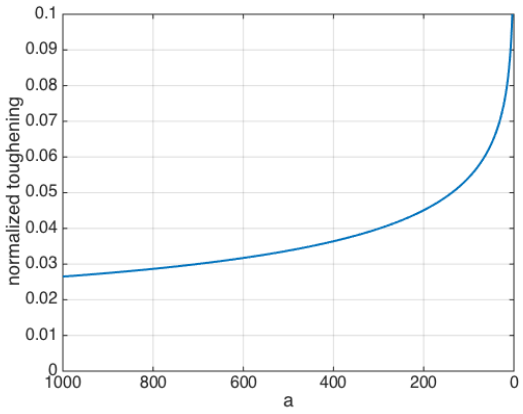

(b) Induced stress intensity factor by the elastic heterogeneity

Figure 5.2: A crack in a compliance material propagates toward a stiff material

5.3 Example 1: Toughening by elastic heterogeneity

We provide two examples to show that the macroscopic toughness can be controlled by the microstructure. The first example shows that the macroscopic toughness can be enhanced by the heterogeneity. Furthermore, the second example shows that the macroscopic toughness can be asymmetrical. This is an unusual behavior in natural materials. You would not expect a material to break easily from left to right but hard to break from right to left. Although this semi-analytical method only works for small contrast, it shows the possibility that one can manipulate the macroscopic toughness by controlling the microstructure.

We first consider a crack in a compliant material (gray material in Figure 5.2(a)) propagate towards a stiff material (red material in Figure 5.2(a)). The distance between the crack tip and the interface is defined as a. We then assume that the stiff material is 10 times stiffer than the compliant material. The induced stress intensity factor is calculated by equation (5.8) to equation (5.14).

When the crack tip is in the compliant material and propagates toward the stiff material, the induced stress intensity factor by equation (5.14) is a negative value. This result means the elastic heterogeneity will decrease the driving force on the crack tip. Therefore, one has to input more energy

to propagate the crack. In other words, the material is tougher by the elastic heterogeneity. Moreover, the induced stress intensity diverges to minus infinity when the crack tip is close to the interface. It means that we need to input more and more energy to let the crack tip approach the interface. The results are shown in Figure 5.2(b).

The crack cannot penetrate the interface because there is no nucleation criteria in Griffith's fracture. When the crack tip is on the interface from the compliant material to the stiff material, the singularity of the stress field is weaker than a regular crack so the stress intensity factor is zero [89].

A related study was done by He and Hutchinson [59]. They studied an oblique crack approaches the interface. They argued that the crack would curve away from the interface if the crack approaches a stiffer material.

5.4 Example 2: Asymmetric effective toughness

The second case we study is a crack propagate in a matrix with asymmetric inclusions as shown in Figure 5.3(a). Since the pattern is asymmetric, the crack propagating in one direction (as in Figure 5.3(a)) does not necessarily have the same behavior as if it were to propagate in the opposite direction (as in Figure 5.3(b)). We assume the inclusions are stiffer than the matrix and plot the results in Figure 5.3(c). It shows that the toughness can be asymmetrical, i.e., propagation in Figure 5.3(b) is harder than that in Figure 5.3(a).

We also studied the effect of the shape of inclusions as shown in Figure 5.4(a). The nose of the asymmetric inclusions is characteristic of the n-th order polynomial $y = x^n$ (in local coordinates). The length of the nose and the tail are 1 and L respectively. We use the shape $n = 2.5$ and $L = 0.25$ (the inclusion in Figure 5.3) as a baseline, which is shown in 5.4(b). We first change the shape of the nose to be sharper and show the results in Figure 5.4(c). The results indicate that the toughening mechanism is not sensitive to the shape of the nose. We then change the length of the tail to be shorter and show the results in Figure 5.4(d). In shows that the tougnening mechanism is sensitive to the tail of the inclusions. Once we make the tail shorter, the asymmetry is reduced.

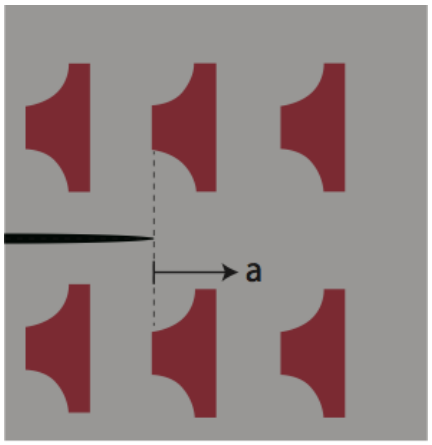

(a) Diverging direction

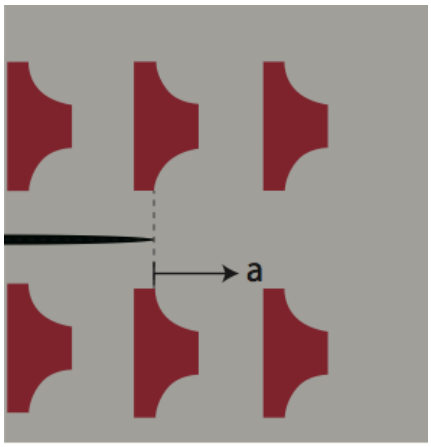

(b) Converging direction

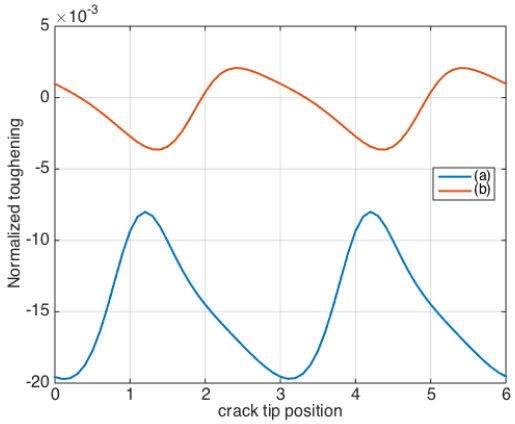

(c) Induced stress intensity factor by the elastic heterogeneity

Figure 5.3: A crack propagates in an asymmetric pattern

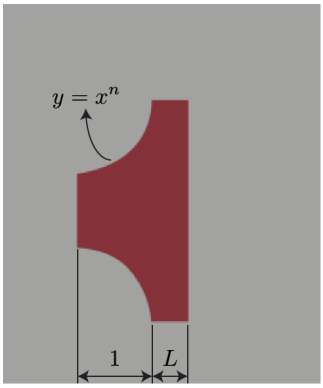

(a) Parameter of the inclusions

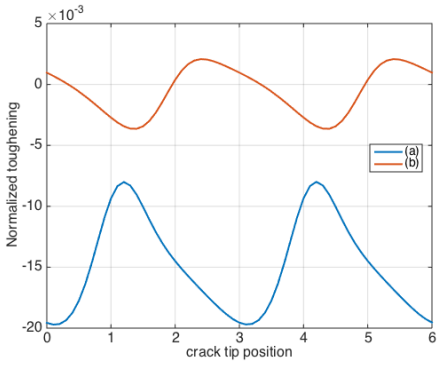

(b) $n = 2.5, L = 0.25$

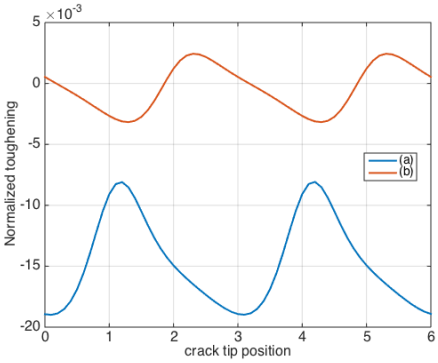

(c) $n = 10, L = 0.25$

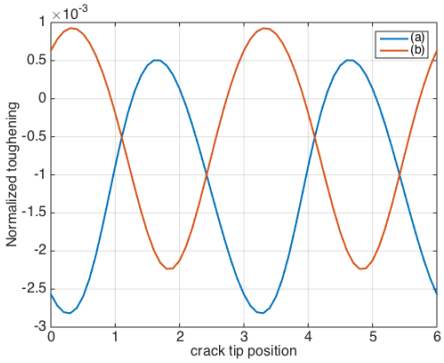

(d) $n = 2.5, L = 0.01$

Figure 5.4: Shape of inclusions effect

Chapter 6

NUMERICAL STUDIES

In this chapter, we study the role of microstructure in determining the overall or effective toughness of a heterogeneous material. We focus on bimaterials, or a composite of two materials with different elastic moduli, in two dimensions. We use a code called *mef90* (bitbucket.org/bourdin/mef90-sieve/), a phase field method due to Bourdin et al [5–7, 26], for our computational study. This is described in section 6.1. We have seen in the previous section that elastic heterogeneity can lead to toughening. We explore this, and specifically the problem of optimizing a combination of effective toughness and effective elastic modulus, in the context of a square array of compliant inclusions in a stiff matrix. We show in section 6.2 that we can significantly enhance toughness without compromising elastic elastic modulus too much. We note that the enhancement of toughness is the result of two contribution: an inhomogeneous stress distribution and renucleation. We study these in section 6.3. Finally, we study the asymmetry of effective toughness in section 6.4.

6.1 Phase-field fracture model

In the classical brittle fracture theory [37, 42, 43], cracks are geometrically idealized as surfaces of displacement discontinuity. A basic model in classical brittle fracture theory contains the elastic energy and the material toughness (energy dissipated through fracture or energy required to create a unit area of new cracks)

$$\mathcal{E}(u,\Gamma) = \int_{\Omega\setminus\Gamma} W(\nabla u)dx + \int_{\Gamma} G ds, \tag{6.1}$$

where W is the elastic energy, G the toughness, u the displacement field, and $\Gamma \subset \Omega$ the crack sets. Therefore, the classical brittle fracture theory can be viewed as minimizing energy with respect to displacement field u and the crack sets Γ, or a competition between energy release rate (how much elastic energy can be reduced by crack extension) and the material toughness (how much energy is needed for creating new cracks).

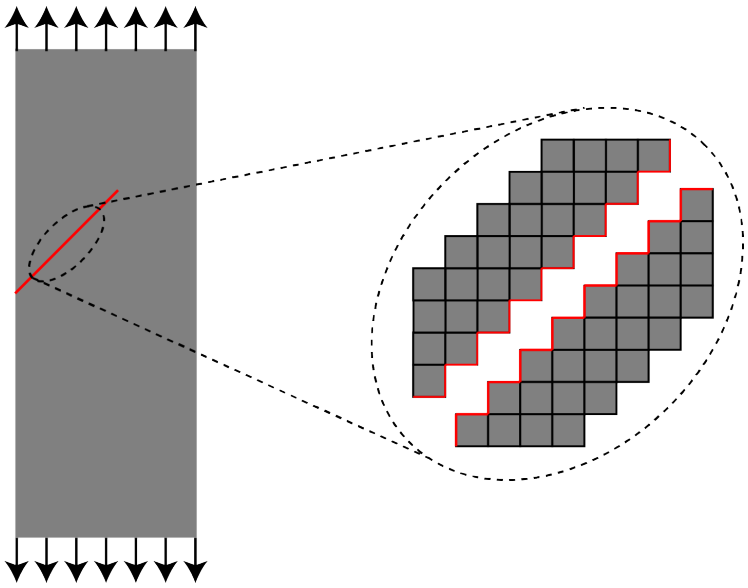

Figure 6.1: The measure of surface can be biased by the meshes

However, equation (6.1) is hard to implement numerically because it is hard to systematically minimize the free discontinuity problem. Furthermore, the measure of the surfaces (cracks) can be easily biased by the meshes. For example, consider an inclined crack in a body as shown in Figure 6.1. No matter how fine the square meshes are, the error of the free surface measurement (red surface in Figure 6.1) would be $\frac{2-\sqrt{2}}{\sqrt{2}} \approx 41\%$. One can overcome these by using discontinuous Galerkin approaches such as extended finite element method (XFEM) [17].

Alternately, a phase field fracture method surmounts these difficulties [5–7, 26]. This is a regularized method which introduces a scalar damage field v taking values in $[0, 1]$ to describe the material states. The undamaged state (intact material) is represented as $v = 0$ and fully damaged state (cracks) is represented as $v = 1$. A typical phase field fracture method is

$$\mathcal{E}^{\ell}(u, v) = \int_{\Omega} \alpha(v) W(\nabla u) + \frac{G}{4c_w} \left(\frac{w(v)}{\ell} + \ell |\nabla v|^2 \right) dx, \tag{6.2}$$

where $\alpha(v)$ is a monotonic function which is the rigidity of the material in the damage state v with $\alpha(0) = 1$ and $\alpha(1) = 0$, $w(v)$ the energy density dissipated by the material during a homogeneous damage process (also a monotonic function) with $w(0) = 0$ and $w(1) = 1$, $c_w = \int_0^1 \sqrt{w(v)} dv$ the normalized constant, and $\ell > 0$ the internal length (regularization parameter).

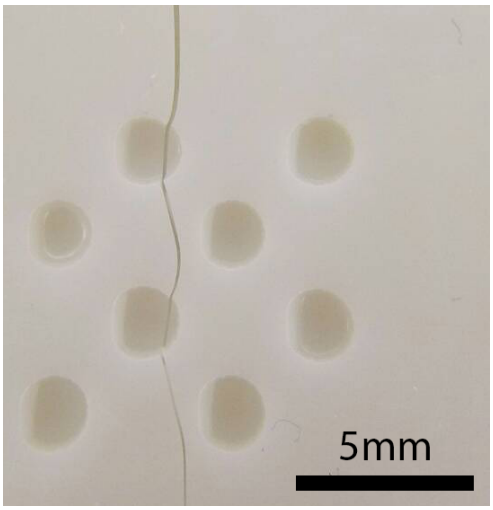

(a) experimental crack path

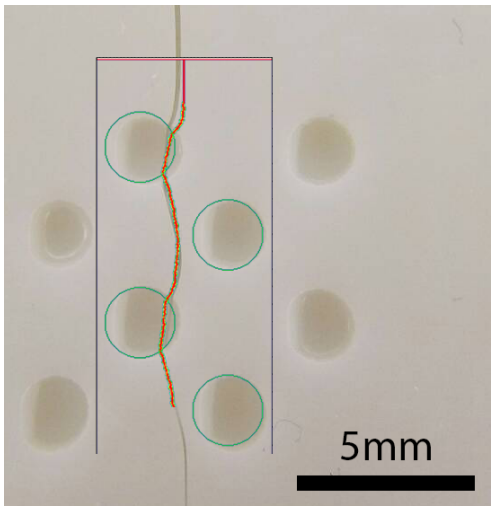

(b) phase field fracture method prediction

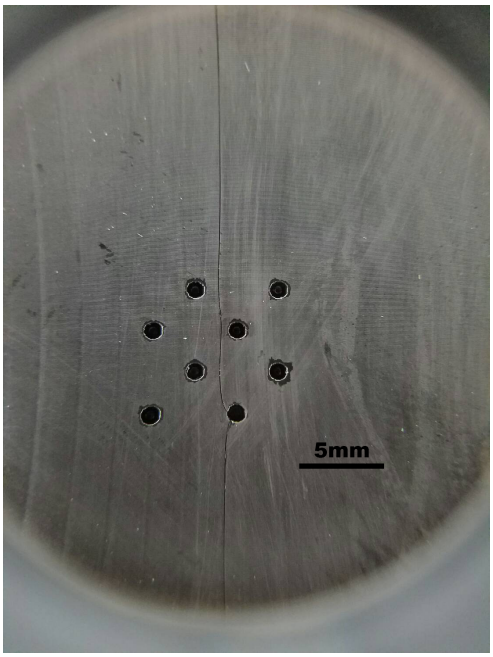

(c) experimental crack path

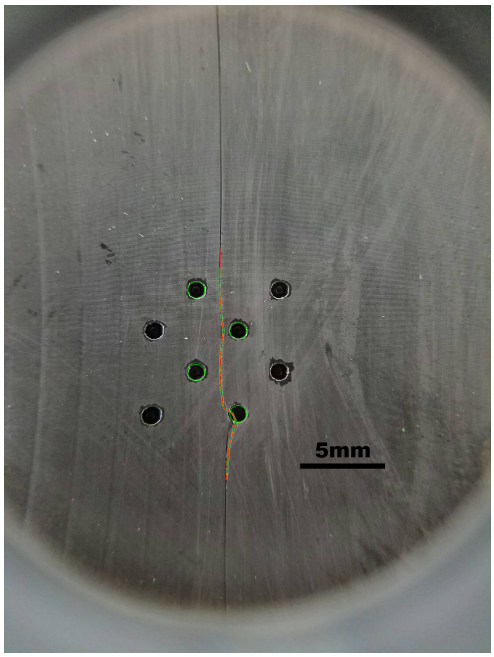

(d) phase field fracture method prediction

Figure 6.2: High agreement between actual crack path and the phase field fracture method prediction

This method have good agreement between the simulation result and the experimental result as shown in Figure 6.2.

The physical interpretation of the phase field model can be examined by applying this model to a material in a homogeneous state (v is constant

over the entire material so $\nabla v = 0$). If this material is undamaged ($v = 0$), the energy in the phase field model is identical with the energy in elasticity. If this material is fully damaged, there is no elastic energy and all the energy of the phase field model is contributed by the toughness. It can be rigorously shown that this phase field fracture method in equation (6.2) approximates (i.e., Γ-converges to) the classical brittle fracture model in equation (6.1) when the internal length (regularized parameter) approaches 0 [1].

We consider a domain Ω (a bounded open set in $\mathbb{R}^N$) subject to body force b. The boundary conditions are $u_i = u_i^*$ on $\partial_1\Omega$ and $\sigma_{ij}n_j = t_i^*$ on $\partial_2\Omega$. We also require that $\partial_1\Omega \cup \partial_2\Omega = \partial\Omega$ and $\partial_1\Omega \cap \partial_2\Omega = \emptyset$. If we apply the phase field fracture on this domain, the total energy is

$$\mathcal{P}^\ell(u, v) = \mathcal{E}^\ell(u, v) - \int_\Omega b_i u_i dx - \int_{\partial_2\Omega} t_i^* u_i ds. \tag{6.3}$$

In a quasi-static setting, we wish to find the solutions $u(x,t)$ and $v(x,t)$ under some external loading $b(x,t)$ and boundary conditions $u^*(x,t)$ and $t_i^*(x,t)$. We further impose the irreversible condition (the materials can not heal) which is

$$\dot{v}(x,t) \geq 0, \tag{6.4}$$

where the superimposed dot denotes the time derivative $\dot{(\,)} = \frac{\partial(\,)}{\partial t}$. Taking variation of the total energy in equation (6.3), we obtain

$$\begin{aligned}
\left.\frac{d\mathcal{P}(u + s\tilde{u}, v + s\tilde{v})}{ds}\right|_{s=0} = &\int_\Omega \left[\alpha'(v)W(\nabla u) + \frac{G}{4c_w}\left(\frac{w'(v)}{\ell} - 2\ell\nabla^2\right)\right. \\
&\left. - \frac{\ell}{2c_w}(\nabla G)\cdot(\nabla v)\right]\tilde{v}dx \\
&- \int_\Omega \left[\frac{\partial}{\partial x_j}\left(\alpha(v)\frac{\partial W(\nabla u)}{\partial F_{ij}}\right) + b_i\right]\tilde{u}_i dx \\
&+ \int_{\partial_2\Omega}\left[\left(\alpha(v)\frac{\partial W(\nabla u)}{\partial F_{ij}}\right)n_j - t_i^*\right]\tilde{u}_i dx \\
&+ \int_{\partial\Omega}\left(\frac{G\ell}{2c_w}\frac{\partial v}{\partial n}\right)\tilde{v}ds.
\end{aligned} \tag{6.5}$$

Minimization of the total energy subject to the irreversible condition requires

$$\left.\frac{d\mathcal{P}(u + s\tilde{u}, v + s\tilde{v})}{ds}\right|_{s=0} \geq 0 \qquad \text{with} \qquad \tilde{v} \geq 0. \tag{6.6}$$

Equation (6.6) implies the following constraints:
(i) damage inequality

$$\alpha'(v)W(\nabla u) + \frac{G}{4c_w}\left(\frac{w'(v)}{\ell} - 2\ell\nabla^2 v\right) - \frac{\ell}{2c_w}(\nabla G)\cdot(\nabla v) \geq 0 \quad \text{in } \Omega; \tag{6.7}$$

(ii) equilibrium equation

$$\frac{\partial}{\partial x_j}\left(\alpha(v)\frac{\partial W(\nabla u)}{\partial F_{ij}}\right) + b_i = 0 \quad \text{in } \Omega; \tag{6.8}$$

(iii) traction boundary condition

$$\left(\alpha(v)\frac{\partial W(\nabla u)}{\partial F_{ij}}\right) n_j = t_i^* \quad \text{on } \partial_2\Omega; \tag{6.9}$$

(iv) damage inequality on boundary

$$\frac{\partial v}{\partial n} \geq 0 \quad \text{on } \partial\Omega. \tag{6.10}$$

Furthermore, we have two more constraints by the energy balance:
(v) evolution law of the damage field

$$\left[\alpha'(v)W(\nabla u) + \frac{G}{4c_w}\left(\frac{w'(v)}{\ell} - 2\ell\nabla^2 v\right) - \frac{\ell}{2c_w}(\nabla G)\cdot(\nabla v)\right]\dot{v} = 0 \quad \text{in } \Omega; \tag{6.11}$$

(vi) evolution law of the damage field on boundary

$$\frac{\partial v}{\partial n}\dot{v} = 0 \quad \text{on } \partial\Omega. \tag{6.12}$$

The internal length ℓ is a key parameter in the phase field model. Since the damage field v is smooth and continuous, there must be a "transition zone" between a crack ($v = 1$) and the undamaged material ($v = 0$). One can show that the size of this transition zone is of order ℓ. Therefore, the damage zone shrinks to a surface (crack face) when $\ell \to 0$. Moreover, the internal length also determines nucleation: smaller internal length makes nucleation harder.

We reproduce a one dimensional example of Pham et al.[71] to demonstrate the effect of the internal length ℓ. Suppose we perform a (numerical) uniaxial test on a uniform 1D bar. The initial conditions and boundary conditions are

$$v(x, t = 0) = 0, \quad u(x, t = 0) = 0, \quad u(x = 0, t) = 0, \quad u(x = L, t) = u^*(t). \tag{6.13}$$

By assuming linear elasticity, we have

$$W = \frac{1}{2}E\left(\frac{\partial u}{\partial x}\right)^2 \implies \sigma = \alpha E\left(\frac{\partial u}{\partial x}\right). \tag{6.14}$$

Therefore, equations (6.7), (6.8), and (6.11) become:
(i) damage inequality

$$\alpha'(v)\frac{1}{2}E\left(\frac{\partial u}{\partial x}\right)^2 + \frac{G}{4c_w}\left(\frac{w'(v)}{\ell} - 2\ell\frac{\partial^2 v}{\partial x^2}\right) \geq 0 \quad x \in (0, L); \tag{6.15}$$

(ii) equilibrium equation

$$\frac{\partial \sigma}{\partial x} = 0 \implies \sigma = \text{constant} \quad x \in (0, L); \tag{6.16}$$

(v) evolution law of the damage field

$$\left[\alpha'(v)\frac{1}{2}E\left(\frac{\partial u}{\partial x}\right)^2 + \frac{G}{4c_w}\left(\frac{w'(v)}{\ell} - 2\ell\frac{\partial^2 v}{\partial x^2}\right)\right]\dot{v} = 0 \quad x \in (0, L). \tag{6.17}$$

We first consider the *homogeneous solution*, where α is a constant, $u(x,t) = \frac{u^* x}{L}$, and $\sigma(t) = \alpha E\frac{u^*}{L}$. Therefore, the damage inequality gives

$$\alpha'(v)\frac{1}{2}E\frac{u^{*2}}{L^2} + \frac{G}{4c_w}\left(\frac{w'(v)}{\ell}\right) \geq 0 \implies \frac{u^*}{L} \leq \sqrt{-\frac{G}{2Ec_w\ell}\frac{w'(v)}{\alpha'(v)}}. \tag{6.18}$$

According to the initial condition $v(x, t = 0) = 0$, we have the criterion for no damage in the bar, which is

$$\frac{u^*}{L} \leq \sqrt{-\frac{G}{2Ec_w\ell}\frac{w'(0)}{\alpha'(0)}}. \tag{6.19}$$

We can use this criterion to calculate the critical stress when the damage starts to evolve

$$\sigma_c = \sqrt{-\frac{GE}{2c_w\ell}\frac{w'(0)}{\alpha'(0)}}. \tag{6.20}$$

The homogeneous solution is stable in the elastic regime, i.e., when $\sigma < \sigma_c$ [71]. However, the homogeneous solution can be unstable when the load exceeds the critical stress (the stability depends on the geometry, the dissipation function $w(v)$ and the damage function $\alpha(v)$). If the homogeneous solution is unstable, a *localized solution* is formed.

In the localized solution, the damage is localized to a region whose size is controlled by the internal length ℓ. Assume that the damage is localized

in the region $(x_0 - a, x_0 + a)$ as shown in Figure 6.3. According to equation (6.17), we have

$$\alpha'(v)\frac{1}{2}E\left(\frac{\partial u}{\partial x}\right)^2 + \frac{G}{4c_w}\left(\frac{w'(v)}{\ell} - 2\ell\frac{\partial^2 v}{\partial x^2}\right) = 0 \quad x \in (x_0 - a, x_0 + a). \tag{6.21}$$

Since the damage field is smooth and continuous, we have the boundary condition

$$v(x_0 \pm a) = \frac{\partial v}{\partial x}(x_0 \pm a) = 0. \tag{6.22}$$

Although the strain is not constant in the localized solution, the stress $\sigma = \alpha E\frac{\partial u}{\partial x}$ is a constant through the entire bar. Therefore, we rewrite equation (6.21) as

$$\frac{\alpha'(v)}{\alpha^2(v)}\frac{1}{2E}\sigma^2 + \frac{G}{4c_w}\left(\frac{w'(v)}{\ell} - 2\ell\frac{\partial^2 v}{\partial x^2}\right) = 0 \quad x \in (0, L). \tag{6.23}$$

Multiplying the equation above by v and integrating with respect to x, we have

$$-\frac{1}{\alpha}\frac{\sigma^2}{2E} + \frac{G}{4c_w}\left[\frac{w}{\ell} - \ell\left(\frac{dv}{dx}\right)^2\right] = C_1, \tag{6.24}$$

where C_1 is a constant of integration. This constant C_1 can be determined by equation (6.22). Therefore, equation (6.24) becomes

$$\frac{G}{4c_w}\left[\frac{w}{\ell} - \ell\left(\frac{dv}{dx}\right)^2\right] = \frac{\sigma^2}{2E}\left(\frac{1}{\alpha} - 1\right), \tag{6.25}$$

or

$$\ell^2\left(\frac{dv}{dx}\right)^2 = w + \frac{2c_w\sigma^2\ell}{GE}\left(1 - \frac{1}{\alpha}\right). \tag{6.26}$$

Thus,

$$\ell\frac{dv}{dx} = \sqrt{w + \frac{2c_w\sigma^2\ell}{GE}\left(1 - \frac{1}{\alpha}\right)} \implies dx = \frac{\ell}{\sqrt{w + \frac{2c_w\sigma^2\ell}{GE}\left(1 - \frac{1}{\alpha}\right)}}dv. \tag{6.27}$$

Therefore, the size of transition zone a can be calculated by

$$a = \int_{x_0 - a}^{x_0} dx = \int_0^{v_{\max}} \frac{\ell}{\sqrt{w + \frac{2c_w\sigma^2\ell}{GE}\left(1 - \frac{1}{\alpha}\right)}}dv. \tag{6.28}$$

We see that the size of the transition zone is controlled by the internal

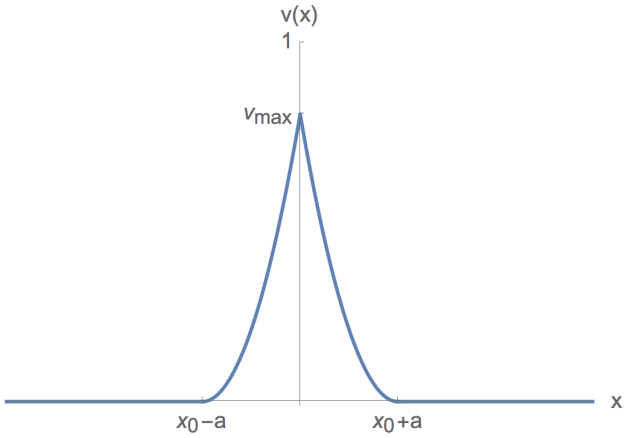

Figure 6.3: Damage profile near the localized damage zone

length ℓ and also the stress σ. Furthermore, substituting equation (6.25) into equation (6.2), we have

$$\mathcal{E}^\ell = \frac{\sigma^2 L}{2E} + \frac{G}{2c_w \ell}\int_{x_0-a}^{x_0+a} w dx \tag{6.29}$$

$$= \frac{\sigma^2 L}{2E} + \frac{G}{c_w \ell}\int_{x_0-a}^{x_0} w dx \tag{6.30}$$

$$= \frac{\sigma^2 L}{2E} + \frac{G}{c_w}\int_0^{v_{\max}} \frac{w}{\sqrt{w + \frac{2c_w\sigma^2\ell}{GE}\left(1-\frac{1}{\alpha}\right)}} dv. \tag{6.31}$$

In fracture mechanics, a crack can be viewed as a localized damage zone where the equilibrium stress on it is 0. Thus, we required that $v_{\max} = 1$ in order to have the equilibrium stress zero. Substituting $\sigma = 0$ and $v_{\max} = 1$ into equation (6.28) to get the size of the transition zone,

$$a = \int_0^1 \frac{\ell}{\sqrt{w}} dv. \tag{6.32}$$

We can see that the size of the transition size is linearly dependent on the internal length ℓ. Furthermore, substituting $\sigma = 0$ into equation (6.31) gives

$$\mathcal{E}^\ell = \frac{G}{c_w}\int_0^1 \sqrt{w} dv. \tag{6.33}$$

The equation above shows that the constant c_w has to be equal to $\int_0^1 \sqrt{w} dv$ so the energy of the localized damage region (crack) is G.

A common choice of the function $\alpha(v)$ and $w(v)$ is

$$\alpha(v) = (1-v)^2, \qquad w(v) = v. \tag{6.34}$$

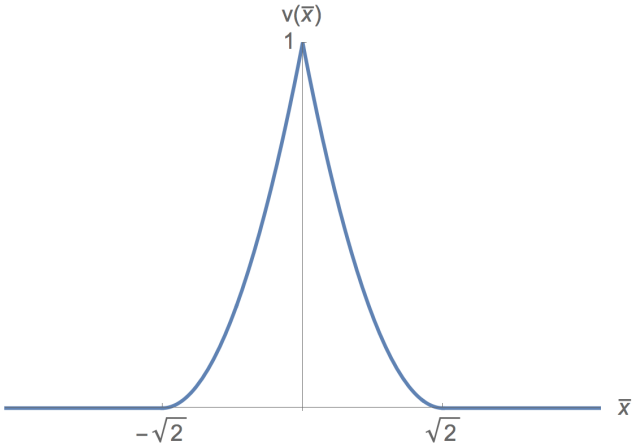

Figure 6.4: Damage profile near the localized damage zone ($\bar{x} := \frac{x}{\ell}$)

In this situation, the normalization constant $c_w = \int_0^1 \sqrt{v} dv = \frac{2}{3}$. The critical stress can be calculated by equation (6.20):

$$\sigma_c = \sqrt{\frac{3GE}{8\ell}}. \tag{6.35}$$

The size of the transition zone can be calculated by equation (6.32):

$$a = \int_0^1 \frac{\ell}{\sqrt{v}} dv = \sqrt{2}\ell. \tag{6.36}$$

Finally, the damage profile near the transition zone is

$$v(x) = \begin{cases} \left(1 - \frac{|x - x_0|}{\sqrt{2}\ell}\right)^2 & x \in [x_0 - a, x_0 + a] \\ 0 & x \in [0, L] \setminus [x_0 - a, x_0 + a], \end{cases} \tag{6.37}$$

which is shown in Figure 6.4.

6.2 Parameter optimization

Consider a material which contains 2-dimensional square array of circular inclusions as shown in Figure 6.5. We want to study the relationship between the microstructure and the effective stiffness and effective toughness.

To compute the effective stiffness, we use a fast Fourier transform (FFT) scheme to calculate the response of a unit cell [57, 61, 62]. Suppose we have a unit cell of inhomogeneous material with the periodic boundary condition and elastic tensor $\mathbb{C}_{ijkl}(x)$. The constitutive relationship can be

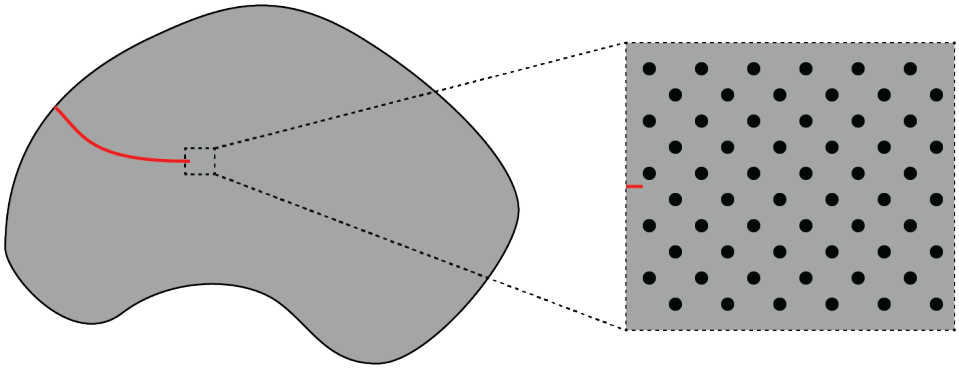

Figure 6.5: Material with a square array of inclusions

expressed as

$$\sigma_{ij} = \mathbb{C}_{ijkl}\varepsilon_{kl} = \mathbb{C}^{o}_{ijkl}\varepsilon_{kl} + \left[\mathbb{C}_{ijkl} - \mathbb{C}^{o}_{ijkl}\right]\varepsilon_{kl}, \tag{6.38}$$

where $\mathbb{C}^{o}_{ijkl}$ is a constant reference elastic tensor. Define the polarization field

$$\tau_{ij} = \left[\mathbb{C}_{ijkl} - \mathbb{C}^{o}_{ijkl}\right]\varepsilon_{kl}. \tag{6.39}$$

Thus, the stress can be represented as

$$\sigma_{ij} = \mathbb{C}^{o}_{ijkl}\varepsilon_{kl} + \tau_{ij} \tag{6.40}$$

and the equilibrium equation

$$\sigma_{ij,j} = 0. \tag{6.41}$$

Taking the Fourier transform of equation (6.40) and (6.41) gives

$$\widehat{\sigma}_{ij} = i\mathbb{C}_{ijkl}\widehat{u}_k k_l + \widehat{\tau}_{ij} \tag{6.42}$$

and

$$i\widehat{\sigma}_{ij}k_j = 0. \tag{6.43}$$

Substitute equation (6.42) into equation (6.43) and get

$$(\mathbb{C}^{o}_{ijkl}k_j k_l)\widehat{u}_k = i\widehat{\tau}_{ij}k_j \implies K_{ik}\widehat{u}_k = i\widehat{\tau}_{ij}k_j, \tag{6.44}$$

where $K_{ik} := \mathbb{C}^{o}_{ijkl}k_j k_l$. Take $N = K^{-1}$,

$$\widehat{u}_i = iN_{ip}\widehat{\tau}_{pq}k_q = \frac{i}{2}\left(N_{ip}k_q + N_{iq}k_p\right)\widehat{\tau}_{pq}. \tag{6.45}$$

Finally,

$$\widehat{\varepsilon}_{ij} = \frac{i}{2}\left(k_i\widehat{u}_j + k_j\widehat{u}_i\right) = -\frac{1}{4}\left(N_{jk}k_ik_l + N_{jl}k_ik_k + N_{ik}k_jk_l + N_{il}k_jk_k\right)\widehat{\tau}_{kl} = -\widehat{\Gamma}_{ijkl}\widehat{\tau}_{kl}, \tag{6.46}$$

where $\widehat{\Gamma}_{ijkl} = \frac{1}{4}\left(N_{jk}k_ik_l + N_{jl}k_ik_k + N_{ik}k_jk_l + N_{il}k_jk_k\right)$. For homogeneous isotropic reference materials, we have

$$\begin{aligned} \mathbb{C}^0_{ijkl} &= \lambda\delta_{ij}\delta_{kl} + \mu(\delta_{ik}\delta_{jl} + \delta_{il}\delta_{jk}) \\ K_{ij} &= (\lambda+\mu)k_ik_j + \mu|\boldsymbol{k}|^2\delta_{ij} \\ N_{ij} &= \frac{1}{\mu|\boldsymbol{k}|^2}\left(\delta_{ij} - \frac{\lambda+\mu}{\lambda+2\mu}\frac{k_ik_j}{|\boldsymbol{k}|^2}\right) \end{aligned}. \tag{6.47}$$

Therefore,

$$\widehat{\Gamma}^0_{ijkl} = \frac{1}{4\mu|\boldsymbol{k}|^2}\left(\delta_{ik}k_jk_l + \delta_{il}k_jk_k + \delta_{jk}k_ik_l + \delta_{jl}k_ik_k\right) - \frac{\lambda+\mu}{\mu(\lambda+2\mu)}\frac{k_ik_jk_kk_l}{|\boldsymbol{k}|^4}. \tag{6.48}$$

We can use the algorithm in Table 6.1 to calculate the response of the unit cell. Finally, the effective stiffness can be determined by the relationship

$$< \sigma_{ij} >= \mathbb{C}^{\text{eff}}_{ijkl} < \varepsilon_{kl} >, \tag{6.49}$$

where $< \sigma_{ij} >$ and $< \varepsilon_{ij} >$ are the overall stress and strain, respectively.

For the effective toughness, we use the phase field fracture method to study crack propagation over multiple periods as shown in Figure 6.6. We apply the surfing boundary condition

$$u^*(x_1, x_2, t) = U(x_1 - t, x_2), \tag{6.50}$$

where U is the K_I field in equation (3.2) with stress intensity factor 1. This surfing boundary is applied on the entire boundary of the domain. The unit cell size is 8×8 and the entire domain size is 42×8. The shortest distance between two inclusions is $4\sqrt{2}$. The elastic modulus and the toughness of the matrix material are both set as 1. The internal length of the matrix and the inclusion material are both 0.45. Therefore, the remaining parameters of the microstructure we can adjust are (i) the radius of the inclusions, (ii) the stiffness of the inclusions, and (iii) the toughness of the inclusions.

initialization:

Set the average strain field $< \varepsilon_{pq} >= E_{pq}$

Set the reference elastic tensor $\mathbb{C}^{o}_{pqrs}$

Set tolerance ξ;

Set the initial guess σ^{o}_{pq} and ε^{o}_{pq}

Calculate the Green operator in Fourier space $\widehat{\Gamma}^{o}_{pqrs}$

repeat

Update the polarization field.

$$\tau^{i}_{pq} = \sigma^{i}_{pq} - \mathbb{C}^{o}_{pqrs}\varepsilon^{i}_{rs}$$

FFT on polarization field

$$\widehat{\tau_{pq}}^{i} = \mathcal{F}\{\tau^{i}_{pq}\}$$

Calculate the strain in Fourier space

$$\widehat{\varepsilon}^{i+1}_{pq}(k) = -\widehat{\Gamma}^{o}_{pqrs}(k)\widehat{\tau}^{i}_{rs}(k) \text{ for all } k \neq o$$

$$\widehat{\varepsilon}^{i+1}_{pq}(o) = E_{pq}$$

IFFT on the strain field:

$$\varepsilon^{i+1}_{pq} = \mathcal{F}^{-1}\{\widehat{\varepsilon}^{i+1}_{pq}\}$$

Update the stress field

$$\sigma^{i+1}_{pq} = \mathbb{C}_{pqrs}\varepsilon^{i+1}_{rs}$$

until *Difference* $||\sigma^{i+1}_{pq} - \sigma^{i}_{pq}|| \leq \xi$;

Table 6.1: Pseudo-code for computing the elastic response of a unit cell with periodic boundary conditions

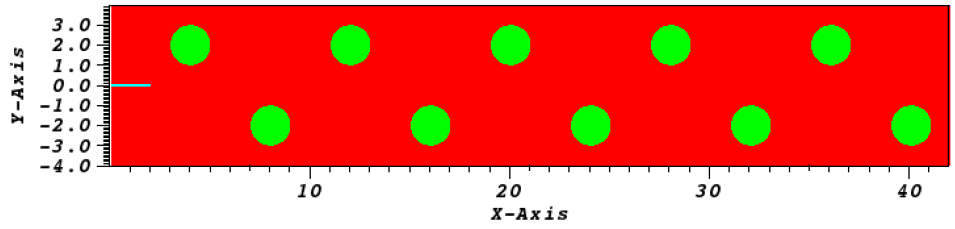

Figure 6.6: Simulation domain (red is the matrix and green is the inclusions)

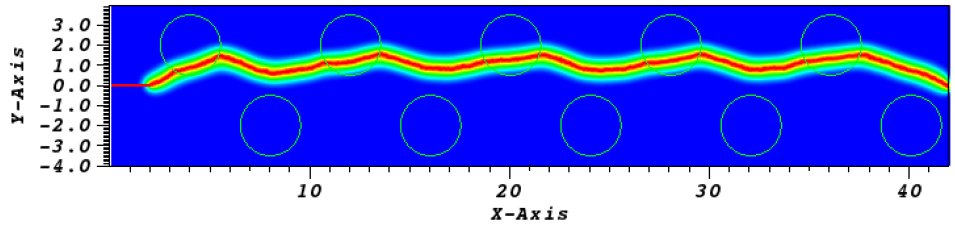

(a) crack path

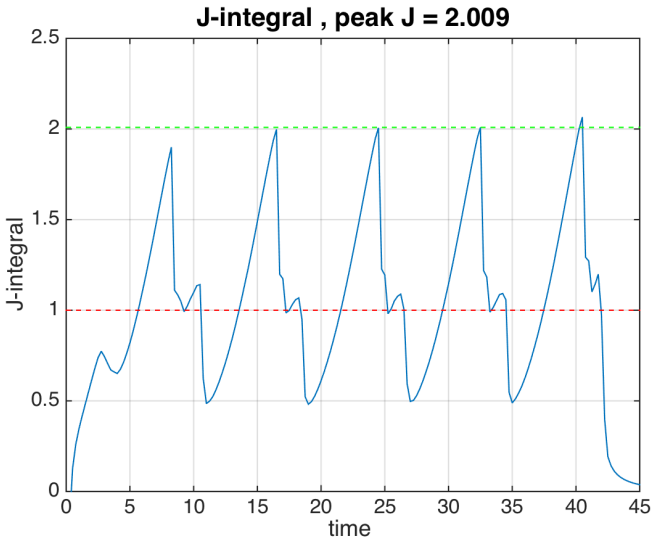

(b) J-integral

Figure 6.7: Simulation of material with square array of inclusions where the radius of inclusion is 1.5 (the red line is the ingredient toughness and the green line is the effective toughness)

We first adjust the radii of the inclusions while the stiffness and the toughness of inclusions are fixed at 0.1 and 1 respectively. Note that under this scenario, the toughness of the entire material is uniformly 1. We first use the inclusions with radius 1.5 and show the crack path and the J-integral in Figure 6.7.

We can see that the compliant inclusions attract the crack so the crack deviates into the inclusions as shown in Figure 6.7 (a). Furthermore, we can see that the J-integral is oscillating as shown in Figure 6.7 (b). We define the effective toughness as the peak of the J-integral when the crack is propagating in the heterogeneous material. The J-integral goes to a peak value 2.009 when the crack tip approaches the interface in the compliant inclusions. In other words, even though the pointwise toughness is uniformly 1, the effective toughness is 2.009. The effective toughness is more than 100%

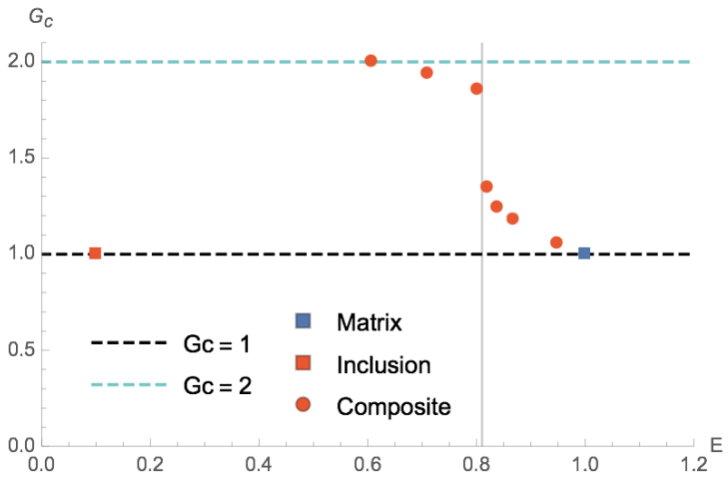

Figure 6.8: Effective toughness and effective stiffness of the material with square array of inclusions (stiffness contrast 10, internal length $\ell = 0.45$)

higher than that of each constituent.

We also change the radii of the inclusions (with fixed the material of the inclusions) and calculate the effective behavior of the microstructure. The results are shown in Figure 6.8. In this figure, the dashed black line indicates the materials with toughness 1. The blue square dot is the matrix material and the red square dot is the inclusion material. The red circular dots are the effective behavior of the heterogeneous materials. The simulation results show that when the inclusion radius is increased, the effective stiffness decreases and the effective toughness increases. Moreover, there is clearly a transition zone (the vertical gray line in the Figure 6.8) where the effective toughness has a dramatic jump across the transition zone but only a small trade off on the stiffness. Importantly, note that the composite material can have almost twice the toughness while retaining 80% of the stiffness of the matrix. We now study the crack path and J-integral before and after the transition zone as shown in Figure 6.9 and 6.10. Consider the case before the transition zone (the radius of the inclusions is 0.95 which is the red dot on the right side of the vertical gray line in Figure 6.8). The crack path and the J-integral of this microstructure are shown in Figure 6.9. The crack path oscillates between the inclusions but does not penetrate into the inclusions. As a result, the J-integral oscillates with peak value 1.348. Now consider the case after the transition zone (the radius of the inclusions is 1.0, which is the red dot on the left side of the vertical gray line in

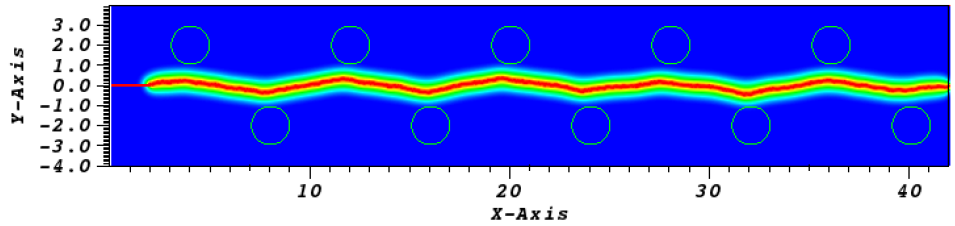

(a) crack path

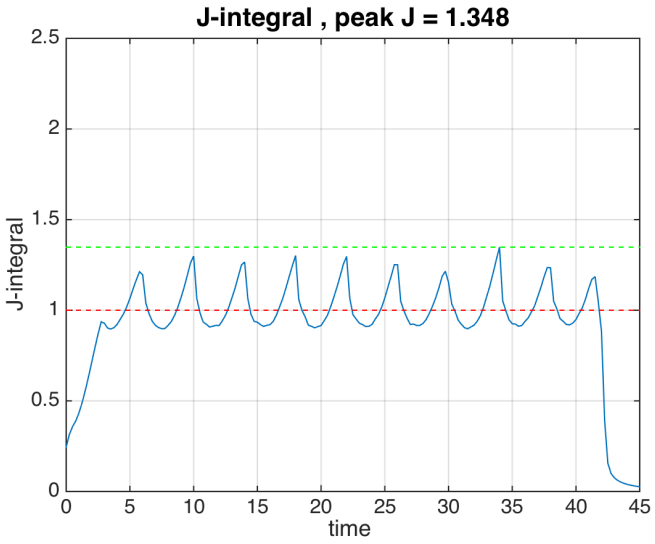

(b) J-integral

Figure 6.9: Simulation of material with square array of inclusions where the radius of inclusion is 0.95 (the red line is the ingredient toughness and the green line is the effective toughness)

Figure 6.8). After some transient region, the crack penetrates the inclusions and is pinned before it renucleates. The J-integral reaches 1.85 just prior to renucleation. Thus, the transition to high effective toughness is the result of penetration, trapping, and renucleation.

We also study how different inclusion stiffness affects the effective toughness. We use the inclusion with stiffness 0.025, 0.25, and 0.5 and the results are plotted as purple, green, and yellow dots in Figure 6.11 respectively. The qualitative behavior is similar. Specifically, we observe that there is a transition zone in the toughness-stiffness figure, and this is related to penetration, pinning and renucleation. Interestingly, there is an optimal elastic contrast.

Finally, we study the relation between the inclusion toughness and the effective toughness. In this study, we fix the stiffness of inclusion at 0.1

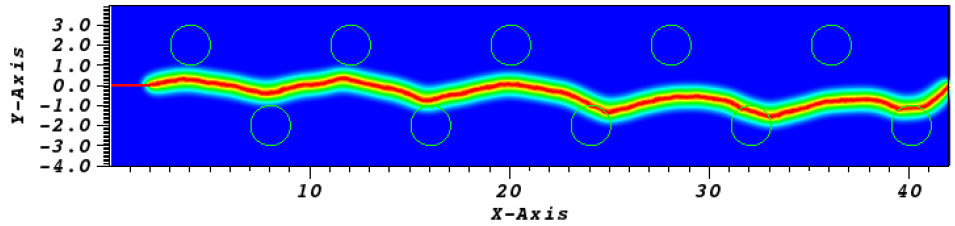

(a) crack path

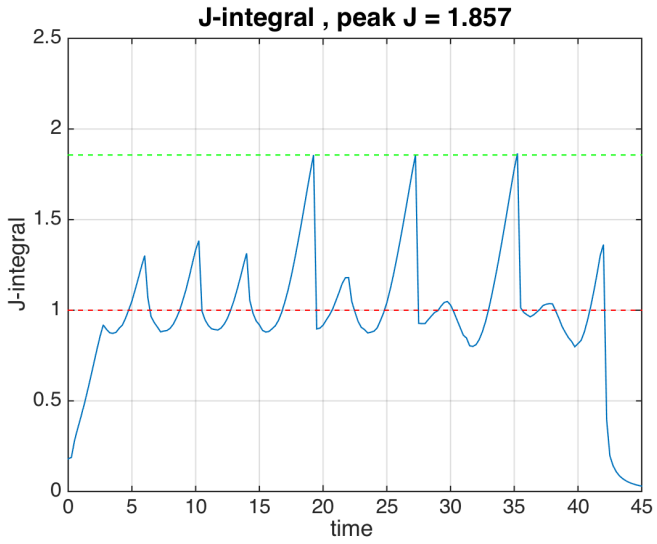

(b) J-integral

Figure 6.10: Simulation of material with square array of inclusions where the radius of inclusion is 1.0 (the red line is the ingredient toughness and the green line is the effective toughness)

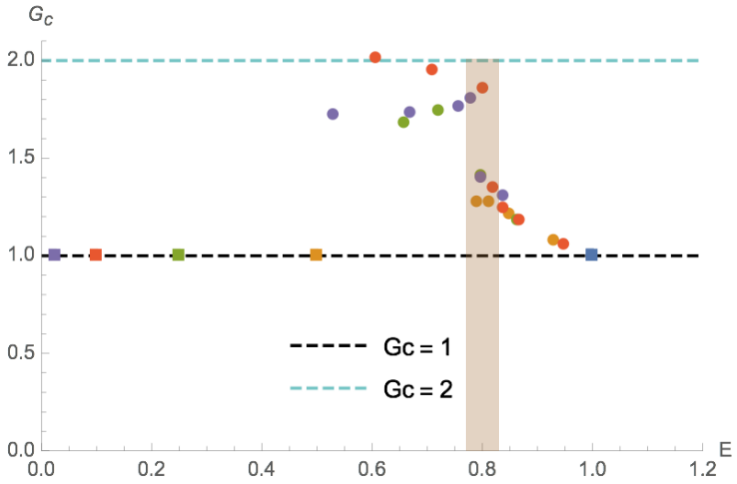

Figure 6.11: Effective toughness and effective stiffness of the material with square array of inclusions

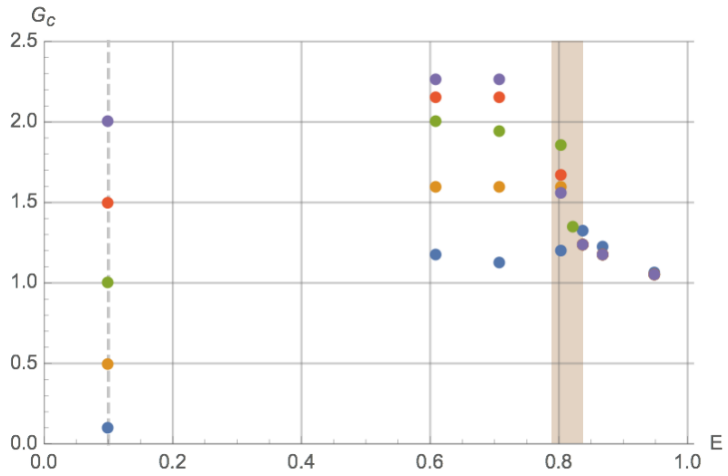

Figure 6.12: Effect of inclusion toughness on effective toughness (fix inclusion stiffness 0.1)

and vary the toughness of the inclusions. We use inclusion toughness 0.1, 0.5, 1.0, 1.5, and 2.0, and plot the effective toughness in Figure 6.12. The inclusion is shown as the dots on vertical dashed line in Figure 6.12. We can see that there is a transition zone around the effective stiffness around 0.8. The inclusion toughness does not significantly affect before the transition zone (right of the transition zone). However, the inclusion toughness can significantly affect the effective behavior after the transition zone (left of the transition zone). Furthermore, higher inclusion toughness leads to higher effective toughness. We define the toughening as

$$\text{Toughening ratio} = \frac{\text{effective toughness}}{\max\left(\text{ matrix toughness }, \text{ inclusion toughness }\right)} \tag{6.51}$$

and plot the toughening ratio in Figure 6.13. We see that there is an optimal toughness ratio between matrix and inclusions for maximize toughening ratio.

In summary, we study the effective properties of a bimaterial composite. We find that the effective toughness can be significantly enhanced with relatively little loss of stiffness where the matrix is stiff and inclusions compliant. There is optimal contrast.

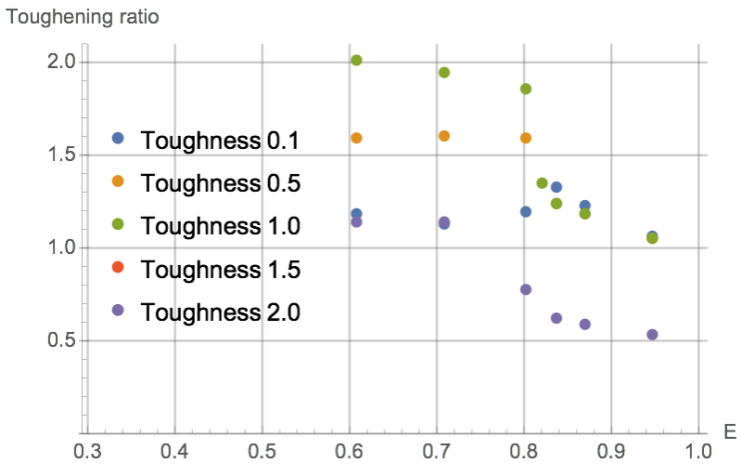

Figure 6.13: Effect of inclusion toughness on toughening ratio (fix inclusion stiffness 0.1)

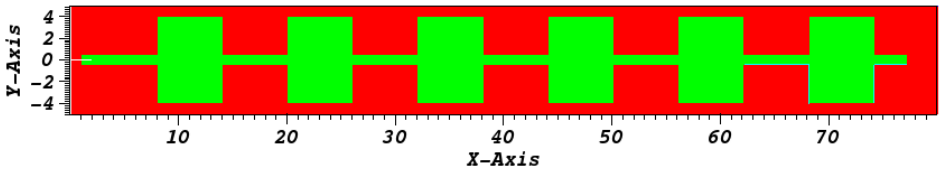

(a) cross microstructure

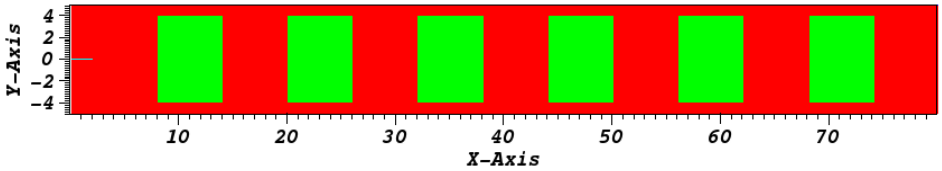

(b) stripe microstructure

Figure 6.14: Two kind of microstructures for studying toughening mechanism

6.3 Elastic contrast with and without renucleation

In the previous section, we see two kinds of toughening mechanism. When the crack propagates but does not go into the inclusions, there is toughening due to stress heterogeneity. When the crack propagates from the inclusions to the matrix material, there is additional toughening mechanism due to the need for renucleation. In order to study these two toughening mechanisms, we study two microstructures as shown in Figure 6.14. We called the microstructure shown in Figure 6.14 (a) the cross microstructure and the microstructure shown in Figure 6.14 (b) the stripe microstructure. The only difference between these two microstructures is that we put a thin stripe with inclusion material in the center of the domain.

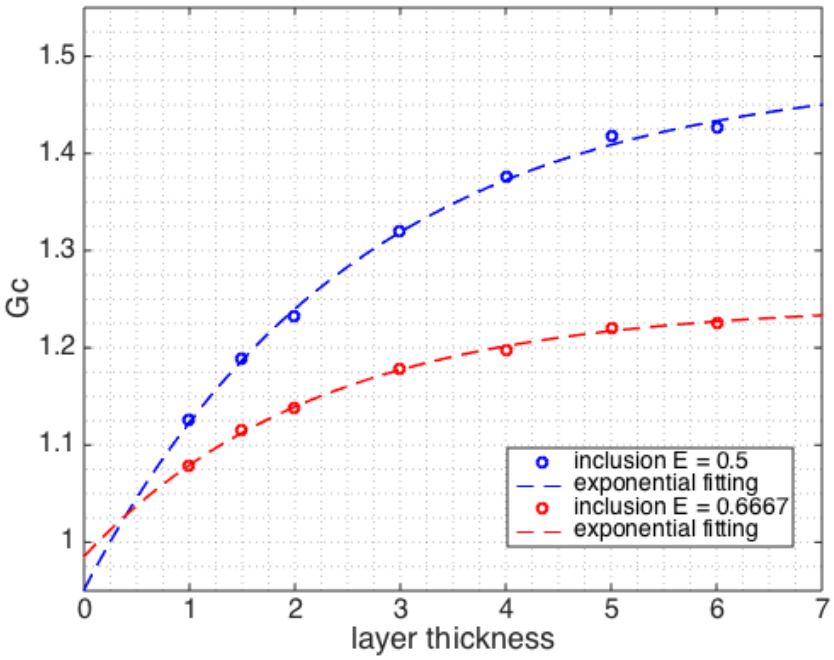

Figure 6.15: Effective toughness of the cross microstructure

When a crack propagates in the center of the cross structure, the crack always stay in the same material. Therefore, there is only stress heterogeneity. On the other hand, when a crack propagates in the stripe microstructure, both stress heterogeneity and renucleation happen.

We first use the cross microstructure in which the matrix material is 50% stiffer than the inclusion material (the stiffness of the matrix and the inclusion material is 1 and 0.6667 respectively). The internal length is 0.45 for both materials. We change the layer thickness and show the effective toughness as red dots in Figure 6.15. We see that the effective toughness increases when the layer thickness increases. Furthermore, the effective toughness converges when the layer thickness is high. We then use the same cross microstructure with higher elastic contrast. In this case, elastic modulus of the inclusion is reduced to 0.5 (therefore, the matrix is 100% stiffer than the inclusion material). The effective toughness with respect to different layer thickness is shown as blue dots in Figure 6.15. The trend is similar with previous case but the toughening mechanism is stronger because the higher elastic contrast.

In order to estimate the elastic heterogeneity toughening mechanism when

the layer thickness is very large, we propose a simple model to estimate it. Consider a bi-materials system which contains two materials with stiffness E_1 and E_2. Suppose there is a vertical interface separating these two materials. We apply macroscopic strain in the vertical direction so that both material have the same vertical strain. Thus, the average strain field can be represented as

$$< \varepsilon >= \frac{< \sigma >}{< E >} = \varepsilon^i = \frac{\sigma^i}{E^i} \quad \Longrightarrow \quad \frac{\sigma^i}{< \sigma >} = \frac{E^i}{< E >} \qquad i = 1, 2, \tag{6.52}$$

where the superscript indicates the materials and $< \cdot >$ indicates the volume average. From the Irwin's formula $G = \frac{K_I^2}{E}$, we can estimate the energy release rate as

$$G = \frac{K_I^2}{E} \sim \frac{\sigma^2}{E}. \tag{6.53}$$

Therefore,

$$\frac{G^i}{< G >} = \frac{\frac{\sigma^{i\,2}}{E^i}}{\frac{<\sigma>^2}{<E>}} = \frac{< E >}{E^i} \quad \Longrightarrow \quad < G >= \frac{< E >}{E^i} G^i. \tag{6.54}$$

By applying this simple model, we can estimate that $< G >= \frac{\frac{1+0.6667}{2}}{0.6667} \times 1 = 1.25$ if the inclusion stiffness is 0.6667. For the inclusion stiffness is 0.5, the effective toughness calculated by this simple model is $< G >= \frac{\frac{1+0.5}{2}}{0.5} \times 1 = 1.5$. We use the exponential fitting $G = c_0 + c_1 e^{-\frac{t}{c_3}}$, where G is the effective toughness, t is the layer thickness and $\{c_1, c_2, c_3\}$ are the fitting parameters. The best fitting lines are shown as dashed lines in Figure 6.15. These two best fitting lines predict that when then layer thickness goes to very high, the effective toughness converges to 1.244 and 1.485 for inclusion stiffness is 0.6667 and 0.5 respectively. These values are very close to the predictions of the simple model.

In order to study renucleation, we study the stripe microstructure as shown in Figure 6.14(b). We use the same inclusion materials (stiffness is 0.6667 and 0.5) and change the layer thickness. The results are shown as red lines in Figure 6.16. Since the blue lines are the result of the cross microstructure, the difference between red and blue lines represent the renucleation toughening (vertical arrows in Figure 6.16).

In order to study renucleation effect, we consider a crack propagates from one material to another material. The crack tip lies on the interface as

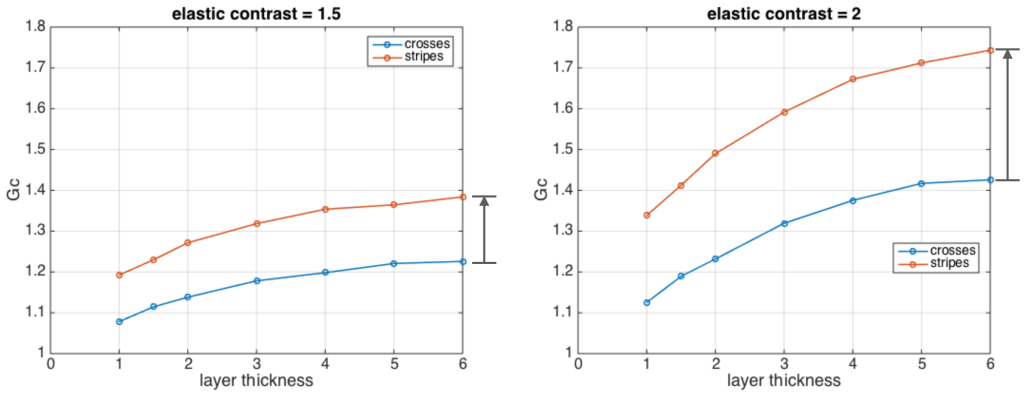

Figure 6.16: Re-nucleation toughening mechanism

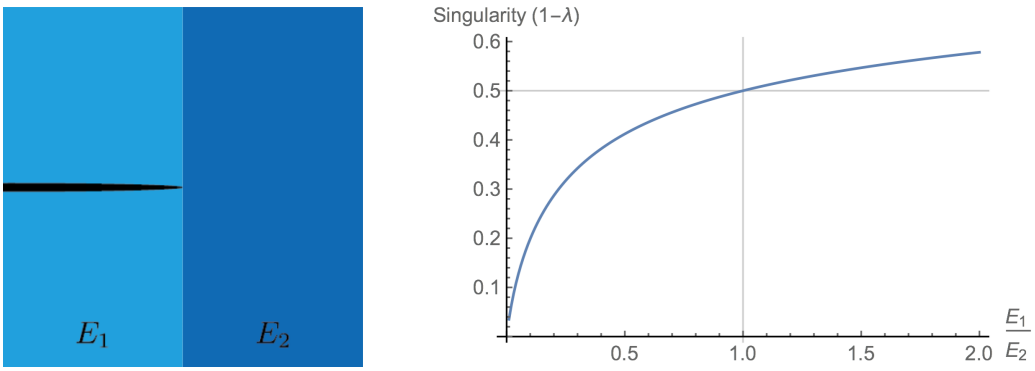

(a) Geometry

(b) Singularity strength

Figure 6.17: Crack tip in bi-material interface

shown in Figure 6.17 (a). Zak and Williams studied the stress singularity of this system [89]. They show that the stress near the crack tip is singular

$$\sigma \sim r^{-(1-\lambda)} \tag{6.55}$$

and the singularity strength $1-\lambda$ is determined by the elastic contrast of the bi-material system as shown in Figure 6.17(b). This study shows that the stress singularity is weaker than a traditional crack when $E_1 < E_2$.

Similarly, the stress singularity of an angle notch is weaker than a traditional crack as shown in Figure 6.18. In this figure we observe that when the angle is 0, which is a traditional sharp crack, the singularity is 0.5. On the other hand, the singularity vanishes ($1-\lambda \to 0$) when the angle approach to $\frac{\pi}{2}$. Therefore, an angle notch and a crack propagating from one material to another material is similar.

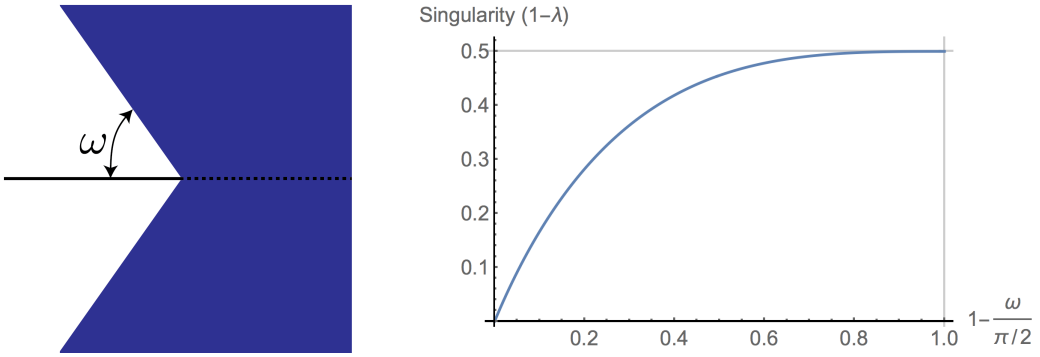

(a) Angle notch (b) Singularity strength

Figure 6.18: An angle notch has weaker singularity

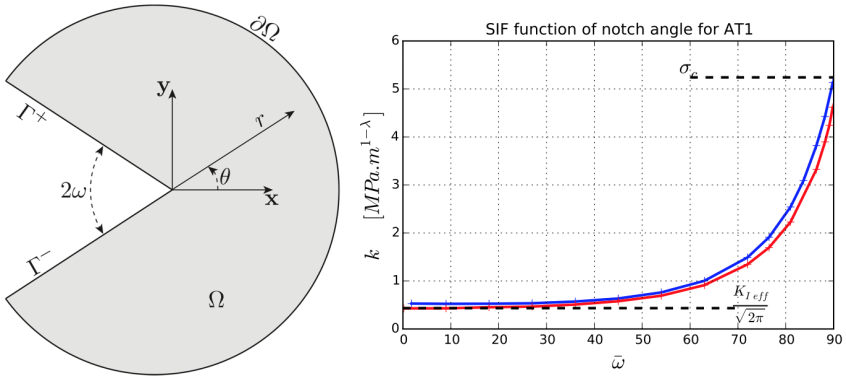

Figure 6.19: Angle notch studies by Tanné et al. [?]

Tanné et al. [82] have studied the angle notch nucleation by using the phase field fracture method. The results are shown in Figure 6.19. This model recovers two classical scenarios on the notch angle is extreme small and extreme large cases. When the notch angle is extremely large, the phase field model approaches the elasticity: the material failure at $\sigma = \sigma_c$. When the notch angle is extremely small, the phase field model approaches the classical fracture mechanics (the crack nucleation at $K_I = K_{Ic}$).

We can connect the crack renucleation in a bi-material system and an angle notch nucleation by comparing the singularity strength as shown in Figure 6.20 (a). Then we can extract the toughening calculated by Tanné et al. and use it to estimate the renucleation toughening mechanism. The results are shown in Figure 6.20 (b). The blue line is the estimated renucleation toughening and the red dots are the values obtained by our stripes and cross calculations. We see good agreement.

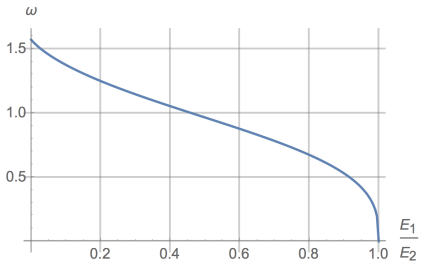

(a) Match angle notch with bi-material interface by singularity comparison

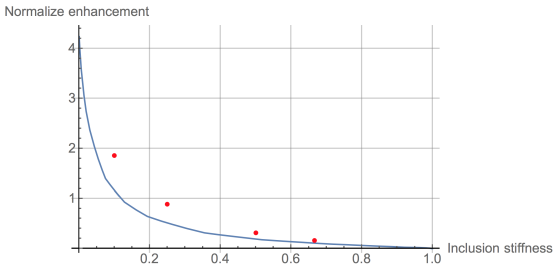

(b) Casual estimation of renucleation toughening mechanism

Figure 6.20: Casual estimation of the renucleation toughening mechanism

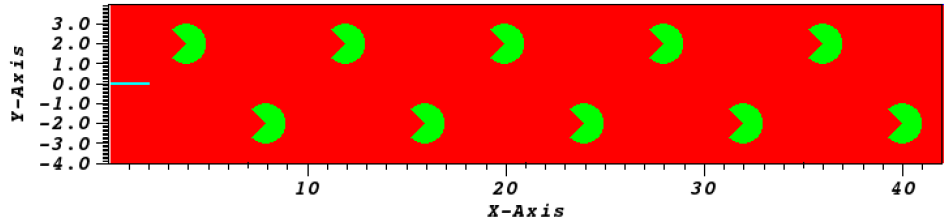

(a) Left-facing pacman

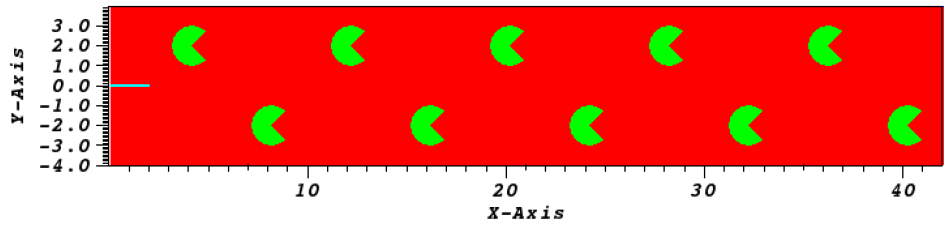

(b) Right-facing pacman

Figure 6.21: Pacman inclusion

6.4 Asymmetric toughness

We saw in Section 5.4 that asymmetric effective toughness can be achieved by using asymmetric microstructures. In this section, we use the same 2D square microstructure but with asymmetric inclusions. The asymmetric inclusions we use are the "pacman" inclusions as shown in Figure 6.21. The matrix material is set at stiffness 1 and toughness 1. The inclusion material parameter is set as stiffness 0.1 and toughness 1. Both material have the same internal length 0.45.

We then study crack propagation with different radii and different facing directions of pacman inclusions. The results are shown in Figure 6.22. The yellow line indicates the left-facing pacman inclusions and the green

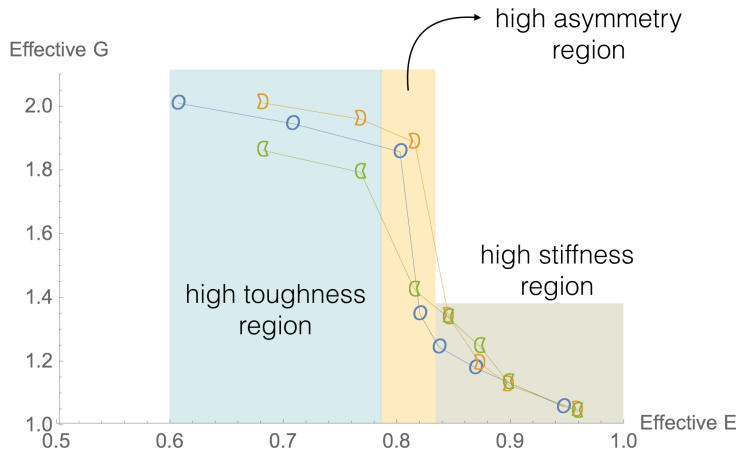

Figure 6.22: Asymmetric toughness

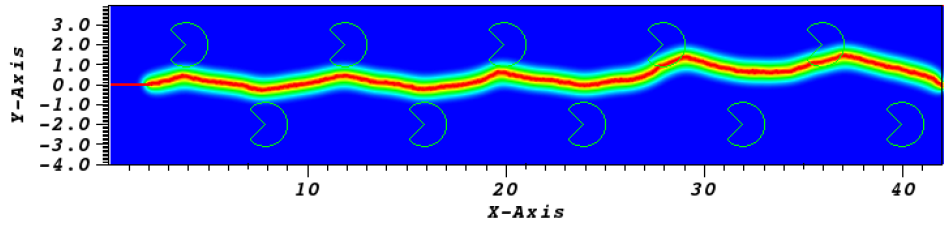

(a) Left-facing pacman

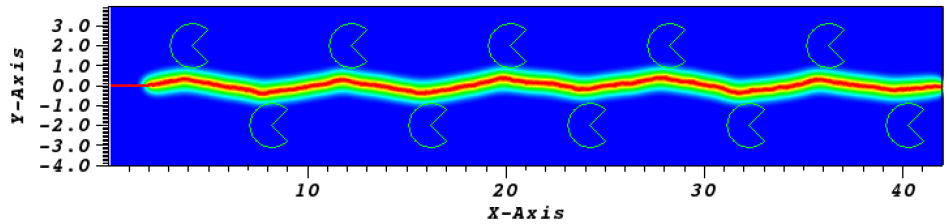

(b) Right-facing pacman

Figure 6.23: Pacman inclusion

indicates the right-facing inclusions. The blue line is the circular inclusion in the previous section.

For the small inclusion region (high effective stiffness region), the effective toughness is low and the asymmetry is also very small. When the inclusion size is moderate (effective stiffness is around 0.8), there is a high asymmetry region that maximizes the asymmetry. For large inclusion sizes, the effective toughness is large but the asymmetry is moderate. Therefore, we can choose a particular inclusion size with respect to the objective we need (high toughness / high stiffness / high asymmetry).

In order to understand why the high asymmetry region appears at mod-

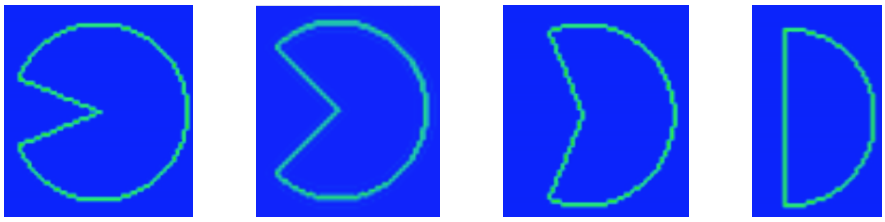

(a) 45 degree (b) 90 degree (c) 135 degree (d) 180 degree

Figure 6.24: Pacman inclusion with different angles

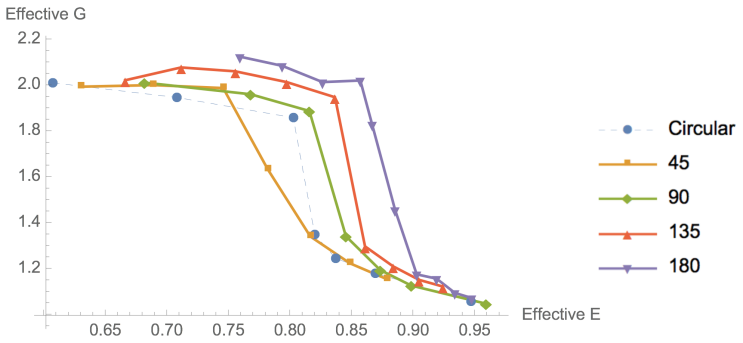

Figure 6.25: Left-facing pacman inclusion with different notch angle

erate inclusion size, we study the crack path shown in Figure 6.23 for the case with effective stiffness around 0.8. We can see that the crack propagates into the left-facing pacman inclusions but it does not propagate into the right-facing inclusions. As a result, the left-facing pacman microstructure has much higher effective toughness than the right-facing pacman microstructure because it has an additional renucleation toughening mechanism.

We also study the effects of the notch angle of the pacman. We use four different notch angles as shown in Figure 6.24. We first show the effective toughness of left-facing pacman inclusions in Figure 6.25. In this figure, we can observe that the higher notch angle makes the transition zone appear earlier (the transition zone appear in higher stiffness region). The reason for this phenomenon is that a higher notch angle leads to a taller inclusion (the inclusion is longer in vertical direction). As a result, the crack can easily propagate into the inclusions and make the transition zone appear earlier (with fixed inclusion radius).

The effective toughness of right-facing pacman inclusions is shown in Fig-

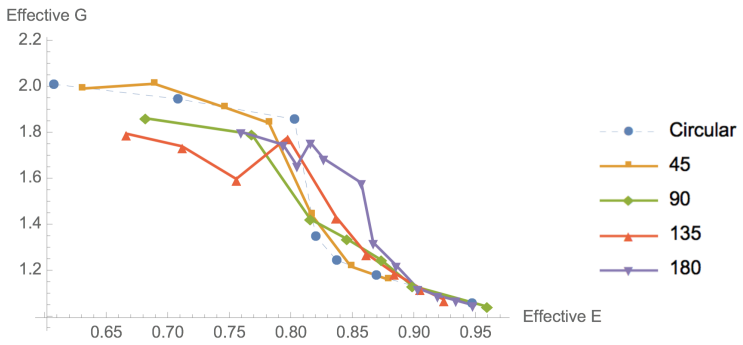

Figure 6.26: Right-facing pacman inclusion with different notch angle

ure 6.26. In this figure, the transition zone also appears earlier when the notch angle is larger. However, there is a drop in effective toughness after the transition zone for large notch angle inclusions (135 and 180 degrees).

In order to understand the drop in effective toughness for large notch angle inclusions, we plot the crack path of the 135 degree right-facing pacman inclusions near the drop in Figure 6.27. We can see that the crack goes to the other row when the inclusion size is increasing. This phenomenon makes the distance between the pinned state (the crack in inclusions propagates towards the interface between the matrix and the inclusion) and the next inclusion decrease drastically. Therefore, the peak driving force at the pinned state is decreasing (the next inclusion can attract the crack jump out of the pinned state). This phenomenon also affects the effective toughness after the transition zone (the low stiffness region). We can observe that the effective toughness after the transition zone decreases when the notch angle increases as shown in Figure 6.26. As a result, a higher notch angle makes higher asymmetry in the high toughness region (low stiffness region) as shown in Figure 6.28.

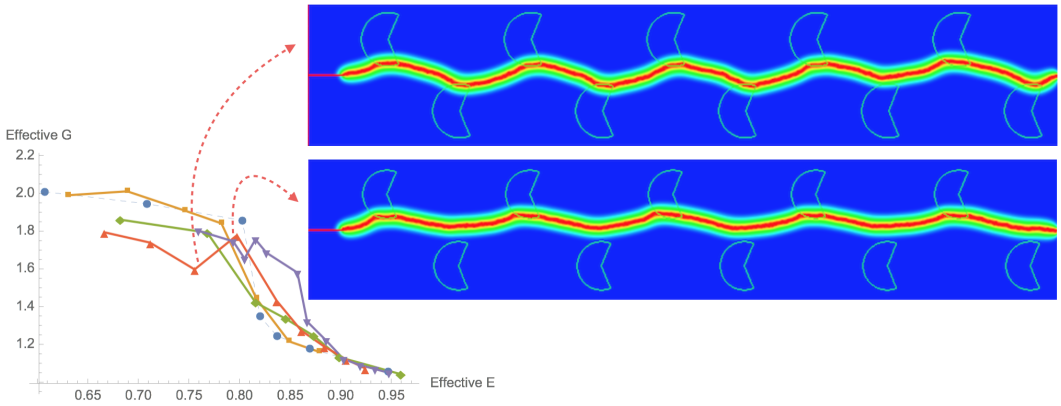

Figure 6.27: Right-facing pacman inclusion with different notch angle

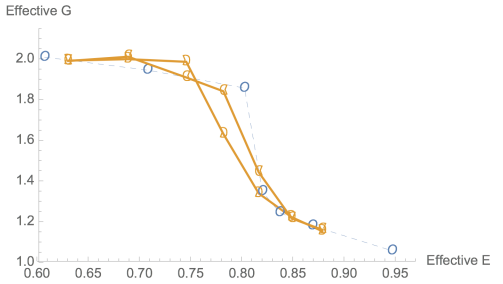

(a) 45 degree

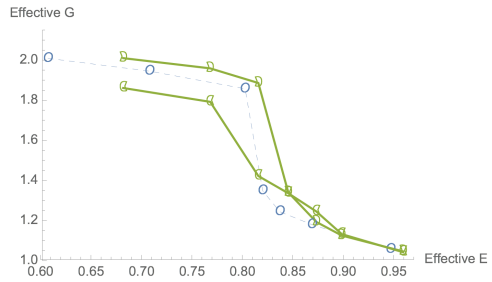

(b) 90 degree

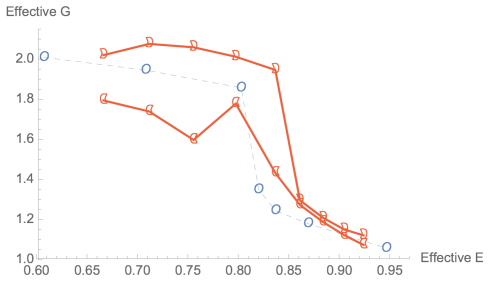

(c) 135 degree

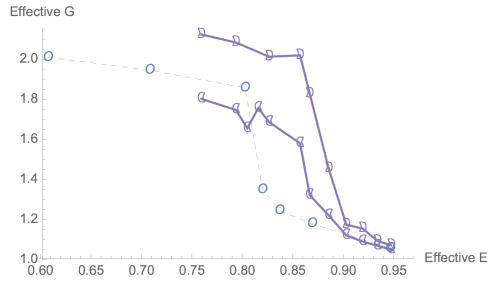

(d) 180 degree

Figure 6.28: Asymmetric toughness for pacman inclusion with different angles

Chapter 7

EXPERIMENTAL STUDIES

[1] C.-J. Hsueh, G. Ravichandran, and K. Bhattacharya. "Investigating the Effective Fracture Toughness of Heterogeneous Materials". In: *Fracture, Fatigue, Failure and Damage Evolution, Volume 8*. Springer, 2017, pp. 15–20. DOI: 10.1007/978-3-319-42195-7_3. URL: http://link.springer.com/chapter/10.1007/978-3-319-42195-7_3.

[2] C.-J. Hsueh, G. Ravichandran, and K. Bhattacharya. "Measuring the Effective Fracture Toughness of Heterogeneous Materials". In: *Fracture, Fatigue, Failure and Damage Evolution, Volume 8*. Springer, 2016, pp. 151–155. DOI: 10.1007/978-3-319-21611-9_19. URL: http://link.springer.com/chapter/10.1007/978-3-319-21611-9_19.

In this chapter, we develop an experimental configuration that can test general heterogeneous specimens and is inspired by the surfing boundary condition. This experimental configuration ensures a stable macroscopic crack growth in heterogeneous specimens but also allows the crack to propagate in any manner that it chooses at the microscopic scale. In order to measure the driving force on the crack, we use a grid method to perform the full-field non-contact measurement. We then use the J-integral to calculate the driving force on the crack. By using the experimental configuration and the grid method, we measure the effective toughness of heterogeneous specimens.

7.1 Surfing loading device

Inspired by the surfing boundary condition, we developed the experimental configuration shown in Figure 7.1. The main purpose of this experimental configuration is to have stable macroscopic crack growth in arbitrary heterogeneous specimens. Unlike traditional test methods, which apply loads on a fixed position of the specimen during the entire test, this experimental configuration applies the displacement sequentially to certain points of the specimen. The surfing boundary condition is applied by rollers and rails. We first machine two pieces of aluminum plate with a precise shape as our rail which are shown as part A1 and A4 in Figure

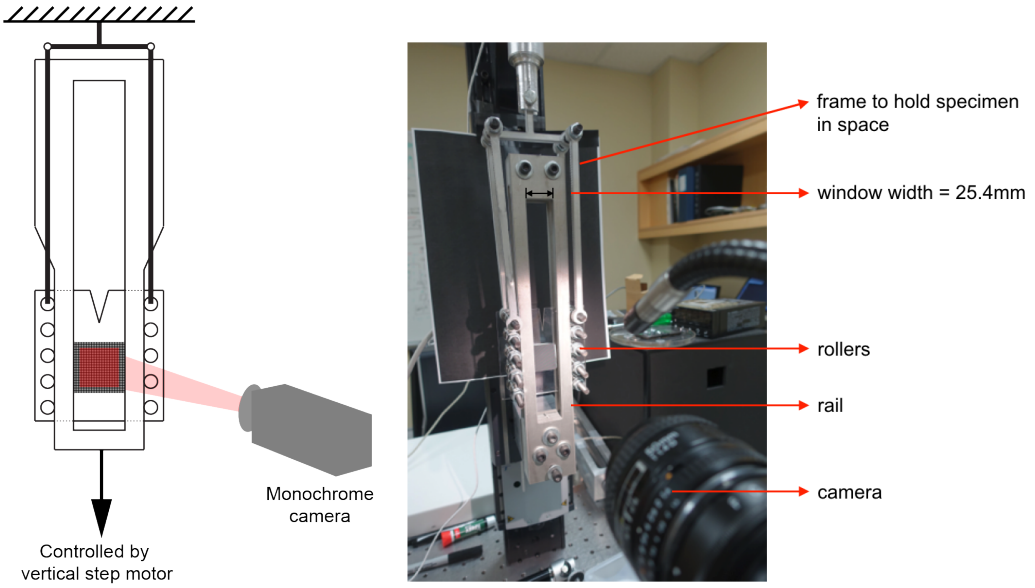

(a) Schematic (b) Actual setup

Figure 7.1: Experimental configuration

7.2(c). Then we assemble the rail with two spacers which are shown as part A2 and A3 in Figure 7.2(c). The thickness of the spacers are choosen to be slightly larger than that of the test specimens. In order to install the specimens onto the experimental configuration, we first put the specimen (part B1 in Figure 7.2(d)) between two aluminum rails. We then insert rods (part C2 in Figure 7.2(d)) on the holes of the specimens and put rollers (part C1 and C3 in Figure 7.2(d)) on the rods. The rollers can slide on the aluminum rail so the width of the rail can control the applied opening displacement. We use an aluminum frame to hold the first row of rods in space. The aluminum rails are connected to a linear stage. As a result, when the linear stage pulls the rail down, the rollers slide along the rail. Therefore, the surfing boundary condition is applied on the specimen experimentally. We can control the applied displacement field by controlling the shape of the rail.

7.2 Measurement of J-integral

In order to measure the driving force on the crack, this experimental configuration can be integrated with non-contact full-field measurement methods such as the digital image correlation (DIC) and the grid method. In our work, we integrate the grid method, which is discussed in detail in Chapter 8, to measure the displacement and strain field. We then use the area

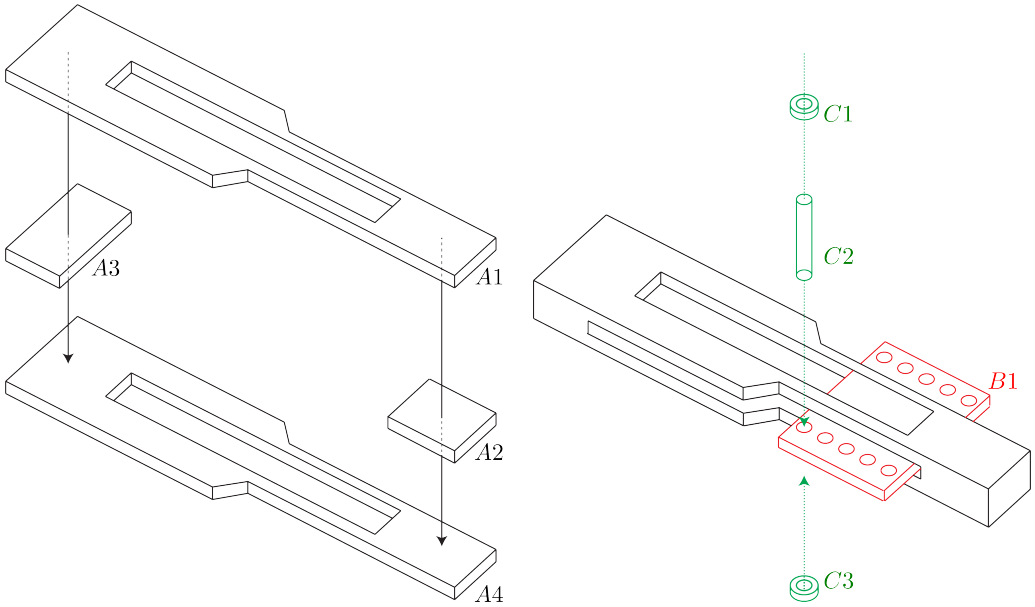

(a) Schematic of assemble the rail (b) Schematic of assemble the specimen

Figure 7.2: Assemble the experimental configuration

J-integral to calculate the macroscopic driving force on the macroscopic crack.

The J-integral is sensitive to the measurement noise [83]. Therefore, we use the area J-integral instead of the traditional line J-integral to involve more data points. The area J-integral can be derived from the traditional line J-integral easily. Suppose we have a line J-integral

$$J = \int_{\Gamma} (W\delta_{ij} - u_{k,i}\sigma_{kj})t_i n_j ds. \tag{7.1}$$

Introduce another contour Γ' which is inside the original contour. Then define a weight function q, which is 0 on the inner contour Γ', 1 on the outer contour Γ, and continuous in between the contours. Therefore,

$$J = \int_{\Gamma} (W\delta_{ij} - u_{k,i}\sigma_{kj})t_i n_j q ds - \int_{\Gamma'} (W\delta_{ij} - u_{k,i}\sigma_{kj})t_i n_j q ds. \tag{7.2}$$

By using the divergence theorem, the equation above becomes

$$J = \int_{A(\Gamma \cup \Gamma')} (W\delta_{ij} - u_{k,i}\sigma_{kj})_{,j} t_i q + (W\delta_{ij} - u_{k,i}\sigma_{kj})t_i q_{,j} dA. \tag{7.3}$$

The first term in the equation above can be represented as

$$(W\delta_{ij} - u_{k,i}\sigma_{kj})_{,j} = \left(\frac{\partial W}{\partial x_i}\right) - u_{k,ij}\sigma_{kj} - u_{k,i}\sigma_{kj,j} \tag{7.4}$$

$$= \frac{\partial W}{\partial u_{p,q}} u_{p,qi} - u_{k,ij}\sigma_{kj} - u_{k,i}\sigma_{kj,j} \tag{7.5}$$

$$= \sigma_{pq}u_{p,qi} - u_{k,ji}\sigma_{kj} - u_{k,i}\sigma_{kj,j} = -u_{k,i}\sigma_{kj,j}. \tag{7.6}$$

Therefore, the equation above becomes

$$J = \int_{A(\Gamma\cup\Gamma')} (-u_{k,i}\sigma_{kj,j})t_i q + (W\delta_{ij} - u_{k,i}\sigma_{kj})t_i q_{,j} dA. \tag{7.7}$$

In the case of quasi-static, we have $\nabla \cdot \sigma = 0$. Thus, the J-integral becomes

$$J = -\int_{A(\Gamma\cup\Gamma')} (u_{k,i}\sigma_{kj} - W\delta_{ij})t_i q_{,j} dA. \tag{7.8}$$

7.3 Preliminary results of fracture tests

In this section, we describe fracture tests on 3D printed specimens using the surfing loading device. The benefit of the 3D printing technique is that we have the ability to control every voxel of the specimens. Thus, we can create any structure we want and test it. We used Ember, a 3D printer produced by Autodesk, to print our specimens. The dimension of the specimens is shown in Figure 7.3. The medium gray region in the center is the test region, which has thickness 1.5mm. The small light gray circular regions in the test region indicate the heterogeneity. The heterogeneity is 0.3mm thick (20% of test region thickness). The dark gray regions at the side are the reinforced regions which is 3mm thick. The large white circular region in the reinforced regions are the circular holes that are used to assemble rods and rollers to mate with the loading device.

The microstructure of the heterogeneity is also shown in Figure 7.3. The heterogeneities are arranged in a square microstructure. However, we have to restrict the region of heterogeneity because we need a homogeneous region surrounding it to measure the J-integral.

Homogeneous specimen

We first test the homogeneous specimen (there is no heterogeneity in the test region) on the surfing loading device. We use the area J-integral to measure the driving force on the crack and use Irwin's formula $G = \frac{K_I^2}{E}$ to

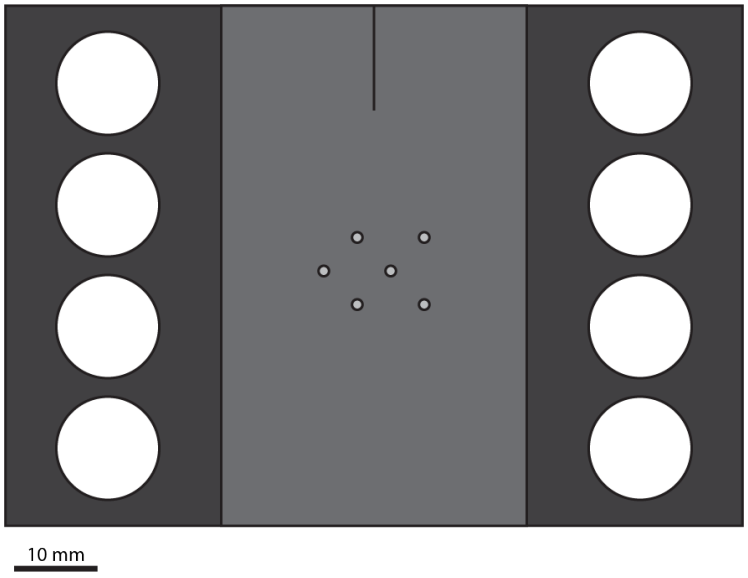

Figure 7.3: 3D printed heterogeneous specimens for fracture test

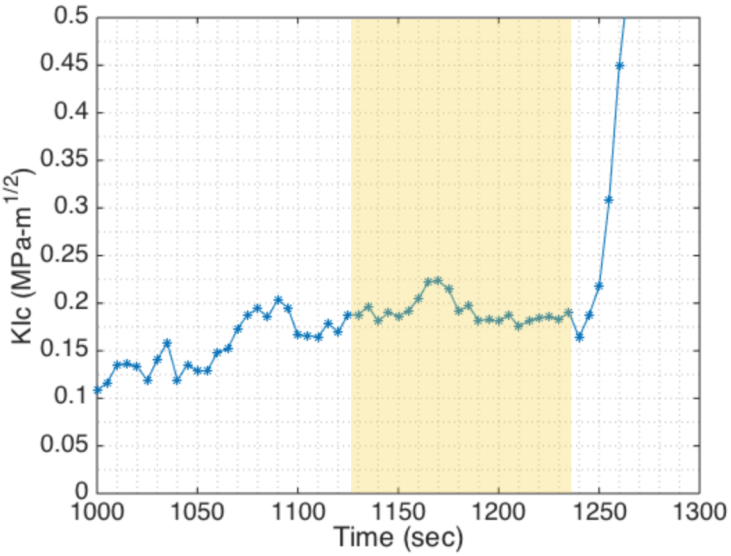

Figure 7.4: The stress intensity factor of the homogeneous specimen

calculate the stress intensity factor. The measured stress intensity factor is shown in Figure 7.4.

We can see that in Figure 7.4, the stress intensity is nearly a constant in the yellow shaded region. We can take the time-average on the J-integral and get the (averaged) J-integral is 49.87 N/m and the corresponding stress intensity factor 0.192 MPa$\sqrt{\text{m}}$.

In the last part of Figure 7.4, the crack tip goes out of the integration region

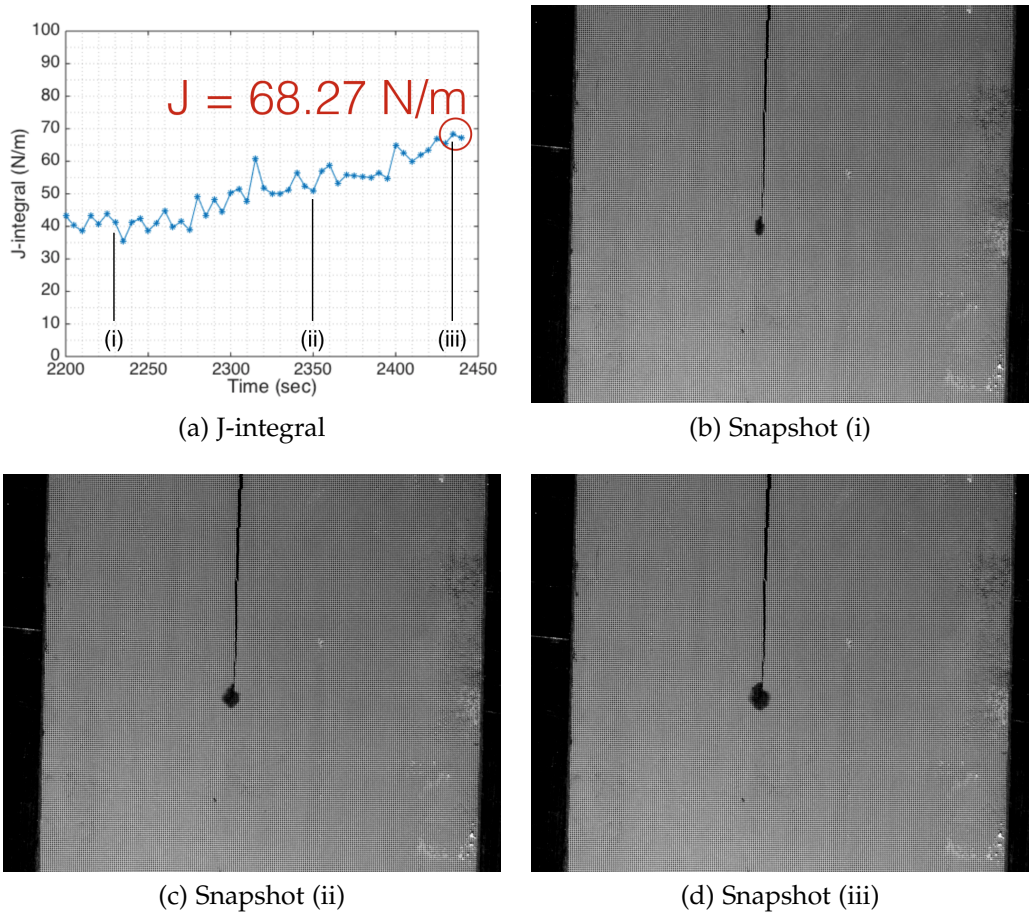

(a) J-integral

(b) Snapshot (i)

(c) Snapshot (ii)

(d) Snapshot (iii)

Figure 7.5: The J-integral of the weak heterogeneity specimen

and the J-integral is not meaningful.

Heterogeneous specimens

We also tested the heterogeneous specimens as shown in Figure 7.3. We have used two different sizes of the heterogeneous inclusions, radius 0.5*mm* (weak heterogeneity) and 1.25*mm* (strong heterogeneity).

We first tested the weak heterogeneous specimen which has heterogeneous inclusions with radius 0.5*mm*. The J-integral when the crack is trapped (in a heterogeneous inclusion) is shown in Figure 7.5. The results show that the J-integral is increasing when the crack is trapped in the inclusion. The maximum value J-integral can reach is 68.27N/m, which is significantly higher than the J-integral value we have from the homogeneous material (49.87 N/m). Thus, the heterogeneity does increase the effective toughness.

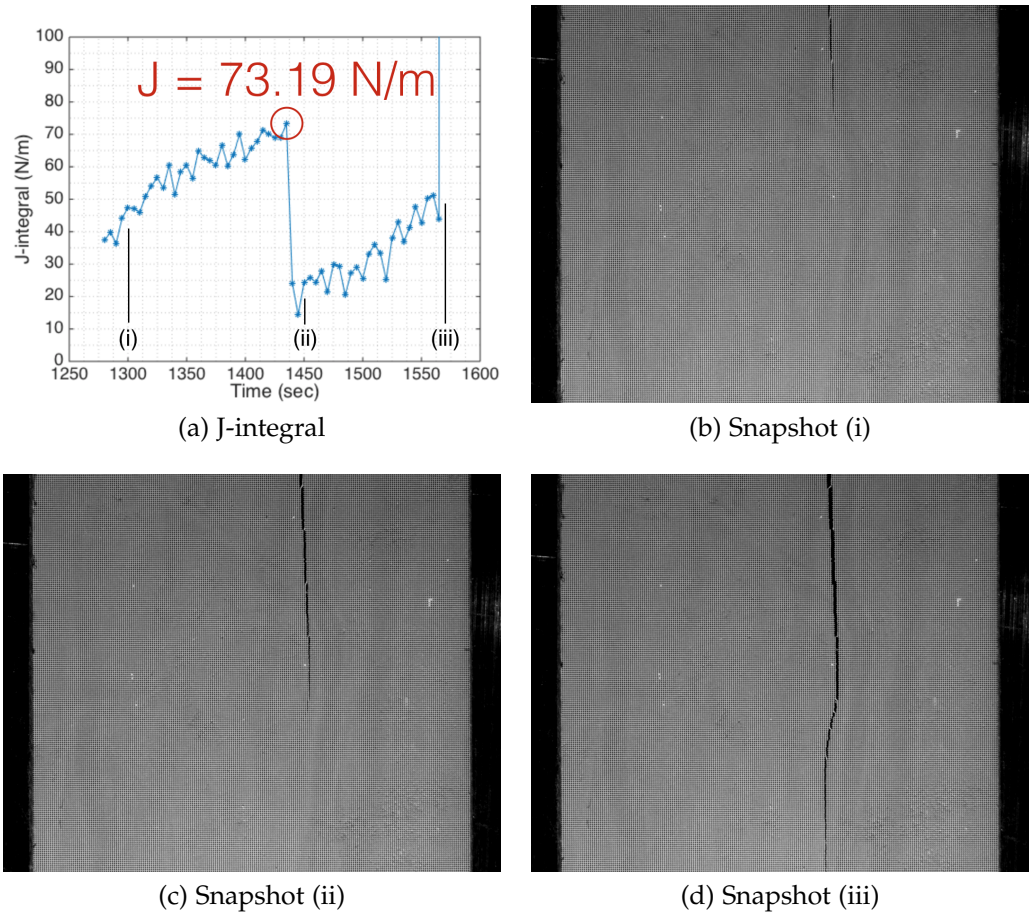

(a) J-integral

(b) Snapshot (i)

(c) Snapshot (ii)

(d) Snapshot (iii)

Figure 7.6: The J-integral of the strong heterogeneity specimen

We also tested the strong heterogeneous specimen, which has heterogeneous inclusions with radius $1.25mm$. The J-integral when the crack is trapped in a heterogeneous inclusion is shown in Figure 7.6. We can see that the J-integral is increasing when the crack is trapped, which is similar to the previous case. Moreover, the peak value 73.19N/m is higher than the previous case.

In conclusion, we have shown that the heterogeneity can increase the effective toughness. Furthermore, the results show that the toughening mechanism is controlled by the microstructure.

Chapter 8

NOVEL GRID METHOD

[1] C.-J. Hsueh, N. Brodnik, and M. T. Johnson. "A novel method to perform the grid method in order to reduce the measurement bias". In: *To be submitted* (2017).

Non-contact full-field measurement methods are extremely useful in experimental mechanics. Interferometric technique and digital image correlation are two of the most widely used non-contact full-field measurement techniques. However, these methods have their own weakness. Although interferometric techniques can provide high measurement resolution, they require complex and accurate experimental configurations that greatly increase the difficulty of implementation. In contrast, digital image correlation is easy to implement but it has a relativity low measurement resolution, especially for small deformation and non-uniform deformation [68]. Therefore, the grid method, which is a compromise between the better measurement resolution of interferometry and the ease of implementation of DIC, has been developed [35]. The idea of the grid method is similar to DIC, where deformation fields are obtained by comparing images before and after deformation. However, unlike DIC, the grid method uses regular patterns instead of random patterns. By extracting the phase distributions of the fringes of these regular patterns, a deformation field can be obtained.

8.1 The grid method

A common method of producing the grid pattern on a specimen is by transferring the pattern printed on a photomask onto the specimen [72]. One can easily obtain a photo mask with a designed pattern with minimum feature size as small as 10 microns. In order to properly transfer the pattern on the specimen, alcohol is used to remove the grease and dirt first. Then epoxy is applied on the specimen and the photomask is put on the epoxy. The photomask is slightly pressed so the bubbles and extra epoxy can be removed. Then the specimen is placed in an oven under slight pressure for 24 hours to cure the epoxy. After the epoxy cures, the photomask is

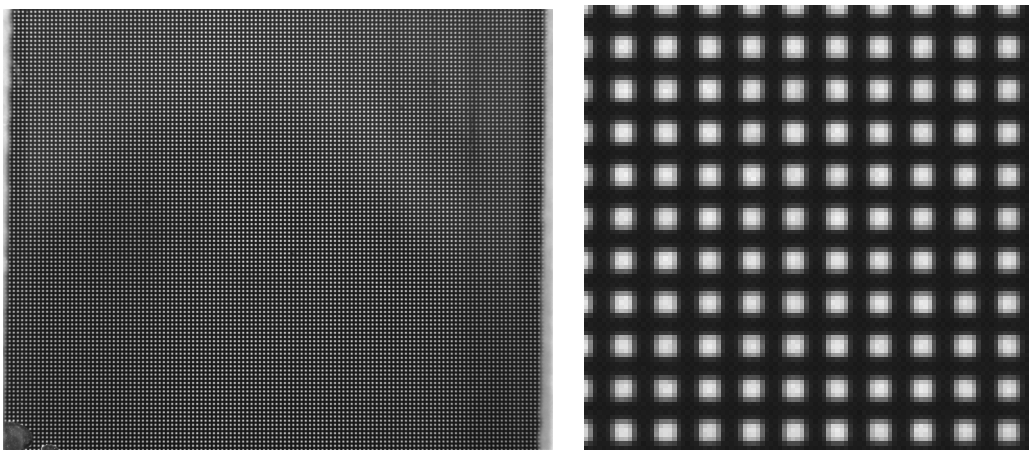

(a) Traditional grids (b) Traditional grids (zoom in)

Figure 8.1: Traditional grid patterns

carefully peeled off and the pattern on the photomask is retained on the specimen. Figure 8.1 is the transferred pattern of the photomask on a specimen.

After producing the grid pattern on the specimen, one can use the images to extract the deformation field. Suppose the camera is aligned properly so the pattern is periodic along the pixel direction. The gray value $g(\vec{x})$ of the image is

$$g(\vec{x}) = \frac{I_0}{2}\left[2 + \gamma \cdot F\left(\frac{2\pi}{p}\vec{x} + \vec{\phi}(\vec{x})\right)\right], \tag{8.1}$$

where I_0 is the average illumination of the system, $0 \le \gamma \le 1$ is the contrast of the pattern, $F : \mathbb{R}^2 \to \mathbb{R}$ is a normalized 2π-periodic function with average 0 and amplitude 2, p is the period of the pattern, and $\vec{\phi} = [\phi_1, \phi_2]^T$ is the phase modulation map. For a given gray scale grid pattern image, a windowed-Fourier-transform is used with chosen window function w to extract the components of the phase modulation map as follows:

$$\phi_1(\vec{x}) = \tan^{-1}\left(\frac{Im(\hat{g}(\vec{z}, \vec{f_1}))}{Re(\hat{g}(\vec{z}, \vec{f_1}))}\right) \tag{8.2}$$

$$\phi_2(\vec{x}) = \tan^{-1}\left(\frac{Im(\hat{g}(\vec{z}, \vec{f_2}))}{Re(\hat{g}(\vec{z}, \vec{f_2}))}\right), \tag{8.3}$$

where $\vec{f_1} = [\frac{1}{p}, 0]^T$, $\vec{f_2} = [0, \frac{1}{p}]^T$, and

$$\hat{g}(\vec{z}, \vec{f}) := \int_{\mathbb{R}^2} g(\vec{x}) w(\vec{z} - \vec{x}) e^{-i2\pi(\vec{f}\cdot\vec{x})} d\vec{x}. \tag{8.4}$$

In this study, the Gaussian function $w(\vec{x}) = \frac{1}{2\pi\sigma^2} e^{-\frac{\vec{x}\cdot\vec{x}}{2\sigma^2}}$ is used with $\sigma = p$ as the window function.

Suppose we have a reference image (with gray scale g_r) and a deformed image (with gray scale g_d). The relationship between these two images is

$$g_r\left(\vec{x}\right) = g_d\left(\vec{x} + \vec{u}(\vec{x})\right). \tag{8.5}$$

Substitute equation (8.1) into the equation above to obtain

$$\frac{I_0}{2}\left[2 + \gamma \cdot F\left(\frac{2\pi}{p}\left(\vec{x} + \vec{u}\left(\vec{x}\right)\right) + \vec{\phi}_d\left(\vec{x} + \vec{u}\left(\vec{x}\right)\right)\right)\right] = \frac{I_0}{2}\left[2 + \gamma \cdot F\left(\frac{2\pi}{p}\vec{x} + \vec{\phi}_r\left(\vec{x}\right)\right)\right], \tag{8.6}$$

where $\vec{\phi}_r$ and $\vec{\phi}_d$ are the phase modulations map of reference and deformed images respectively. By comparing the phase modulations, we have

$$\frac{2\pi}{p}\vec{u}\left(\vec{x}\right) + \vec{\phi}_d\left(\vec{x} + \vec{u}\left(\vec{x}\right)\right) = \vec{\phi}_r\left(\vec{x}\right). \tag{8.7}$$

Thus, the displacement field $\vec{u}$ can be calculated by using

$$\vec{u}(\vec{x}) = -\frac{p}{2\pi}\left(\vec{\phi}_d\left(\vec{x} + \vec{u}(\vec{x})\right) - \vec{\phi}_r(\vec{x})\right). \tag{8.8}$$

Equation (8.9) is a non-linear equation in $\vec{u}$. One can use iterative approach to solve the equation (8.9):

$$\vec{u}_{n+1}(\vec{x}) = -\frac{p}{2\pi}\left(\vec{\phi}_d\left(\vec{x} + \vec{u}_n(\vec{x})\right) - \vec{\phi}_r(\vec{x})\right). \tag{8.9}$$

Finally, the strain field is determined by taking the derivative of the displacement field numerically.

8.2 Novel implementation of grid method

Although using the epoxy to transfer the grid pattern onto a specimen is a common technique, it presents serious concern when the toughness and stiffness of the specimen are low. The epoxy layer can contribute extra stiffness and toughness and bias the measurement. Therefore, we propose a novel method to produce the pattern on the specimen without using an epoxy layer. This novel method is developed in collaboration with Neal Brodnik and Matthew Johnson.

We first use the traditional semiconductor photolithography techniques to create a template for a textured photopolymer grid pattern. A silicon wafer

is coated with SU-8 photoresist to a thickness of about 70 microns and then exposed through a grid-patterned mask and developed. The result of this is a silicon wafer which has a uniform pattern of SU-8 pillars that are 70 microns tall and have spacing corresponding to the pitch of the grid. This resist-patterned wafer is then coated with Sylgard 184 liquid silicone and placed under rough vacuum for 30 minutes to allow for proper infiltration and degassing. Once infiltration is sufficient such that the silicone is cleanly wetted to the SU-8 photoresist and is optically clear across the entire wafer, the wafer is cured for 2 hours at 70 degrees Celsius. Once fully cured, the silicone is separated from the resist-coated wafer to produce a silicone template mold which has uniform square channels in it that are 70 microns deep and have a pitch of 100 microns.

To make a grid pattern as shown in Figure 8.2 on a sample, a layer of liquid photopolymer is deposited onto the sample of interest using a pipette. Once this photpolymer layer is deposited, the silicone grid template is placed on it and allowed to settle under its own weight, after which excess photopolymer is removed. The sample with the silicone template still resting on it is then placed under rough vacuum to remove all air trapped beneath the template. Once all air has been removed, the sample is placed under UV light for 20 minutes to fully cure the liquid PR 48 polymer into the shape of the silicone template. Because the polymer is physically constrained by the shape of the template, overexposure and fugitive polymerization are not of concern. However, if samples are very thin, they should be inverted intermittently during the UV exposure period to prevent warping of the sample. Once polymerized, the photopolymer preferentially adheres to the polymer specimen over the silicone template, so the template can be easily removed for repeated use. Once separated, both the sample and template are cleaned with isopropanol.

At this point, the specimen has an array of pillars on it which form a grid pattern, but this grid pattern is only present as surface morphology and has little optical contrast. To add optical contrast, the valleys between these pillars are filled in with opaque powder that is optically differentiable from the grid material. In the case of this study, the photopolymer used is translucent, so the powder chosen to fill in the valleys is alumina with a median particle size of 350 nm. The powder is ground in a mortar and

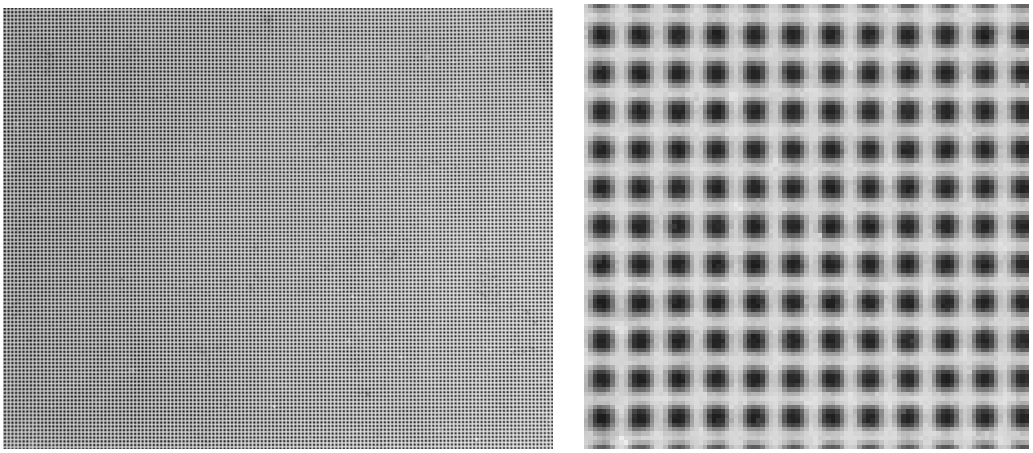

(a) Novel grids (b) Novel grids (zoom in)

Figure 8.2: Novel grid patterns

pestle to break up any aggregated particles and is then spread over the patterned sample face using a flat edge, taking care not to damage the array of pillars, as this will disrupt the grid regularity. Once the powder is spread, this same flat edge is used to remove any excess powder, leaving a grid pattern of white alumina on the sample. To achieve good contrast, the sample is imaged against a black background during testing.

8.3 Test of the novel grids

Synthetic test

To assess the quality of the grids produced in this study (grids pattern shown in Figure 8.2), synthetic tests were performed to compare them to grids produced using traditional lithography and epoxy mounting methods (grid pattern shown in Figure 8.1) as well as to perfect grids fabricated digitally (grid pattern shown in Figure 8.3). The traditional lithography photo mask is produced at the company Laser Technologie (address: 1 rue Jean Rostand, ZI les Bruyères, 78190 Trappes, France) and Loctite® Epoxy Marine is used to transfer the pattern on the photomask. The perfect grids were produced using the gray value distribution

$$s(x_1, x_2) = \frac{I_0}{2} \times \left[2 + \gamma \times \left(\sin \frac{2\pi x_1}{p} + \sin \frac{2\pi x_2}{p} \right) \right]. \tag{8.10}$$

Since the imaging done in this study has a depth of is 8-bits per pixel, $I_0 = 255/2$, $\gamma = 1$, and $p = 10$ and the grid pattern is shown in Figure 8.3.

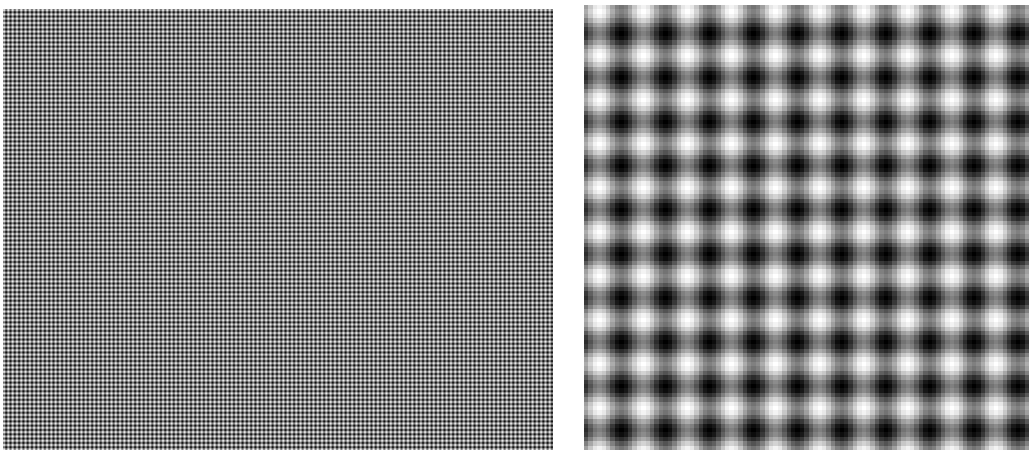

(a) Perfect grids (b) Perfect grids (zoom in)

Figure 8.3: Perfect digital grid patterns

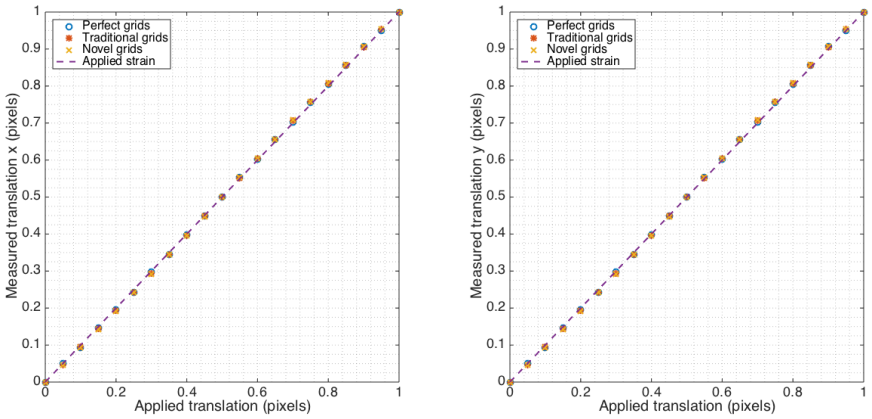

Figure 8.4: Measured translation in synthetic tests

In the synthetic tests, a square region is chosen at the center of the image which contains $N \times N$ pixels over which the applied field and the measured field of different grid patterns are compared. In the following tests, we choose $N = 800$ pixels as our analysis region size.

First, a sub-pixel synthetic translation in both horizontal (x-direction) and vertical (y-direction) directions is applied. Grid method analysis is then performed to calculate the measured translation in both the x and y directions. The average translation from this analysis is then compared to the synthetic applied translation, and the results of this comparison are plotted in Figure 8.4. This figure shows that the measured translation qualitatively match the applied translation reasonably well in the sub-pixel level.

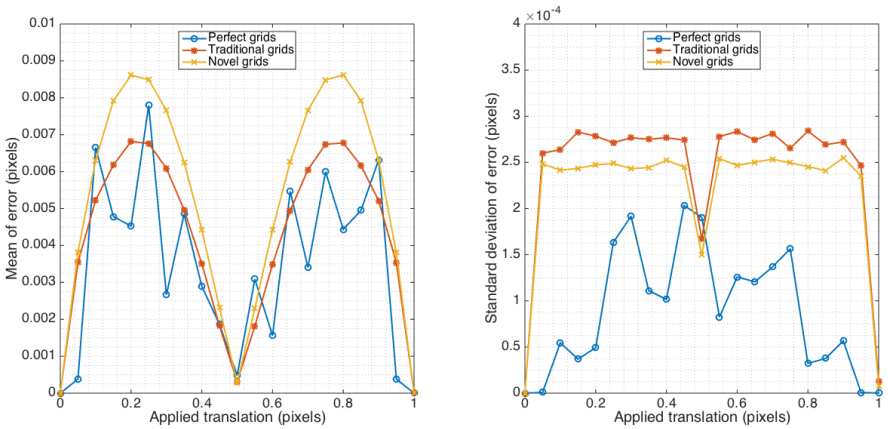

Figure 8.5: Mean and standard deviation of the pixel-wise error in translation synthetic tests

The error in each pixel is defined in the following form:

$$e^u := \frac{1}{2}\left(\left|u_x^{measured} - u_x^{applied}\right| + \left|u_y^{measured} - u_y^{applied}\right|\right). \tag{8.11}$$

The mean and the standard deviations of the errors are then calculated in the region of analysis. The results are plotted in Figure 8.5. The mean and standard deviation of errors are related to measurement accuracy and precision respectively as shown in Figure 8.6. The mean of error (accuracy) indicates how close the measured values are to the reference values (true value). In Figure 8.5, we can see that the mean error (accuracy) is of the same order for all grids. Furthermore, all grids provide high measurement accuracy (mean of error < 0.009 pixel). The standard deviation of error (precision) indicates how close two measurements are. In Figure 8.5, although all grids provide high measurement precision (standard deviation of error < 0.0003 pixel), the perfect grids have much higher measurement precision than the other two grids. This is because the regularity of the perfect grids is perfect. There are no defects in the perfect grids. However, it is inevitable to have defects in real grid patterns.

Synthetic biaxial stretch tests were also performed on all three grid patterns. In these tests, the average normal strain in the analysis region is compared with the synthetic applied translation, the results of which are plotted in Figure 8.7. Similarly to the synthetic translation study, the measured strain also qualitatively matches the applied translation well when

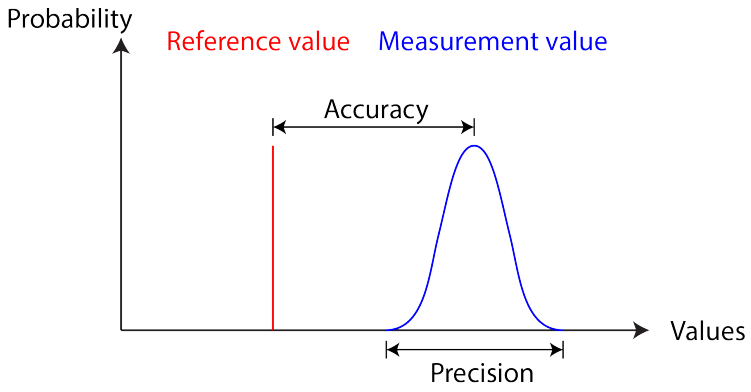

Figure 8.6: Measurement accuracy and precision

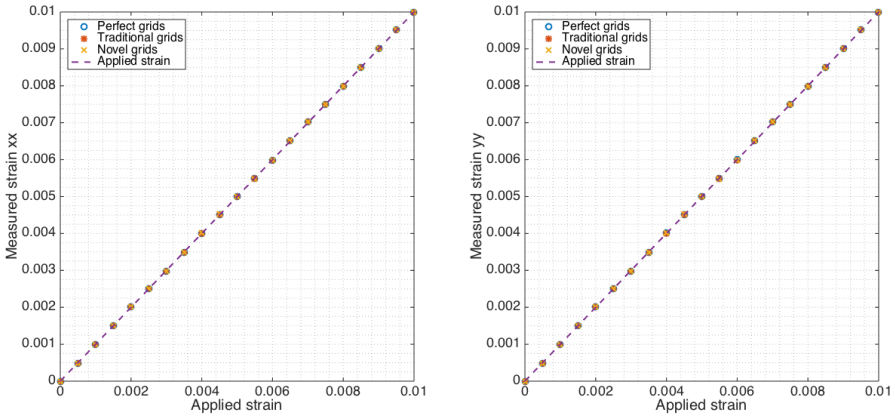

Figure 8.7: Measured strain in synthetic tests

applied strain is smaller than 1%. The error in each pixel is defined as the following.

$$e^{\varepsilon} := \frac{1}{2}\left(\left|\varepsilon_{xx}^{measured} - \varepsilon_{xx}^{applied}\right| + \left|\varepsilon_{yy}^{measured} - \varepsilon_{yy}^{applied}\right|\right). \tag{8.12}$$

The mean and the standard deviation of the errors in the analysis region for the biaxial stretch tests are plotted in Figure 8.8. In this figure, we can see that the novel grids have slightly larger mean of error than other two grids, which means the measurement accuracy is slightly lower.

The result of the synthetic tests indicate that the mean error in all of the grid patterns are within the same order of magnitude. However, the perfect grid has a much smaller standard deviation of the error compared to both the grids made directly with lithography or the grids made using a silicone template and powder filling. This is expected because the regular-

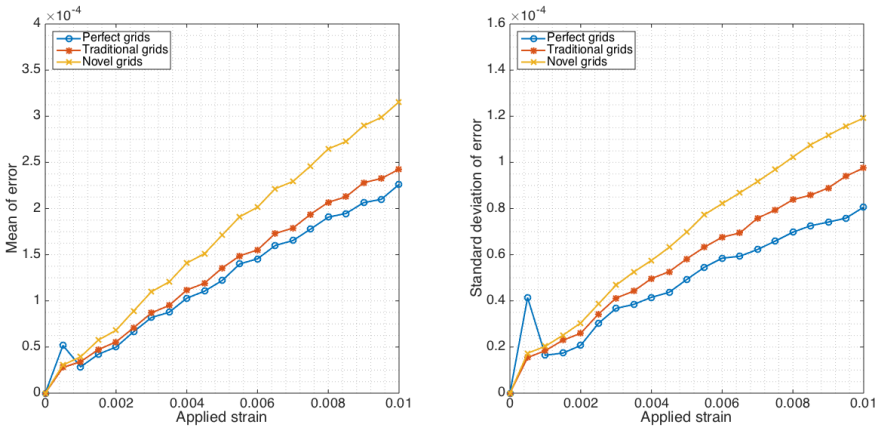

Figure 8.8: Mean and standard deviation of the pixel-wise error in biaxial strain synthetic tests

ity of the perfect grids is completely unperturbed. Additionally, all of the synthetic tests indicate that the error in the novel grids is slightly higher than the error in the traditional grids. The reason for this is because the novel grids are produced from the photomask so the defects in the novel grids are slightly more than the defects in the photo mask (but almost the same). However, without using an entire epoxy layer, the novel grids can drastically reduce the bias on the actual experiment.

Uniaxial tensile test

Uniaxial tensile testing was performed on laser-cut PMMA dog bone specimens. The cross-section of the test region of the specimen is 12.7mm x 3.125mm. We applied force up to 350 N to the specimen and used the grid method to determine the strain response. The stress-strain curve is plotted in Figure 8.9. As we expected, we have a linear relationship between the stress and strain because PMMA is a brittle material. We also used the least square method to calculate the Young's modulus. The Young's modulus calculated by the uniaxial tensitle test is 2.62 GPa, which is in the region of published values.

Plate-hole experiment

The grids produced by the novel method were also used to perform a full-field measurement on a traditional plate-hole experiment. Similar to the uniaxial tensile tests, the specimens were made from laser-cut PMMA with dimensions of 76.2 mm (width) x 177.8 mm (height) x 3.175 mm (thickness).

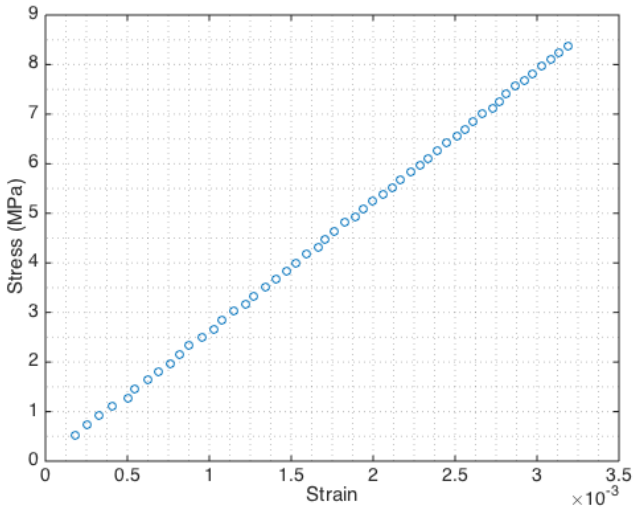

Figure 8.9: Stress-strain curve of PMMA specimen

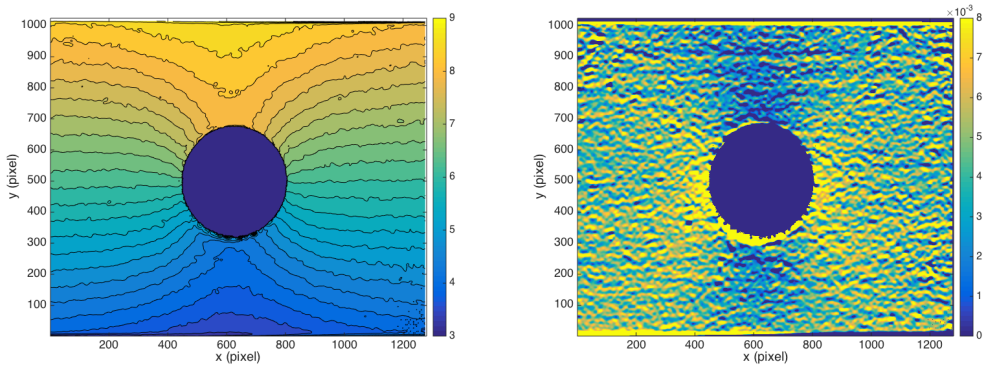

(a) displacement u_2 (b) normal strain ε_{22}

Figure 8.10: Displacement and strain field in the plate-hole experiment

A laser cutter was also used to make a circular hole with radius 6.35 mm. A 2200 N uniaxial tensile force was applied at the end of the specimen and the full deformation field near the hole was measured. The displacement field u_2 is shown in Figure 8.10(a). Finite differences then used to calculate the normal strain ε_{22} and this is shown in 8.10(b). In this figure, we can see the displacement field is well captured macroscopically. However, there is noise in the displacement field, especially near the hole. As a result, the strain field is much noiser because it is the derivative of the displacement field. The result is acceptable because the strain field is very small (in the order of 10^{-3}).

8.4 Discussion

In this chapter, we proposed a novel implementation method for the grid method which is a compensation between DIC (easy to implement) and the interferometric technique (high measurement resolution). The advantage of this novel implementation is that there is no need for an epoxy layer to create the grid pattern. Therefore, the bias of the epoxy layer is eliminated. We test the novel grids synthetically and the error of the novel grids is slightly larger than the traditional grids. We then test the novel grids with a uniaxial tensile test and the measured elastic modulus is in the published values. We also test the novel grids with a plate-hole test, which shows that the novel grids are able to characterize the inhomogeneous deformation field well.

Suppose we want to measure the deformation field on brittle and weak specimens. The DIC does not have very high measurement resolution, so it suffers from the small deformation field if the specimens are brittle. On the other hand, the traditional grid method biased the measurement easily by the epoxy layer if the specimens are weak. The novel implementation we proposed can fill this gap and be useful for brittle and weak specimens.

Chapter 9

A MODEL PROBLEM OF FRACTURE MECHANICS: THE PEELING PROBLEM

[1] C.-J. Hsueh and K. Bhattacharya. "Optimizing microstructure for toughness: The model problem of peeling". In: *To be submitted* (2017).

We consider the problem of peeling an adhesive thin film from a substrate. This peeling problem as well as closely related problems arise in various applications in engineering and biology. The peeling problem is also a model problem in fracture mechanics. This problem is easier than the general fracture mechanics problem because the peel front (crack front) is confined to a plane. Furthermore, the analysis of stress distribution is easier in the thin domain. In this chapter, we study peeling a thin film from a rigid substrate with heterogeneous adhesive distribution. We seek to understand the distributions of adhesive strength that optimize aspects of the effective adhesive strength. We do so both analytically and computationally using topology optimization.

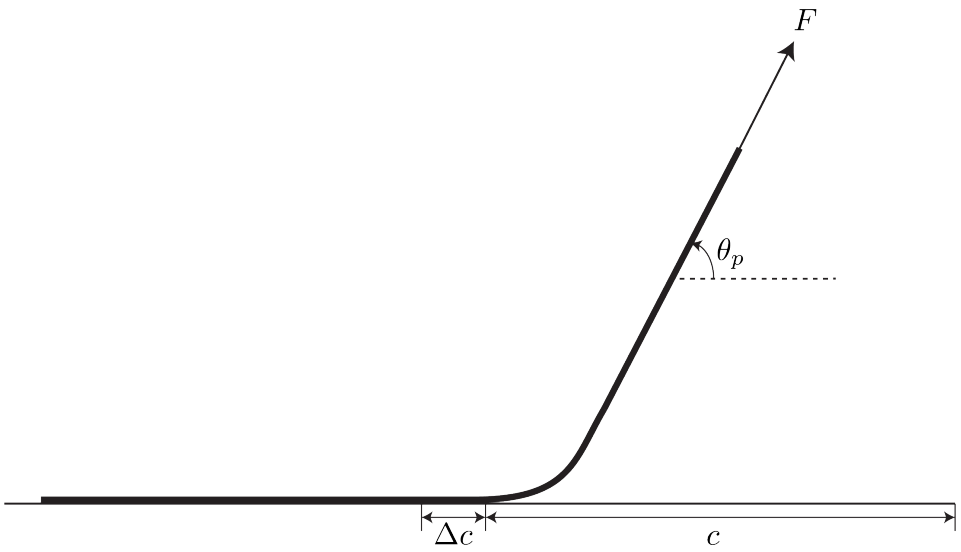

Figure 9.1: The 1d peeling model

9.1 Background

The study of peeling can be traced back to Rivlin [75]. This provides a simple one-dimension model which connects the adhesive strength with the force required to peel off an adhesive inextensive thin film from a rigid substrate. Consider a thin film is peeled at a fixed angle as in Figure 9.1. When the incremental length of the film Δc to be peeled, the point of the peel force F move by $\Delta c\left(1-\cos\theta_p\right)$ along the peeling direction. By the energy balance, the work done by the peeling force is equal to the change of the surface energy.

$$F\Delta c\left(1-\cos\theta_p\right)=\varphi\Delta c \quad \Longrightarrow \quad F=\frac{\varphi}{1-\cos\theta_p}, \tag{9.1}$$

where φ is the adhesive strength. This model shows that for a fixed angle, the required peeing force for an inextensive thin film is linearly proportional to the adhesive strength.

In the following decades, this has been followed by various researchers. Kaelble studied micro-fracture mechanisms in the process [44–46]. Gent and Hamed studied the peeling of an adhesive polymer film from a surface either tangentially (180^o) or perpendicularly (90^o) [31–33]. Kendall studied peeling of elastic (and extensible) films and the development of interfacial dislocations [47–49].

More recently, work has focused on heterogeneous systems. Ghatak et al. have studied the peeling of a flexible plate and found that the peeling force is enhanced by a patterned elastomeric substrate [34]. Chung and Chaudhury have similar results and attributed the enhancement to the crack nucleation at heterogeneities [14]. Ramrus and Berg studied the adhesion of random patterns [73]. Chan et al. focused on adhesive interfaces on periodic patterns [13]. In addition to two-dimension patterns, Greiner et al. investigated the toughening by 3D structures such as pillars and other features on the substrate [36]. In the past few years, Shuman Xia et al. studied the effective adhesion strength of thin films on flat substrates with heterogeneous adhesion strength [87, 88]. They attached a polydimethylsiloxane (PDMS) thin film on a transparent surface with an ink pattern. The adhesion strength of PDMS is different on the ink-coated surface versus the uncoated transparency surface, i.e., the adhesion strength distribution is heterogeneous. They peeled the PDMS thin film with constant velocity

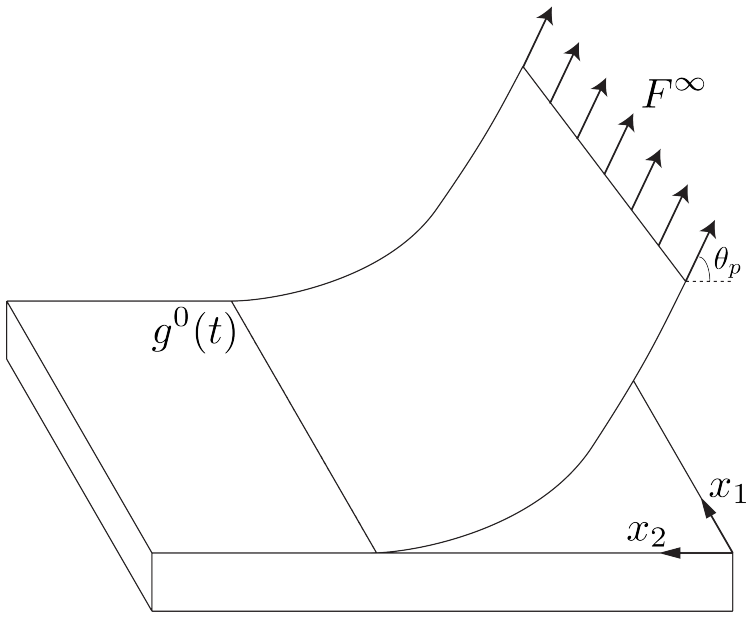

Figure 9.2: The peeling problem

and at constant angle. They have observed that the peeling force oscillates and defined the effective adhesion strength of the pattern to be the peak of the peeling force. If the applied force is smaller than the effective adhesion strength, the thin film cannot be peeled off. They found that the effective strength depends on the pattern. Furthermore, they found out that the effective adhesion strength can be asymmetric if the pattern is asymmetric, i.e., the applied force to peel the thin film off in one direction is different than the opposite direction. This study opened the possibility that one can design the desired effective adhesion by controlling the adhesion distribution. The current work is motivated by understanding the link between pattern and effective adhesion, specifically the question of designing patterns for desired effective adhesion.

As the film is peeled from a substrate with heterogeneous adhesion, the peel front that separates the adhered and separated regions is not straight. So the mathematical problem is a free boundary problem. The analysis of free boundary problems in a heterogeneous medium is the subject of recent interest [16, 18] and we use their results in our analysis.

9.2 Model of the peeling problem

Consider the peeling problem as shown in Figure 9.2. Assume that the thin film is inextensible and elastic homogeneous. If the adhesion distribution

is uniform, the peel front position $g^0(t)$ is a straight line and the required force to peel it off can be calculated by Rivlin's model (9.1).

If the adhesion strength is not uniform but some function $\varphi = \varphi(x_1, x_2)$, the peel front would be curved as shown in Figure 9.3. Assuming that the curved peel front $x_2 = g(x_1, t)$ is close to the straight peel front $x_2 = g^0(t)$, Xia et al. obtained the governing equation of the curved peel front [87]:

$$\frac{\partial g}{\partial t}(x_1, t) = \alpha' \int_{-\infty}^{\infty} \frac{g(\xi, t) - g(x_1, t)}{|\xi - x_1|^2} d\xi - \varphi(x_1, g(x_1, t)) + F \tag{9.2}$$

$$= -\alpha(-\Delta)^{\frac{1}{2}} g(x_1, t) - \varphi(x_1, g(x_1, t)) + F, \tag{9.3}$$

where α', α are positive constants depending on the bending modulus of the thin film, $\varphi(x_1, x_2)$ is the adhesive strength distribution, and $F = F^\infty(1 - \cos\theta_p)$ is the macroscopic driving force.

In this governing equation, the velocity of the peel front is determined by the competition among three terms. The first term, the half Laplacian term, is the stiffness of the peel front. If the peel front is curved, it will introduce complex bending in the thin film and increase the bending energy. Therefore, the half-Laplacian term would like to straighten the peel front. The second term is the adhesion strength distribution evaluated at the peel front position. Since it has to be evaluated at the peel front position, the shape and position of the peel front can affect the peel front propagation. This non-linear term makes the peeling problem interesting. The last term is the driving force on the peel front. Suppose the peeling angle is fixed: then the driving force is linearly proportion to the far-field peeling force F^∞.

This governing equation also arises in many physical phenomena such as ferroelectric and ferromagnetic domain walls, dislocations, etc [18].

Since we are interested in the overall behavior of the front at length-scales that are much larger compared to the variations of the adhesive strength φ, we specialize to the situation where φ is periodic. Without loss of generality, we assume (by rescaling if necessary) that the period is 1 in both direction. Then it is convenient to take Fourier transform with respect to x_1 are rewrite the equation as

$$\frac{\partial \hat{g}}{\partial t}(k, t) = -\alpha|k|\hat{g}(k, t) - \widehat{\varphi(x_1, g)}(k, t) + \hat{F}, \tag{9.4}$$

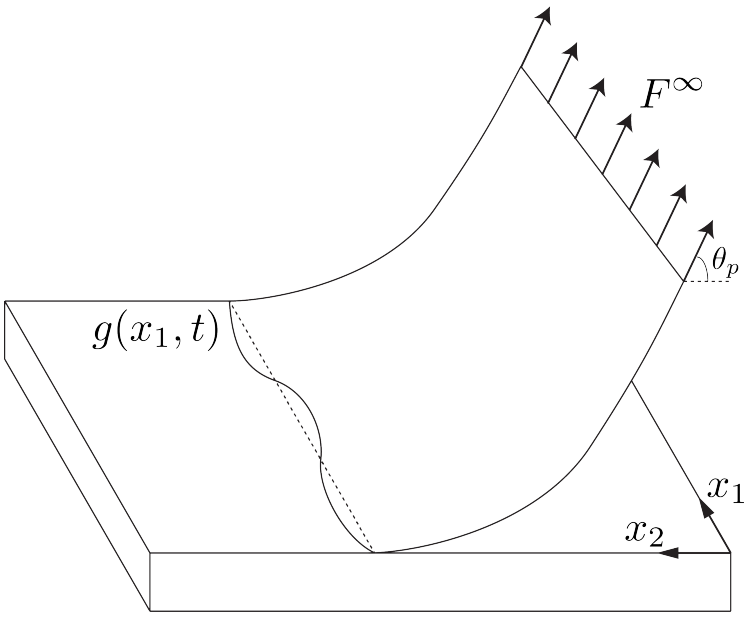

Figure 9.3: Curved peel front

where the superimposed hat denotes the Fourier transform.

When the applied force is small, equation (9.3) has stationary solutions. It means that the applied force is insufficient to peel the film off and the peel front will be pinned. Thus, the critical force F^* is defined as the smallest applied force necessary to peel the front over distances large compared to the period of φ, or the largest value of F for which we can have a stationary peel front:

$$F^* := \max_F \left\{ F \;\middle|\; 0 = -\alpha\,(-\Delta)^{\frac{1}{2}}\, g - \varphi(x, g) + F \text{ has a solution} \right\}. \tag{9.5}$$

Dondl and Bhattacharya [18] following methods of Dirr and Yip [16] showed that this is well defined.

9.3 Optimal pattern

We claim that the critical force is bounded by the maximum and the minimum of the adhesion strength, i.e.,

$$\varphi_{\min} := \min_{x_1, x_2} \varphi(x_1, x_2) \le F^* \le \max_{x_1, x_2} \varphi(x_1, x_2) =: \varphi_{\max}. \tag{9.6}$$

We prove this by considering any stationary solution g^* for an applied force F. It satisfies

$$-\alpha\,(-\Delta)^{\frac{1}{2}}\, g^* - \varphi(x, g^*) + F = 0. \tag{9.7}$$

Taking the Fourier transform of the equation above gives

$$\alpha|k|\widehat{g^*(x_1)} = \widehat{F} - \widehat{\varphi(x_1, g^*)} \tag{9.8}$$

for each k. In particular, setting $k = 0$, we see that $\widehat{F}(0) = \widehat{\varphi(x_1, g^*(x_1))}(0)$ or

$$F = \int_0^1 \varphi(\xi, g^*(\xi))d\xi. \tag{9.9}$$

We can see that the critical force is bounded by the adhesion strength. Furthermore, we can achieve the upper bound by a layer potential $\varphi(x_1, x_2) = \tilde{\varphi}(x_2)$. We can observe that the solution $g(x_1, x_2)$ should be also independent of x_1 which makes the non-local (half-Laplancian) term zero. Now let $\xi = \arg\max\tilde{\varphi}$. Notice that $g^* = \xi$ is a stationary solution for $F = \max\tilde{\varphi}$. It follows that $F^* \geq F = \max\tilde{\varphi}$.

We notice that if the adhesive strength distribution is not symmetric in the direction of peeling, i.e., it does not identically satisfy

$$\varphi(x_1, x_2) = \varphi(x_1, 1 - x_2), \tag{9.10}$$

then it is possible that the inverting the distribution could lead to a different critical peeling force. Physically, it means that the force required to peel the tape from right to left can be different from that required to peel the tape from left to right. This asymmetry has been observed by Xia et al. experimentally [87, 88]. We now examine how large this asymmetry can be, and the arrangement of the adhesive strength distribution that can give rise to this asymmetry.

We define the asymmetry in the critical force as

$$\mathcal{A} := F_{\mathrm{f}}^* - F_{\mathrm{b}}^*, \tag{9.11}$$

where the forward critical peeling force F_{f}^* is defined as

$$F_{\mathrm{f}}^* := \max_F \left\{ F \;\middle|\; 0 = -\alpha\,(-\Delta)^{\frac{1}{2}}\, g - \varphi(x_1, g) + F \text{ has a solution} \right\} \tag{9.12}$$

and the backward critical peeling force F_{b}^* is defined as

$$F_{\mathrm{b}}^* := \max_F \left\{ F \;\middle|\; 0 = -\alpha\,(-\Delta)^{\frac{1}{2}}\, g - \varphi(x_1, 1 - g) + F \text{ has a solution} \right\}. \tag{9.13}$$

By equation (9.6), we know that both peeling force are bounded by the maximum and the minimum of the adhesion strength. Therefore, the asymmetry is bounded by the contrast of the adhesion strength, i.e.,

$$\varphi_{\min} - \varphi_{\max} \leq \mathcal{A} \leq \varphi_{\max} - \varphi_{\min}. \tag{9.14}$$

Figure 9.4: The candidate adhesive strength distribution (dark gray is strong adhesion and light gray is weak adhesion) for maximizing asymmetry. This is plotted for $\alpha = \frac{1}{2\pi}$, $\varphi_{\max} - \varphi_{\min} = 1$, $\lambda = 0.5$, $h = 0.1$ and sum up to 1000 terms in (9.16)

Furthermore, these bounds are optimal in the sense that given any $\varepsilon > 0$, we can find φ^{ε} such that

$$\varphi^{\varepsilon}_{\min} - \varphi^{\varepsilon}_{\max} + \varepsilon \leq \mathcal{A} \leq \varphi^{\varepsilon}_{\max} - \varphi^{\varepsilon}_{\min} - \varepsilon. \tag{9.15}$$

To prove the optimality, we construct an adhesive strength distribution that takes two values only, $\varphi_{\min} < \varphi_{\max}$. We consider a two parameter family of adhesive strength distributions

$$\varphi_{\lambda,h}(x_1, x_2) = \begin{cases} \varphi_{\max} & -\frac{\lambda}{2} \leq x_1 \leq \frac{\lambda}{2} \quad \text{and} \quad 0.2 + f(x_1;\lambda) \leq x_2 \leq 0.2 + f(x;\lambda) + h \\ \varphi_{\min} & \text{otherwise,} \end{cases} \tag{9.16}$$

where

$$f(x;\lambda) = \sum_{n=1}^{\infty} -\frac{(\varphi_{\max} - \varphi_{\min})\sin(n\pi\lambda)}{\alpha n^2\pi^2}\cos(2n\pi x). \tag{9.17}$$

This pattern is shown in Figure 9.4.

Suppose we take Fourier transform to f, we have

$$\hat{f} = -2(\varphi_{\max} - \varphi_{\min})\sum_{n=1}^{\infty}\frac{\sin(n\pi\lambda)}{n\alpha|k|}\Big[\delta(k - 2n\pi) + \delta(k + 2n\pi)\Big]. \tag{9.18}$$

This leads us to

$$-\alpha|k|\hat{f} = -2(\varphi_{\max} - \varphi_{\min})\sum_{n=1}^{\infty}\frac{\sin(n\pi\lambda)}{n}\Big[\delta(k - 2n\pi) + \delta(k + 2n\pi)\Big]. \tag{9.19}$$

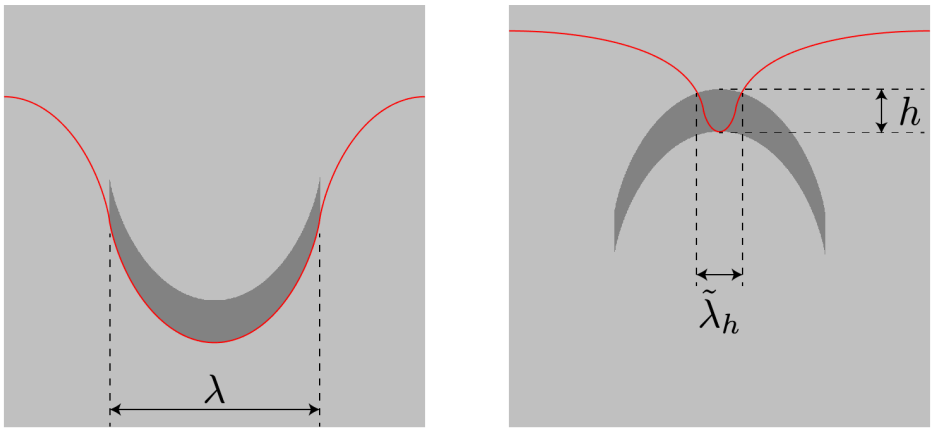

Figure 9.5: Schematic of critical front at forward (left figure) and backward direction (right figure) (dark gray is strong adhesion and light gray is weak adhesion)

Taking the inverse Fourier transform, we see that

$$-\alpha(-\Delta)^{\frac{1}{2}} f = \begin{cases} (1-\lambda)(\varphi_{\max} - \varphi_{\min}) & -\frac{\lambda}{2} \le x_1 \le \frac{\lambda}{2}, \\ -\lambda(\varphi_{\max} - \varphi_{\min}) & \text{otherwise.} \end{cases} \tag{9.20}$$

Now consider a curve

$$g_f(x) = 0.2 + f(x), \tag{9.21}$$

shown in Figure 9.5. According to (9.20), we have

$$-\alpha(-\Delta)^{1/2} g_f - \varphi_{\lambda,h}(x, g_f(x)) = -(\lambda\varphi_{\max} + (1-\lambda)\varphi_{\min}). \tag{9.22}$$

It follows that g_f is a stationary solution to the governing equation (9.3) with $F = \lambda\varphi_{\max} + (1-\lambda)\varphi_{\min}$. Therefore,

$$F_f^* \ge \lambda\varphi_{\max} + (1-\lambda)\varphi_{\min}. \tag{9.23}$$

We now turn to the backward direction. We seek to identify features of the critically pinned peel front. Given the periodicity and the fact that $\varphi_{\lambda,h}$ is symmetric in x_1, we expect that any stationary solution to be periodic. We observe from (9.9) that for any stationary solution, the applied force F is given by $\bar{\lambda}\varphi_{\max} + (1-\bar{\lambda})\varphi_{\min}$ where $\bar{\lambda}$ is the length of the projection of the peel front to the x_1 axes in the region with adhesive strength $\varphi_{\max}$. Further, given the shape of the $\varphi_{\max}$ region, we notice that for any curve this increases near to top of this region. Putting all these together, we

conclude that the critical pinned state is as shown in Figure 9.5, and given by the curve

$$g_b(x) = 0.8 - h + f(x, \tilde{\lambda}_h), \tag{9.24}$$

where $\tilde{\lambda}_h$ is as shown in the figure. Importantly, note that $\tilde{\lambda}_h \to 0$ as $h \to 0$ for each $\lambda \in (0, 1)$. Following the calculations above, we see that

$$F_b^* = \tilde{\lambda}_h \varphi_{\max} + (1 - \tilde{\lambda}_h)\varphi_{\min}. \tag{9.25}$$

Putting these together, we conclude that for this pattern, the asymmetry in the critical driving force is given by

$$\mathcal{A} \geq \lambda\varphi_{\max} + (1 - \lambda)\varphi_{\min} - \left(\tilde{\lambda}_h \varphi_{\max} + (1 - \tilde{\lambda}_h)\varphi_{\min}\right). \tag{9.26}$$

Now, take λ large enough that

$$\lambda\varphi_{\max} + (1 - \lambda)\varphi_{\min} > \varphi_{\max} - \frac{\varepsilon}{2}, \tag{9.27}$$

Now, given any ε, λ, take h small enough so that $\tilde{\lambda}_h$ is small enough to ensure that

$$\tilde{\lambda}_h \varphi_{\max} + (1 - \tilde{\lambda}_h)\varphi_{\min} < \varphi_{\min} + \frac{\varepsilon}{2}, \tag{9.28}$$

or

$$\mathcal{A} \geq \varphi_{\max} - \varphi_{\min} - \varepsilon. \tag{9.29}$$

This establishes the optimality of the bound.

We also examine this optimal pattern in equation (9.16) numerically. In this numerical study, we choose $\varphi_{\max} = 1$ and $\varphi_{\min} = 0$. We then fix the volume fraction of the strong adhesive (the volume fraction is λh) and vary the width of the pattern λ. We use three different volume fractions $10\%, 5\%, 0.5\%$ and vary λ from 0.5 to 0.95. The results are shown in Figure 9.6. As we expected, Figure 9.6(a) shows the forward critical force only depends on λ and it is independent of h. Figure 9.6(b) shows that the backward critical force can be reduced by decreasing h for any λ. As a result, we can achieve high asymmetry when λ is large and h is small as shown in Figure 9.6(c).

9.4 Topology optimization for maximum peeling force

In this section, we revisit the problem posed above using topology optimization. In the previous section, we fixed the applied force and studied

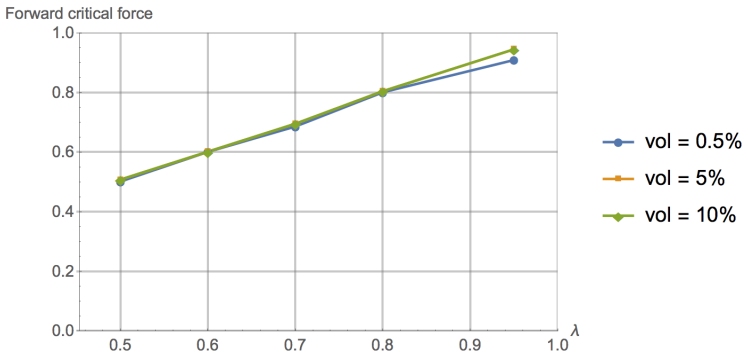

(a) Forward peeling force

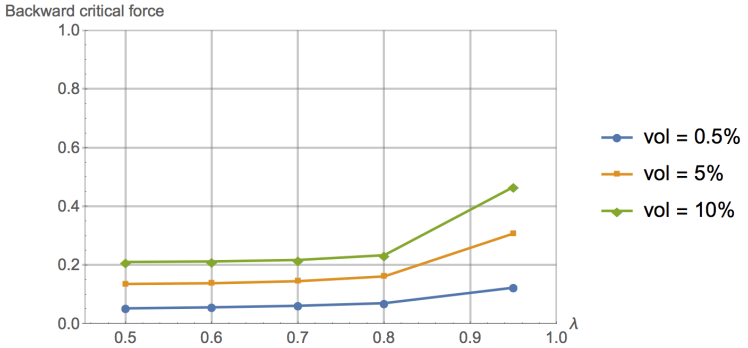

(b) Backward peeling force

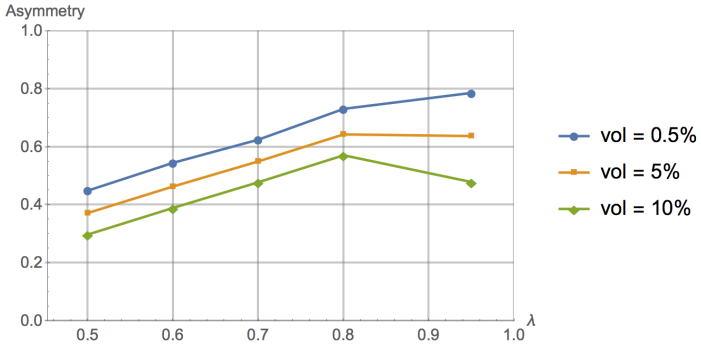

(c) Asymmetry

Figure 9.6: Parameter study of the optimal pattern

the propagation of the peel front. However, in some experiments like those of Xia et al. [87, 88] and for numerical purposes, it is preferable to impose an average velocity for the peel front and compute the force required to sustain it. We prescribe that

$$\int_0^1 \dot{g}(x_1, t) dx_1 = v_0. \tag{9.30}$$

At any instance of time, the peel front is still governed by the equation (9.3). Therefore, we find that the force required to sustain it is

$$F(t) = v_0 + \int_0^1 \left[-(-\Delta)^{\frac{1}{2}} g(x_1, t) - \varphi(x_1, g(x_1, t)) \right] dx_1. \tag{9.31}$$

Following an initial transient, we expect the peel front to be a pulsating wave, i.e., it advances by one period at a time interval of $1/v_0$:

$$g(x, t + 1/v_0) = g(x, t) + 1, \tag{9.32}$$

and the applied force $F(t)$ to be periodic (see for example Dondl and Bhattacharya [18] for theoretical justification or Xia et al. [87, 88] for experimental observations). We define the critical force to be

$$F^* = \max_t F(t) - v_0. \tag{9.33}$$

We remark that our governing equation (9.3) is rate-dependent (not invariant under a rescaling of time) and therefore the solution or peel front $g(x, t)$ depends on the applied velocity v_0. Therefore the critical force F^* as defined in (9.33) also depends on the applied velocity v_0. This definition approaches the previous definition as $v_0 \to 0$. On the other hand, the peel front behavior approach to rigid peel front ($\alpha \to \infty$) as $v_0 \to \infty$. Figure 9.7 shows the numerical study on the average velocity v_0. In this case, we pick

$$\varphi(x_1, x_2) = \sin(\pi x_1) \sin(\pi x_2) \tag{9.34}$$

and calculate $\max_t \left(F(t) - v_0 \right)$ under different v_0. The yellow dashed line indicates the critical force by equation (9.5). We can see that the critical force evaluated by equation (9.33) approaches the yellow line as the velocity approaches zero. For very high velocity, the peel front becomes rigid and it is always a straight line. Therefore, we know the critical force is

$$\max_{x_2} \int_0^1 \varphi(x_1, x_2) dx_1 = \int_0^1 \sin(\pi x_1) dx_1 = \frac{2}{\pi} \tag{9.35}$$

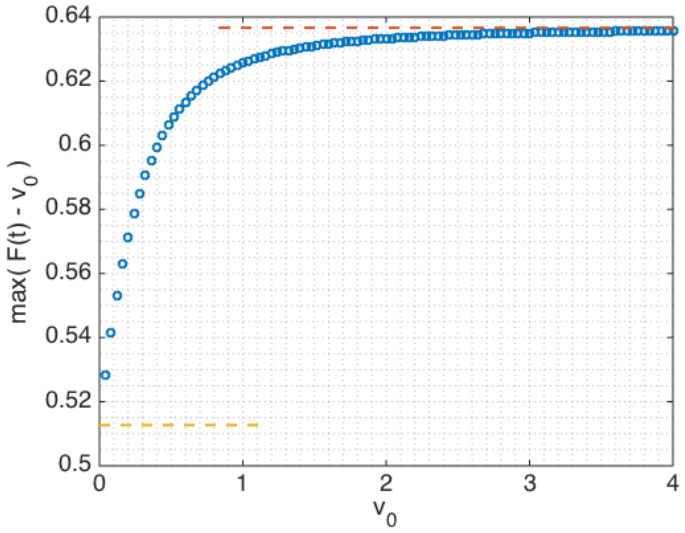

Figure 9.7: $\max_t(F(t) - v_0)$ in an impose average velocity peeling problem.

by equation (9.9). The critical force for rigid peel front is indicated as the red dashed line in Figure 9.7.

We are interested in finding the adhesive distribution that maximizes the critical force. Unfortunately, the definition in (9.33) is difficult to implement as it is the maximum over trajectories. So we replace the maximum with the integral of a high power:

$$\Phi = \int_0^T |F(t) - v_0|^p \, dt \tag{9.36}$$

for p a large enough integer, where $T = 1/v_0$ is the period that a pulsating solution takes to traverse one unit cell. Since p is large, the largest value of the integrand dominates the integral. Thus, equation (9.36) is an approximation of equation (9.33).

Next, we discretize in space, and let $\mathbf{g}(t)$ to be $N-$vector of the values of $g(x_1, t)$ at discrete points. The governing equation (9.3) becomes a system of ordinary differential equations

$$\dot{\mathbf{g}} = -\mathbb{K}\mathbf{g} - \boldsymbol{\varphi}(\mathbf{g}) + F\mathbf{1}, \tag{9.37}$$

where $\mathbb{K}$ is the discretized half-Laplancian operator, $\boldsymbol{\varphi}$ is a vector-value function mapping corresponding to the adhesion strength, and $\mathbf{1}$ is a vector which every element is one. Similarly, the driving force in equation (9.31) becomes

$$F = v_0 + \ell^T \left(\mathbb{K}\mathbf{g} + \boldsymbol{\varphi}(\mathbf{g}), \right) \tag{9.38}$$

where ℓ^T is the discretized integral operation.

We seek the maximum of (9.36) over all possible distributions φ where for each distribution the objective Φ is calculated over trajectories satisfying (9.37). This requires us to compute the sensitivity or variation of Φ with respect to φ. This in turn requires us to compute the sensitivity of the trajectory $\boldsymbol{g}$ to the distribution φ. This is difficult, and we sidestep this difficulty using the adjoint method.

Since the trajectories $\boldsymbol{g}$ satisfy (9.37), the objective function can be rewritten as

$$\Phi[\varphi] = \int_0^T \left(|F - v_0|^p + \boldsymbol{\lambda}^T \left(-\dot{\mathbf{g}} - \mathbb{K}\mathbf{g} - \varphi(\mathbf{g}) + F\mathbf{1} \right) \right) dt \tag{9.39}$$

for any time-dependent $N-$vector $\boldsymbol{\lambda}(t)$. We now take the variation of this objective with respect to the adhesive strength distribution by perturbing it in the direction η, $\varphi \to \varphi + s\eta$. We obtain

$$\begin{aligned} \frac{d}{ds}\Phi[\varphi + s\eta]\Big|_{s=0} = \int_0^T \Bigg[& \left(p|F - v_0|^{p-1} + \boldsymbol{\lambda}^T \mathbf{1} \right) \frac{\partial F}{\partial s}\Big|_{s=0} \\ & + \boldsymbol{\lambda}^T \left(-\dot{\mathbb{G}}\eta - \mathbb{K}\mathbb{G}\eta - \mathbb{P}\mathbb{G}\eta - \eta \right) \Bigg] dt, \end{aligned} \tag{9.40}$$

where $\mathbb{G} := \frac{\partial \mathbf{g}}{\partial \varphi}$ and $\mathbb{P} := \frac{\partial \varphi(\mathbf{g})}{\partial \mathbf{g}}$. We would like to choose $\boldsymbol{\lambda}$ so that we do not need to compute $\mathbb{G}$. To this end, take the derivative of (9.38) with respect to s,

$$\frac{\partial F}{\partial s}\Big|_{s=0} = \ell^T \left(\mathbb{K}\mathbb{G}\eta + \mathbb{P}\mathbb{G}\eta + \eta \right). \tag{9.41}$$

Substitute (9.41) into (9.40) and integrate by parts to conclude

$$\begin{aligned} \frac{d}{ds}\Phi[\varphi + s\eta]\Big|_{s=0} = \int_0^T & \left\{ \left[(p|F - v_0|^{p-1} + \boldsymbol{\lambda}^T \mathbf{1})\ell^T(\mathbb{K} + \mathbb{P}) + \dot{\boldsymbol{\lambda}}^T - \boldsymbol{\lambda}^T(\mathbb{K} + \mathbb{P}) \right] \mathbb{G}\eta \right. \\ & \left. + \left[(p|F - v_0|^{p-1} + \boldsymbol{\lambda}^T \mathbf{1})\ell^T - \boldsymbol{\lambda}^T \right] \eta \right\} dt \\ & + \left[-\boldsymbol{\lambda}^T \mathbb{G}\eta \right] \Big|_{t=0}^T . \end{aligned} \tag{9.42}$$

We are now in a position to choose $\boldsymbol{\lambda}$ such that $\mathbb{G}$ does not appear in this equation.

First, we observe that since the initial condition $g(x_1, 0)$ is independent of the adhesion strength distribution, we have $\mathbb{G}\big|_{t=0} = 0$. In order to eliminate the other boundary term in (9.42), we require that

$$\boldsymbol{\lambda}\big|_{t=T} = 0. \tag{9.43}$$

We also require $\boldsymbol{\lambda}$ to satisfy

$$\dot{\boldsymbol{\lambda}} - (\mathbb{K} + \mathbb{P})^T \boldsymbol{\lambda} + (pF^{p-1} + \boldsymbol{\lambda}^T \mathbf{1})(\mathbb{K} + \mathbb{P})^T \boldsymbol{\ell} = 0, \tag{9.44}$$

so that the first term in the integrand of (9.42) is zero. With this choice of $\boldsymbol{\lambda}$, (9.42) reduces to

$$\left.\frac{d\Phi}{ds}\right|_{s=0} = \int_0^T \left[(p|F - v_0|^{p-1} + \boldsymbol{\lambda}^T \mathbf{1})\boldsymbol{\ell}^T - \boldsymbol{\lambda}^T\right] \boldsymbol{\eta} dt. \tag{9.45}$$

We use this formula for the sensitivity.

We discretize the equations in time and find the optimal design using the algorithm in Table 9.1.

initialization:

Calculate the stiffness matrix $\mathbb{K}$;

Set time step Δt and a basis $\{\boldsymbol{\eta}_\alpha\}$ for the adhesive strength distribution

Set initial adhesive strength distribution $\boldsymbol{\varphi}$ and tolerance ε;

repeat

Forward problem. Explicitly solve (9.37) subject to $\boldsymbol{g}(0) = 0$:

Iteratively update
$\mathbf{g}(t + \Delta t) = \mathbf{g}(t) + \left[\left(\mathbf{1}\boldsymbol{\ell}^T - \mathbb{I}\right)(\mathbb{K}\mathbf{g}(t) + \boldsymbol{\varphi}(\mathbf{g}(t))) + v_0\mathbf{1}\right] \times \Delta t$ from $t = 0$ to $t = T$.

Find the force. Calculate the force at each time step from (9.38).

Adjoint problem. Explicitly solve (9.44) subject to (9.43) backward in time:

Calculate $\mathbb{P}(t) = \frac{\partial \boldsymbol{\varphi}(\boldsymbol{g}(t))}{\partial \boldsymbol{g}}$ for each discrete t,

Iteratively update $\boldsymbol{\lambda}(t + \Delta t) =$
$\boldsymbol{\lambda}(t) + \left[-(\mathbb{K} + \mathbb{P}(t))^T \boldsymbol{\lambda}(t) + (p|F - v_0|^{p-1}(t) + \boldsymbol{\lambda}^T(t)\mathbf{1})(\mathbb{K} + \mathbb{P}(t))^T \boldsymbol{\ell}\right] \times \Delta t$
from $t = T$ to $t = 0$.

Compute the sensitivity: $S_\alpha = \int_0^T \left[(p|F - v_0|^{p-1} + \boldsymbol{\lambda}^T \mathbf{1})\boldsymbol{\ell}^T - \boldsymbol{\lambda}^T\right](\boldsymbol{\eta}_\alpha) dt$.

Update the adhesive strength distribution: $\boldsymbol{\varphi} = \boldsymbol{\varphi} + \sum_\alpha S_\alpha \boldsymbol{\eta}_\alpha$.

until *Difference* $||\Delta\boldsymbol{\varphi}|| \leq \varepsilon$;

Table 9.1: Pseudo-code for computing the optimal adhesive distribution for maximal critical force

We demonstrate this algorithm with the following numerical examples. We consider a square unit cell. We specify the adhesive strength distribution

to be piecewise linear on a $M \times M$ grid, and discretize $\boldsymbol{g}$ using N points. Figure 9.8 shows the results of a numerical examples with

$$N = 128, \quad M = 25, \quad v_0 = 1, \quad T = 1, \quad \Delta t = 0.01, \quad \alpha = \frac{1}{2\pi}, \quad p = 11,$$

and where the initial adhesive strength distribution is

$$\varphi(x_1, x_2) = 0.5\Big[1 - 0.1\left[\cos(2\pi x_1) + \cos(2\pi x_2)\right]\Big]. \tag{9.46}$$

We also impose the additional constraints that

$$0 \leq \varphi(x_1, x_2) \leq 1, \quad \int \varphi(x_1, x_2) d\Omega = 0.5. \tag{9.47}$$

We see that the adhesive strength distribution evolves to the layer potential anticipated in Section 9.3. Figure 9.8(f) shows the peeling force for the various adhesive strength distribution. We see that it reaches that the maximum peeling force increases and eventually reaches the upper bounds $v_0 + \varphi_{\max} = 2$. All of this is as anticipated in Section 9.3.

9.5 Topology optimization for maximum asymmetry

In this section, we optimize the adhesive strength distribution for the highest asymmetry. Similar to previous section, we use the p-norm as our objective function.

$$\begin{aligned}\Phi_{\text{asymmetry}} = \int_0^T \Big[& |F_+ - v_0|^p - |F_- - v_0|^p \\ & + \boldsymbol{\lambda}_+^T \left(-\dot{\mathbf{g}}_+ - \mathbb{K}\mathbf{g}_+ - \boldsymbol{\varphi}(\mathbf{g}_+) + F_+ \mathbf{1}\right) \\ & - \boldsymbol{\lambda}_-^T \left(-\dot{\mathbf{g}}_- - \mathbb{K}\mathbf{g}_- - \boldsymbol{\varphi}(\mathbf{1} - \mathbf{g}_-) + F_- \mathbf{1}\right) \Big] dt \end{aligned} \tag{9.48}$$

The only difference in this section is that we have to introduce two Lagrange multiplier $\boldsymbol{\lambda}_+$ and $\boldsymbol{\lambda}_-$ where the subscript plus and minus correspond to the forward and backward peeling directions respectively. We then use the procedure in Section 9.3 to perform the sensitivity analysis. In this optimization process, we choose the following parameters:

$$N = 256, \quad M = 100, \quad v_0 = 1, \quad T = 1, \quad \Delta t = 0.005, \quad \alpha = \frac{1}{2\pi}, \quad p = 11.$$

We also restrict $0 \leq \varphi(x_1, x_2) \leq 1$ and $\int \varphi(x_1, x_2) d\Omega = 0.1$ with the initial distribution

$$\varphi(x_1, x_2) = 0.1\Big[1 - 0.1\left[\cos(2\pi x_1) + \cos(2\pi x_2)\right]\Big]. \tag{9.49}$$

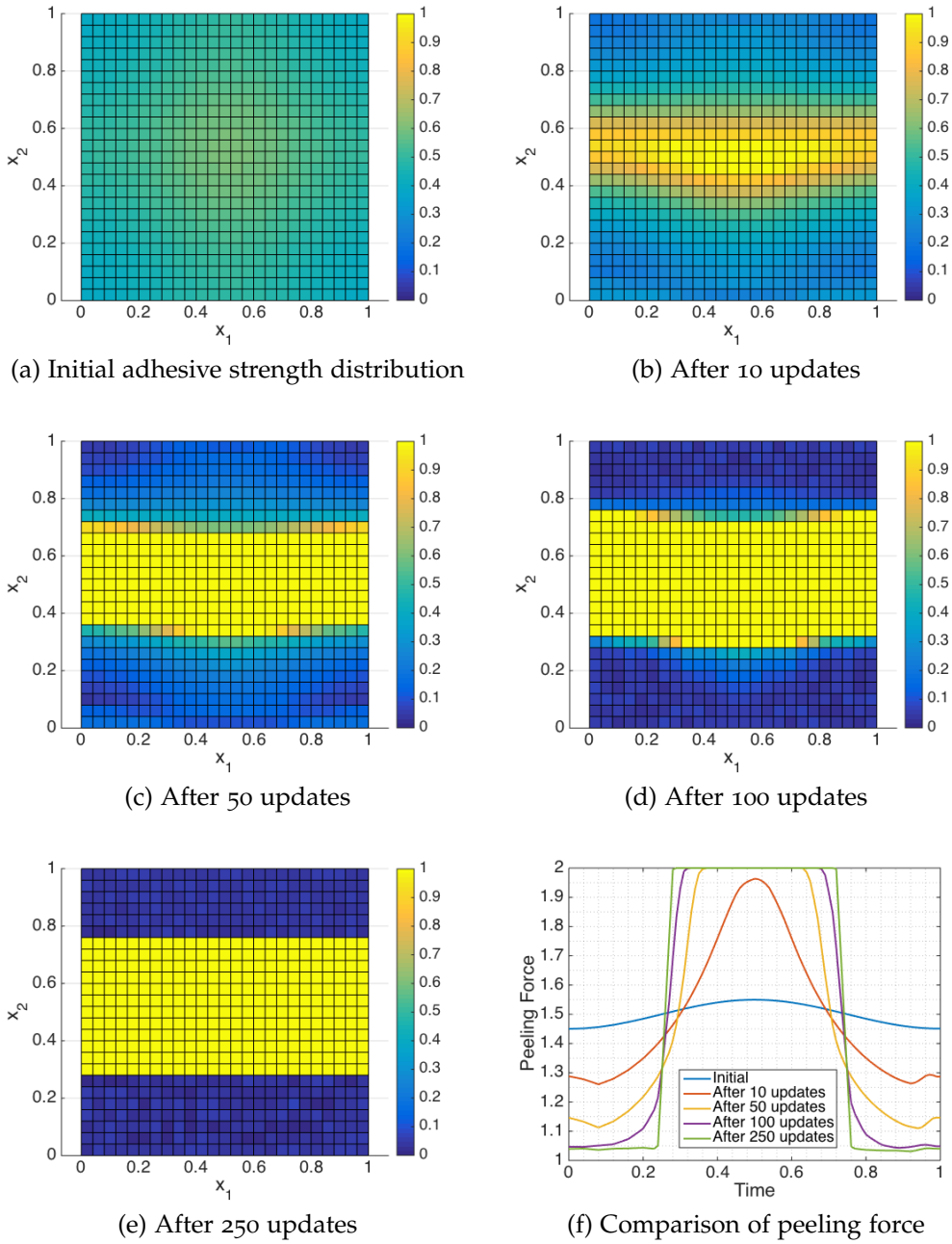

(a) Initial adhesive strength distribution

(b) After 10 updates

(c) After 50 updates

(d) After 100 updates

(e) After 250 updates

(f) Comparison of peeling force

Figure 9.8: Topology optimization for maximum peeling force.

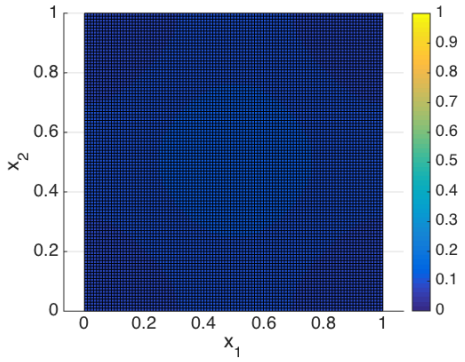

(a) Initial adhesive strength distribution

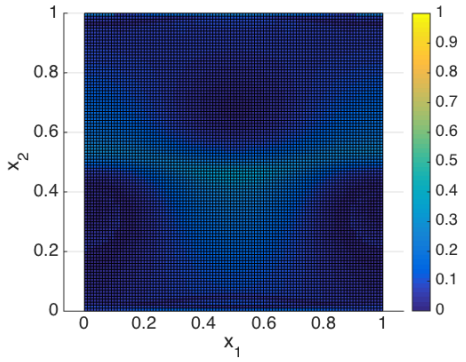

(b) After 3 updates

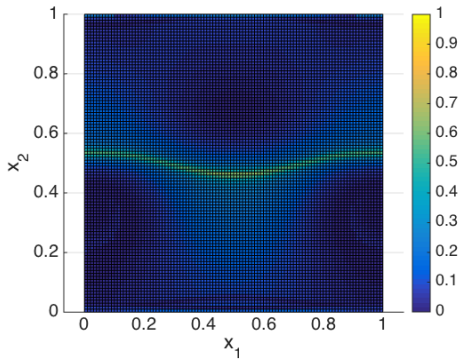

(c) After 6 updates

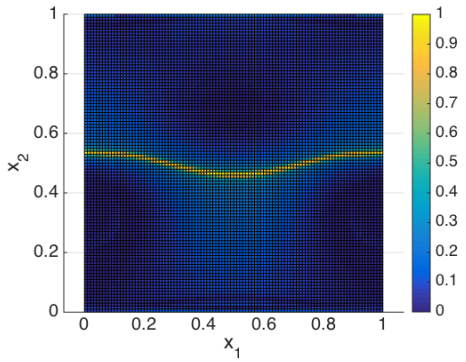

(d) After 10 updates

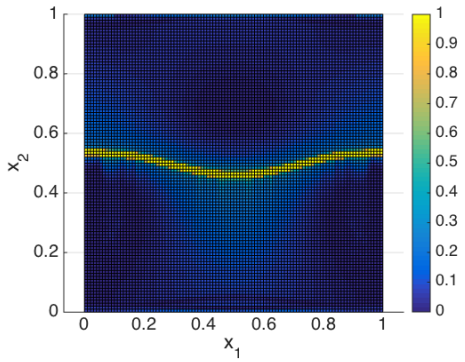

(e) After 30 updates

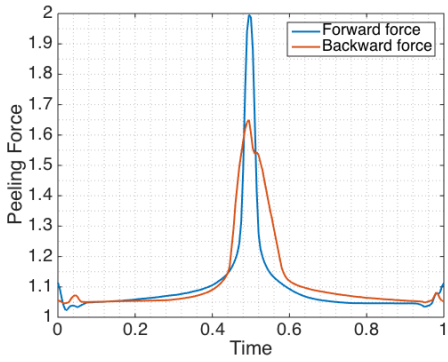

(f) Comparison of peeling force (after 30 updates)

Figure 9.9: Topology optimization for maximum asymmetry.

The progress of the optimization is shown in Figure 9.9. We can see that the optimization algorithm forms a curve with strong adhesive strength to increase asymmetry in critical peeling force. The forward and backward peeling force for the adhesive strength after 30 updates is shown in Figure 9.9(f). The peeling force in the forward peeling direction has a sharp peak which reaches the upper bounds of peeling force. In contrast, the peeling force in the backward peeling direction is a blunt curve with lower critical peeling force. The optimization algorithm distributes the adhesive strength to maximize the asymmetry. However, we have to point out that there is no theoretical bounds for asymmetry with finite spatial resolution adhesive strength distribution. Therefore, we are not able to compare our result with any theoretical bounds.

We also change the volume fraction of the initial guess

$$\varphi(x_1, x_2) = vol \times \Big[1 - 0.1\left[\cos(2\pi x_1) + \cos(2\pi x_2)\right]\Big], \tag{9.50}$$

where vol range from 2.5% to 25%. The relationship between asymmetry and the volume fraction is shown in Figure 9.10(a). The results show that the asymmetry slightly increases when the volume fraction of the strong adhesive strength decreases from 25% to 12.5%. However, the asymmetry decreases dramatically in the small volume fraction region ($vol < 10\%$). This is because the resolution of the potential is not fine enough to form a thin curve line. For example, the potential resolution in Figure 9.10(b) ($vol = 2.5\%$) is not high enough so the strong adhesive strength can only form an almost straight line.

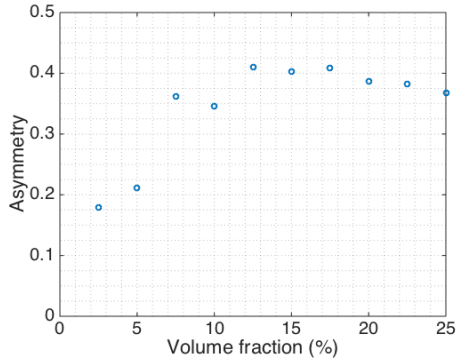

(a) Relationship between asymmetry and the volume fraction of the initial guess

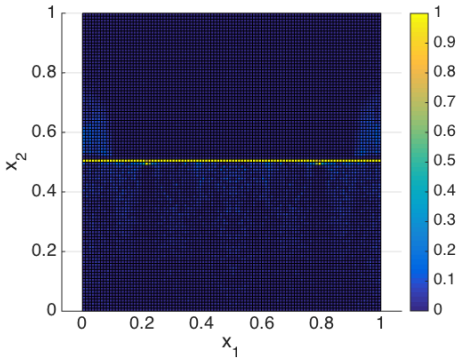

(b) volume fraction = 2.5%

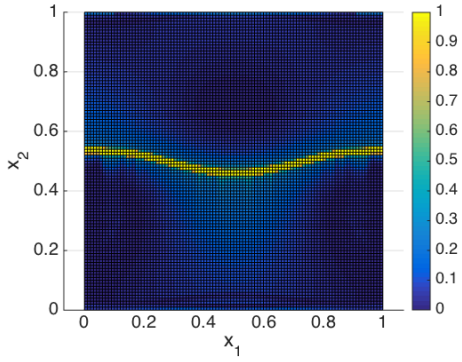

(c) volume fraction = 10%

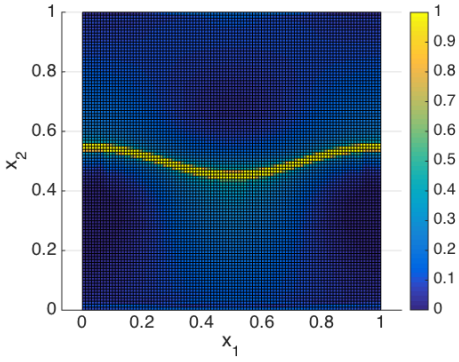

(d) volume fraction = 15%

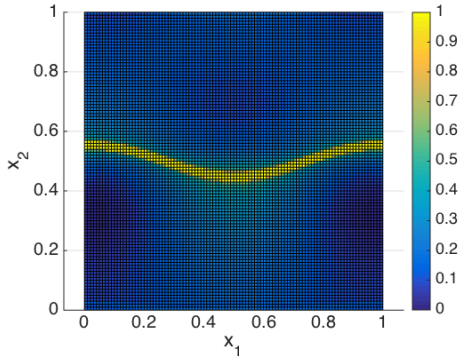

(e) volume fraction = 20%

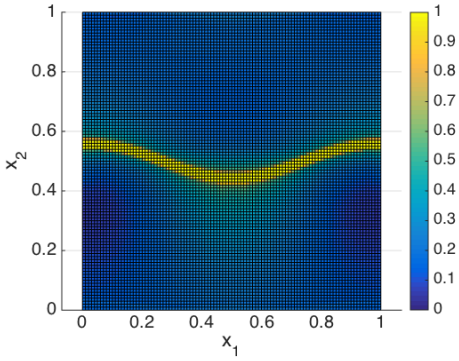

(f) volume fraction = 25%

Figure 9.10: The volume fraction effect

Chapter 10

CONCLUSIONS AND FUTURE WORK

10.1 Conclusions

In this thesis, the crack propagation in heterogeneous materials is studied. In order to have a steady macroscopic propagation in heterogeneous materials, we introduce the surfing boundary condition which can ensure a macroscopic steady crack propagation in Chapter 3. Then we define the effective toughness of heterogeneous materials as the peak of the J-integral, an integral which can measure the driving force on the crack, during crack propagation. If the driving force on the crack does not exceed the effective toughness of heterogeneous materials, the crack cannot propagate through and break the heterogeneous material. In Chapter 4, we showed that the macroscopic J-integral in heterogeneous materials is well-defined and it can be calculated with the homogenized stress and strain field. Further, we showed that the path-independency can be recovered if the material is macroscopically homogeneous and the integral path is large compared to the size of the heterogeneities.

By using the surfing boundary condition, we studied the crack propagation in heterogeneous materials semi-analytically, numerically, and experimentally. We use a semi-analytical method to study crack propagation in heterogeneous materials in Chapter 5. We found that the effective toughness is higher when the crack propagates from the compliance material towards the stiff material. Furthermore, we can construct a heterogeneous material which has asymmetric toughness. We also studied the crack propagation in heterogeneous numerically in Chapter 6. With the assistance of the phase field fracture method, we are able to simulate the crack propagation in heterogeneous materials. The simulation results show that the effective toughness can be enhanced and controlled by the microstructure. Therefore, we parametrically optimize the microstructure for better performance. We also use the phase field fracture method to simulate the crack propagation in asymmetric microstructures. In order to study crack propagation in heterogeneous specimens experimentally, we developed an experimen-

tal configuration which can apply the surfing boundary on specimens in Chapter 7. We also improve the grid method, a non-contact full-field measurement method, to reduce the measurement bias. By using the experimental configuration and the improved grid method, we studied the crack propagation in heterogeneous specimens experimentally. The experimental results show that the effective toughness in heterogeneous specimens is higher than the homogeneous specimen.

In addition to studies crack propagation in heterogeneous materials, we also studied a model problem of fracture mechanics: the peeling problem in Chapter 9. We first found the optimal microstructures (adhesive distributions) for maximum peeling force and maximum asymmetry. Furthermore, we proposed an adjoint method to topology optimize the microstructure (adhesive distribution).

In conclusion, we have shown that the microstructure can control and enhance the effective toughness in heterogeneous materials. We conclude that manipulating and optimizing the microstructure is a good method to push the boundaries of material's performance further. The works presented in this thesis can be extended in many directions, as shown in the next section.

10.2 Future works

Topology optimization with phase field fracture method (in discrete scheme) We explore the use of the phase field fracture method for topology optimization. The key idea is using the approach similar to that in Chapter 9 to develop an adjoint method to optimize the microstructure. First we consider the phase field fracture method in Chapter 6:

$$\mathcal{P}^{\ell}(u,v) = \int_{\Omega} \alpha(v) W(\nabla u) + \frac{G}{4c_w}\left(\frac{w(v)}{\ell} + \ell|\nabla v|^2\right) dx - \int_{\Omega} b_i u_i dx - \int_{\partial_2\Omega} t_i^* u_i ds \tag{10.1}$$

with the restriction on damage field $0 \le v \le 1$. The Euler-Lagrange equations of the phase field fracture method are

$$\frac{\delta \mathcal{P}^{\ell}}{\delta u} = 0 \implies \frac{\partial}{\partial x_j}\left(\alpha(v)\frac{\partial W(\nabla u)}{\partial F_{ij}}\right) + b_i = 0 \tag{10.2}$$

and

$$\frac{\delta \mathcal{P}^{\ell}}{\delta v} = 0 \implies \alpha'(v)W(\nabla u) + \frac{G}{4c_w}\left(\frac{w'(v)}{\ell} - 2\ell\nabla^2 v\right) - \frac{\ell}{2c_w}(\nabla G)\cdot(\nabla v) = 0. \tag{10.3}$$

A common restriction in fracture mechanics is the crack irreversible condition

$$\dot{v} \geq 0, \tag{10.4}$$

where the superimposed dot represents the derivative with respect to time. If we discretized the system in time, the crack irreversible condition becomes

$$v^{n+1} \geq v^{n}, \tag{10.5}$$

where the superscript indicates the time steps. Therefore, the solution of equation (10.1) at each time step has to satisfy

$$f_i(u_i^n, v^n) := \frac{\partial}{\partial x_j}\left(\alpha(v^n)\frac{\partial W(\nabla u^n)}{\partial F_{ij}}\right) + b_i^n = 0 \tag{10.6}$$

and

$$g(u^n, v^n \mid v^{n-1}, 1) := \left[\alpha'(v^n)W(\nabla u^n) + \frac{G}{4c_w}\left(\frac{w'(v^n)}{\ell} - 2\ell\nabla^2 v^n\right) - \frac{\ell}{2c_w}(\nabla G)\cdot(\nabla v^n)\right] (v^n - v^{n-1})(1 - v^n) = 0. \tag{10.7}$$

We have to point out that equation (10.7) indicates that the solution (of a constraint minimization problem) are either in equilibrium state (equation (10.3) is satisfied) or on the boundaries ($v^n = 1$ or $v^n = v^{n-1}$). The schematic idea of equation (10.6) is shown in Figure 10.1.

We introduce the design variable field ξ that controls material properties. Therefore, the elastic energy density and the toughness depends on the design variable

$$W = W(\nabla u, \xi), \quad G = G(\xi). \tag{10.8}$$

The objective of this optimization problem is maximize the effective toughness. We use the p-norm of the J-integral with high order p to approximate the effective toughness. Therefore, the objective function is

$$\Phi = \sum_{n=0}^{T} \left[J^p(u^n, v^n, \xi)\right] \Delta t. \tag{10.9}$$

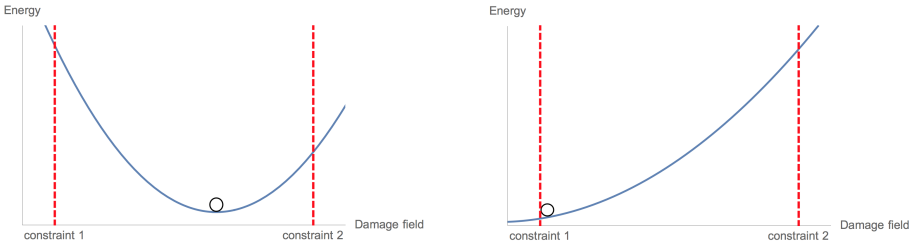

(a) In equilibrium state (b) On boundary

Figure 10.1: The minima of a constraint minimization problem is either in the equilibrium state or on the boundary

Since the solution of equation (10.1) at each time step has to satisfy equation (10.6) and (10.7), we can rewrite the objective function as

$$\Phi = \sum_{n=0}^{T} \left[J^p(u^n, v^n, \xi) + \int_\Omega \Big(\lambda_k f_k(u^n, v^n, \xi) + \mu g(u^n, v^n, \xi | v^{n-1}, 1) \Big) dx \right] \Delta t, \tag{10.10}$$

where λ_i and μ are arbitrary functions and v^{-1} is the initial guess of the damage field at time $t = 0$. Now suppose we discrete the system in space, then we are able to take derivate of J, f_i and g with respect to u and v directly. Thus, we introduce a small perturbation on the material parameter $\xi \to \xi + s\eta$, and then the derivative of the objection function with respect

to s becomes

$$
\begin{aligned}
\left.\frac{d\Phi}{ds}\right|_{s=0} = \\
&\sum_{n=0}^{T-1}\Bigg[\left(pJ^{p-1}\frac{\partial J}{\partial u_i^n}+\int_\Omega \lambda_k^n\frac{\partial f_k(u^n,v^n,\xi)}{\partial u_i^n}+\mu^n\frac{\partial g(u^n,v^n,\xi|v^{n-1},1)}{\partial u_i^n}dx\right)\frac{\partial u_i^n}{\partial \xi}\\
&\quad\left(pJ^{p-1}\frac{\partial J}{\partial v^n}+\int_\Omega \lambda_k^n\frac{\partial f_k(u^n,v^n,\xi)}{\partial v^n}+\mu^n\frac{\partial g(u^n,v^n,\xi|v^{n-1},1)}{\partial v^n}\right.\\
&\qquad\left.+\mu^{n+1}\frac{\partial g(u^{n+1},v^{n+1},\xi|v^n,1)}{\partial v^n}dx\right)\frac{\partial v^n}{\partial \xi}\\
&\quad\left(pJ^{p-1}\frac{\partial J}{\partial \xi}+\int_\Omega \lambda_k^n\frac{\partial f_k(u^n,v^n,\xi)}{\partial \xi}+\mu^n\frac{\partial g(u^n,v^n,\xi|v^{n-1},1)}{\partial \xi}dx\right)\Bigg]\eta\,\Delta t\\
+\quad&\Bigg[\left(pJ^{p-1}\frac{\partial J(u^T,v^T,\xi)}{\partial u_i^T}+\int_\Omega \lambda_k^T\frac{\partial f_k(u^T,v^T,\xi)}{\partial u_i^T}\right.\\
&\qquad\left.+\mu^T\frac{\partial g(u^T,v^T,\xi|v^{T-1},1)}{\partial u_i^T}dx\right)\frac{\partial u_i^T}{\partial \xi}\\
&\quad\left(pJ^{p-1}\frac{\partial J(u^T,v^T,\xi)}{\partial v^T}+\int_\Omega \lambda_k^T\frac{\partial f_k(u^T,v^T,\xi)}{\partial v^T}\right.\\
&\qquad\left.+\mu^T\frac{\partial g(u^T,v^T,\xi|v^{T-1},1)}{\partial v^T}dx\right)\frac{\partial v^T}{\partial \xi}\\
&\quad\left(pJ^{p-1}\frac{\partial J(u^T,v^T,\xi)}{\partial \xi}+\int_\Omega \lambda_k^T\frac{\partial f_k(u^T,v^T,\xi)}{\partial \xi}\right.\\
&\qquad\left.+\mu^T\frac{\partial g(u^T,v^T,\xi|v^{T-1},1)}{\partial \xi}dx\right)\Bigg]\eta\,\Delta t.
\end{aligned}
\tag{10.11}
$$

We choose λ^T and μ^T such that

$$
\begin{aligned}
pJ^{p-1}(u^T,v^T,\xi)\frac{\partial J(u^T,v^T,\xi^T)}{\partial u_i^T}+\int_\Omega \lambda_k^T\frac{\partial f_k(u^T,v^T,\xi^T)}{\partial u_i^T}\\
+\mu^T\frac{\partial g(u^T,v^T,\xi^T|v^{T-1},1)}{\partial u_i^T}dx=0
\end{aligned}
\tag{10.12}
$$

$$
\begin{aligned}
pJ^{p-1}(u^T,v^T,\xi)\frac{\partial J(u^T,v^T,\xi^T)}{\partial v^T}+\int_\Omega \lambda_k^T\frac{\partial f_k(u^T,v^T,\xi^T)}{\partial v^T}\\
+\mu^T\frac{\partial g(u^T,v^T,\xi^T|v^{T-1},1)}{\partial v^T}dx=0.
\end{aligned}
\tag{10.13}
$$

We then solve $(\lambda^{T-1}, \mu^{T-1}) \cdots (\lambda^0, \mu^0)$ by the following equations

$$pJ^{p-1}(u^n, v^n, \xi)\frac{\partial J(u^n, v^n, \xi)}{\partial u_i^n} + \int_\Omega \lambda_k^n \frac{\partial f_k(u^n, v^n, \xi)}{\partial u_i^n} + \mu^n \frac{\partial g(u^n, v^n, \xi | v^{n-1}, 1)}{\partial u_i^n} dx = 0 \tag{10.14}$$

$$pJ^{p-1}(u^n, v^n, \xi)\frac{\partial J(u^n, v^n, \xi)}{\partial v^n} + \int_\Omega \lambda_k^n \frac{\partial f_k(u^n, v^n, \xi)}{\partial v^n} + \mu^n \frac{\partial g(u^n, v^n, \xi | v^{n-1}, 1)}{\partial v^n} + \mu^{n+1} \frac{\partial g(u^{n+1}, v^{n+1}, \xi | v^n, 1)}{\partial v^n} dx = 0. \tag{10.15}$$

Equation (10.12) - (10.15) is just linear equations of λ and μ. Therefore, solving equation (10.12) - (10.15) is not expensive. By choosing this particular $\{\lambda^n, \mu^n\}_{n=0}^T$, the sensitivity function can be reduced as follows:

$$\left.\frac{d\Phi}{ds}\right|_{s=0} = \sum_{n=0}^{T} \left[\left(pJ^{p-1}(u^n, v^n, \xi)\frac{\partial J(u^n, v^n, \xi)}{\partial \xi} + \int_\Omega \lambda_k^n \frac{\partial f_k(u^n, v^n, \xi)}{\partial \xi} + \mu^n \frac{\partial g(u^n, v^n, \xi | v^{n-1}, 1)}{\partial \xi} dx \right) \right] \eta \, \Delta t. \tag{10.16}$$

Then we have the sensitivity of the design variable ξ. This shows the feasibility of the method.

Experimental studies

One interesting direction of the experimental studies is the asymmetric toughness. The toughness can be asymmetric if the microstructure is asymmetric. This is not a common property in natural materials but it can be easily achieved by the composite materials. Therefore, we can use the surfing loading device to measure the effective toughness of the specimens, as shown in 10.2.

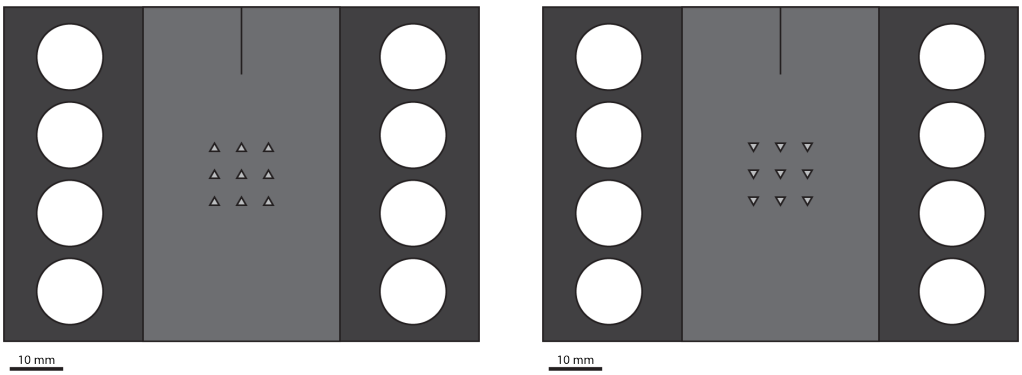

(a) Tough direction (b) Weak direction

Figure 10.2: Asymmetric specimens

BIBLIOGRAPHY

[1] Luigi Ambrosio and Vincenzo Maria Tortorelli. "Approximation of functional depending on jumps by elliptic functional via t convergence". In: *Communications on Pure and Applied Mathematics* 43.8 (1990), pp. 999–1036.

[2] Grigory Isaakovich Barenblatt. "The mathematical theory of equilibrium cracks in brittle fracture". In: *Advances in applied mechanics* 7 (1962), pp. 55–129.

[3] Ted Belytschko, Nicolas Moës, Shuji Usui, and Chandu Parimi. "Arbitrary discontinuities in finite elements". In: *International Journal for Numerical Methods in Engineering* 50.4 (2001), pp. 993–1013.

[4] Michael J. Borden, Clemens V. Verhoosel, Michael A. Scott, Thomas J.R. Hughes, and Chad M. Landis. "A phase-field description of dynamic brittle fracture". In: *Computer Methods in Applied Mechanics and Engineering* 217 (2012), pp. 77–95.

[5] Blaise Bourdin. "Numerical implementation of a variational formulation of quasi-static brittle fracture". In: *Interfaces Free Bound.* 9 (Aug. 2007), pp. 411–430.

[6] Blaise Bourdin, Gilles A. Francfort, and Jean-Jacques Marigo. "Numerical experiments in revisited brittle fracture". In: *J. Mech. Phys. Solids* 48.4 (2000), pp. 797–826.

[7] Blaise Bourdin, Gilles A. Francfort, and Jean-Jacques Marigo. "The Variational Approach to Fracture". In: *J. Elasticity* 91.1-3 (2008), pp. 1–148.

[8] Blaise Bourdin, Christopher J. Larsen, and Casey L. Richardson. "A time-discrete model for dynamic fracture based on crack regularization". In: *International journal of fracture* 168.2 (2011), pp. 133–143.

[9] Blaise Bourdin, Jean-Jacques Marigo, Corrado Maurini, and Paul Sicsic. "Morphogenesis and propagation of complex cracks induced by thermal shocks". In: *Physical review letters* 112.1 (2014), p. 014301.

[10] Allan F. Bower and Michael Ortiz. "A three-dimensional analysis of crack trapping and bridging by tough particles". In: *Journal of the Mechanics and Physics of Solids* 39.6 (1991), pp. 815–858.

[11] Andrea Braides. "Homogenization of some almost periodic coercive functional". In: *Rendiconti. Accademia Nazionale delle Scienze detta dei XL. Serie V. Memorie di Matematica e Applicazioni* 9 (1985), pp. 313–321.

[12] H.F. Bueckner. "Novel principle for the computation of stress intensity factors". In: *Zeitschrift fuer Angewandte Mathematik & Mechanik* 50.9 (1970).

[13] Edwin P. Chan, Dongchan Ahn, and Alfred J. Crosby. "Adhesion of patterned reactive interfaces". In: *The Journal of Adhesion* 83.5 (2007), pp. 473–489.

[14] Jun Young Chung and Manoj K. Chaudhury. "Roles of discontinuities in bio-inspired adhesive pads". In: *Journal of The Royal Society Interface* 2.2 (2005), pp. 55–61.

[15] Brian Cox and Qingda Yang. "In quest of virtual tests for structural composites". In: *science* 314.5802 (2006), pp. 1102–1107.

[16] Nicolas Dirr and Nung Kwan Yip. "Pinning and de-pinning phenomena in front propagation in heterogeneous media". In: *Interfaces and Free Boundaries* 8.1 (2006), pp. 79–109.

[17] John Dolbow and Ted Belytschko. "A finite element method for crack growth without remeshing". In: *International journal for numerical methods in engineering* 46.1 (1999), pp. 131–150.

[18] Patrick W. Dondl and Kaushik Bhattacharya. "Effective behavior of an interface propagating through a periodic elastic medium". In: *Interfaces and Free Boundaries* 18 (2016), pp. 91–113.

[19] Donald S. Dugdale. "Yielding of steel sheets containing slits". In: *Journal of the Mechanics and Physics of Solids* 8.2 (1960), pp. 100–104.

[20] Eduardo N Dvorkin, Alberto M Cuitiño, and Gustavo Gioia. "Finite elements with displacement interpolated embedded localization lines insensitive to mesh size and distortions". In: *International Journal for Numerical Methods in Engineering* 30.3 (1990), pp. 541–564.

[21] MGGV Elices, GV Guinea, J Gomez, and J Planas. "The cohesive zone model: advantages, limitations and challenges". In: *Engineering fracture mechanics* 69.2 (2002), pp. 137–163.

[22] AM Ermi and LA James. "Miniature center-cracked-tension specimen for fatigue crack growth testing". In: *The Use of Small-Scale Specimens for Testing Irradiated Material*. ASTM International, 1986.

[23] Anthony G. Evans and Katherine T. Faber. "Toughening of ceramics by circumferential microcracking". In: *Journal of the American Ceramic Society* 64.7 (1981), pp. 394–398.

[24] Katherine T. Faber and Anthony G. Evans. "Crack deflection processes—I. Theory". In: *Acta Metallurgica* 31.4 (1983), pp. 565–576.

[25] Katherine T. Faber and Anthony G. Evans. "Crack deflection processes—II. Experiment". In: *Acta Metallurgica* 31.4 (1983), pp. 577–584.

[26] Gilles A. Francfort and Jean-Jacques Marigo. "Revisiting brittle fracture as an energy minimization problem". In: *J. Mech. Phys. Solids.* 46.8 (1998), pp. 1319–1342.

[27] Huajian Gao. "Fracture analysis of nonhomogeneous materials via a moduli-perturbation approach". In: *International Journal of Solids and Structures* 27.13 (1991), pp. 1663–1682.

[28] Huajian Gao and James R. Rice. "A first-order perturbation analysis of crack trapping by arrays of obstacles". In: *ASME, Transactions, Journal of Applied Mechanics* 56 (1989), pp. 828–836.

[29] Thomas C. Gasser and Gerhard A. Holzapfel. "3d crack propagation in unreinforced concrete.: A two-step algorithm for tracking 3d crack paths". In: *Computer Methods in Applied Mechanics and Engineering* 195.37 (2006), pp. 5198–5219.

[30] Thomas C. Gasser and Gerhard A. Holzapfel. "Modeling 3D crack propagation in unreinforced concrete using PUFEM". In: *Computer Methods in Applied Mechanics and Engineering* 194.25 (2005), pp. 2859–2896.

[31] Alan N. Gent and Gary R. Hamed. "Peel mechanics". In: *The Journal of Adhesion* 7.2 (1975), pp. 91–95.

[32] Alan N. Gent and Gary R. Hamed. "Peel mechanics for an elastic-plastic adherend". In: *Journal of Applied Polymer Science* 21.10 (1977), pp. 2817–2831.

[33] Alan N. Gent and Gary R. Hamed. "Peel mechanics of adhesive joints". In: *Polymer Engineering & Science* 17.7 (1977), pp. 462–466.

[34] Animangsu Ghatak, L. Mahadevan, Jun Young Chung, Manoj K. Chaudhury, and Vijay Shenoy. "Peeling from a biomimetically patterned thin elastic film". In: *Proceedings of the Royal Society of London A: Mathematical, Physical and Engineering Sciences*. Vol. 460. 2049. The Royal Society. 2004, pp. 2725–2735.

[35] Michel Grediac, Frédéric Sur, and Beno^ıt Blaysat. "The Grid Method for In-plane Displacement and Strain Measurement: A Review and Analysis". In: *Strain* 52.3 (2016), pp. 205–243.

[36] Christian Greiner, Aránzazu del Campo, and Eduard Arzt. "Adhesion of bioinspired micropatterned surfaces: effects of pillar radius, aspect ratio, and preload". In: *Langmuir* 23.7 (2007), pp. 3495–3502.

[37] Alan A. Griffith. "The phenomena of rupture and flow in solids". In: *Philosophical transactions of the royal society of london. Series A, containing papers of a mathematical or physical character* 221 (1921), pp. 163–198.

[38] Rodney Hill. "Elastic properties of reinforced solids: some theoretical principles". In: *Journal of the Mechanics and Physics of Solids* 11.5 (1963), pp. 357–372.

[39] Arne Hillerborg, Mats Modéer, and P-E Petersson. "Analysis of crack formation and crack growth in concrete by means of fracture mechanics and finite elements". In: *Cement and concrete research* 6.6 (1976), pp. 773–781.

[40] John W. Hutchinson and Zhigang Suo. "Mixed mode cracking in layered materials". In: *Advances in applied mechanics* 29.63 (1992), p. 191.

[41] Charles Edward Inglis. "Stresses in a plate due to the presence of cracks and sharp corners". In: *Transactions of the Institution of Naval Architects* XLIV (1913), pp. 219–241.

[42] George R. Irwin. "Analysis of stresses and strains near the end of a crack traversing a plate". In: *Journal of Applied Mechanics* 24 (1957), pp. 361–364.

[43] George R. Irwin. "Fracture mechanics". In: *Structural Mechanics. Proceedings of the First Symposium on Naval Structural Mechanics*. Ed. by J.N. Goodier and N.J. Hoff. New York: Pergamon Press, 1960, pp. 557–594.

[44] David H. Kaelble. "Peel Adhesion: Micro-Fracture Mechanics of Interfacial Unbonding of Polymers". In: *Transactions of the Society of Rheology* 9.2 (1965), pp. 135–163.

[45] David H. Kaelble. "Theory and analysis of peel adhesion: bond stresses and distributions". In: *Transactions of the Society of Rheology* 4.1 (1960), pp. 45–73.

[46] David H. Kaelble. "Theory and analysis of peel adhesion: mechanisms and mechanics". In: *Transactions of the Society of Rheology* 3.1 (1959), pp. 161–180.

[47] Kevin Kendall. "Interfacial dislocations spontaneously created by peeling.(Adhesive joint strength)". In: *Journal of Physics D: Applied Physics* 11.11 (1978), p. 1519.

[48] Kevin Kendall. "The shapes of peeling solid films". In: *The Journal of Adhesion* 5.2 (1973), pp. 105–117.

[49] Kevin Kendall. "Thin-film peeling-the elastic term". In: *Journal of Physics D: Applied Physics* 8.13 (1975), p. 1449.

[50] J. J. Kruzic, R. L. Satet, M. J. Hoffmann, R. M. Cannon, and R. O. Ritchie. "The Utility of R Curves for Understanding Fracture Toughness Strength Relations in Bridging Ceramics". In: *Journal of the American Ceramic Society* 91.6 (2008), pp. 1986–1994.

[51] M. E. Launey and R. O. Ritchie. "On the fracture toughness of advanced materials". In: *Advanced Materials* 21.20 (2009), pp. 2103–2110.

[52] Feng Liang, Kumbhani Mayur, et al. "Fracture behavior of flock fiber reinforced laminar composite". In: *Journal of Materials Science and Engineering. B* 1.1B (2011), p. 1.

[53] Luca Lussardi and Matteo Negri. "Convergence of nonlocal finite element energies for fracture mechanics". In: *Numerical functional analysis and optimization* 28.1-2 (2007), pp. 83–109.

[54] C. Maurini, B. Bourdin, G. Gauthier, and V. Lazarus. "Crack patterns obtained by unidirectional drying of a colloidal suspension in a capillary tube: experiments and numerical simulations using a two-dimensional variational approach". In: *International Journal of Fracture* 184.1-2 (2013), pp. 75–91.

[55] Julia Mergheim, Ellen Kuhl, and Paul Steinmann. "A finite element method for the computational modelling of cohesive cracks". In: *International Journal for Numerical Methods in Engineering* 63.2 (2005), pp. 276–289.

[56] Lucas R. Meza, Satyajit Das, and Julia R. Greer. "Strong, lightweight, and recoverable three-dimensional ceramic nanolattices". In: *Science* 345.6202 (2014), pp. 1322–1326.

[57] J.C. Michel, H. Moulinec, and P. Suquet. "A computational scheme for linear and non-linear composites with arbitrary phase contrast". In: *International Journal for Numerical Methods in Engineering* 52.1-2 (2001), pp. 139–160.

[58] C. Miehe, F. Welschinger, and M. Hofacker. "Thermodynamically consistent phase-field models of fracture: Variational principles and multi-field FE implementations". In: *International Journal for Numerical Methods in Engineering* 83.10 (2010), pp. 1273–1311.

[59] He Ming-Yuan and John W Hutchinson. "Crack deflection at an interface between dissimilar elastic materials". In: *International Journal of Solids and Structures* 25.9 (1989), pp. 1053–1067.

[60] Lauren C. Montemayor, Lucas R. Meza, and Julia R. Greer. "Design and Fabrication of Hollow Rigid Nanolattices via Two-Photon Lithography". In: *Advanced Engineering Materials* 16.2 (2014), pp. 184–189.

[61] H. Moulinec and P. Suquet. "A FFT-based numerical method for computing the mechanical properties of composites from images of their microstructures". In: *IUTAM Symposium on Microstructure-Property Interactions in Composite Materials*. Springer. 1995, pp. 235–246.

[62] H. Moulinec and P. Suquet. "A numerical method for computing the overall response of nonlinear composites with complex microstructure". In: *Computer methods in applied mechanics and engineering* 157.1-2 (1998), pp. 69–94.

[63] Stefan Müller. "Homogenization of nonconvex integral functionals and cellular elastic materials". In: *Archive for Rational Mechanics and Analysis* 99 (1987), pp. 189–212.

[64] Matteo Negri and Christoph Ortner. "Quasi-static crack propagation by Griffith's criterion". In: *Mathematical Models and Methods in Applied Sciences* 18.11 (2008), pp. 1895–1925.

[65] JC Newman. "A review of chevron-notched fracture specimens". In: *Chevron-notched specimens: testing and stress analysis*. ASTM International, 1984.

[66] Michael Ortiz and A. Pandolfi. "A class of cohesive elements for the simulation of three-dimensional crack propagation". In: *International Journal for Numerical Methods in Engineering* 44.9 (1999), pp. 1267–1282.

[67] Michael Ortiz and A Pandolfi. "Caltech ASCI technical report 090". In: *Int. J. Numer. Methods Eng.* 44 (1999).

[68] Bing Pan, Kemao Qian, Huimin Xie, and Anand Asundi. "Two dimensional digital image correlation for in plane displacement and strain measurement: a review". In: *Measurement science and technology* 20.6 (2009), p. 062001.

[69] Anna Pandolfi and Michael Ortiz. "An efficient adaptive procedure for three-dimensional fragmentation simulations". In: *Engineering with Computers* 18.2 (2002), pp. 148–159.

[70] Earl R. Parker. "Brittle behavior of engineering structures". In: (1957).

[71] Kim Pham, Hanen Amor, Jean-Jacques Marigo, and Corrado Maurini. "Gradient damage models and their use to approximate brittle fracture". In: *International Journal of Damage Mechanics* 20.4 (2011), pp. 618–652.

[72] J.-L. Piro and M. Grédiac. "PRODUCING AND TRANSFERRING LOW-SPATIAL-FREQUENCY GRIDS FOR MEASURING DISPLACEMENT FIELDS WITH MOIRÉ AND GRID METHODS". In: *Experimental Techniques* 28.4 (2004), pp. 23–26.

[73] Daniel A. Ramrus and John C. Berg. "Enhancement of adhesion to heterogeneously patterned substrates". In: *Colloids and Surfaces A: Physicochemical and Engineering Aspects* 273.1 (2006), pp. 84–89.

[74] James R. Rice. "A path independent integral and the approximate analysis of strain concentration by notches and cracks". In: *Journal of Applied Mechanics* 35.2 (1968), pp. 379–386.

[75] Ronald S. Rivlin. "The effective work of adhesion". In: *Paint Technol* (1944), pp. 215–216.

[76] T. A. Schaedler, A. J. Jacobsen, A. Torrents, A. E. Sorensen, J. Lian, J. R. Greer, L. Valdevit, and W. B. Carter. "Ultralight metallic microlattices". In: *Science* 334.6058 (2011), pp. 962–965.

[77] Paul Sicsic, Jean-Jacques Marigo, and Corrado Maurini. "Initiation of a periodic array of cracks in the thermal shock problem: a gradient damage modeling". In: *Journal of the Mechanics and Physics of Solids* 63 (2014), pp. 256–284.

[78] ASTM Standard. "ASTM E1457 - 15: Standard Test Method for Plain-Strain Fracture Toughness of Metallic Materials". In: American Society for Testing Materials. 2016.

[79] ASTM Standard. "ASTM E399: Standard Test Method for Plain-Strain Fracture Toughness of Metallic Materials". In: American Society for Testing Materials. 2002.

[80] ASTM Standard. "D6272 - 17: Standard Test Method for Flexural Properties of Unreinforced and Reinforced Plastics and Electrical Insulating Materials by Four-Point Bending". In: American Society for Testing Materials.

[81] S. Suresh. "Fatigue crack deflection and fracture surface contact: micromechanical models". In: *Metallurgical and Materials Transactions A* 16.1 (1985), pp. 249–260.

[82] E. Tanné, T. Li, B. Bourdin, J.-J. Marigo, and C. Maurini. "Crack nucleation in variational phase-field models of fracture". In: *To be submitted* (2017).

[83] Jared Tracy, Anthony Waas, and Samantha Daly. "Experimental assessment of toughness in ceramic matrix composites using the J-integral with digital image correlation part I: methodology and validation". In: *Journal of Materials Science* 50.13 (2015), pp. 4646–4658.

[84] Harold M. Westergaard. "Bearing pressures and cracks". In: *Journal of Applied Mechanic* 6:A (1939), pp. 49–53.

[85] Max L. Williams. "On the stress distribution at the base of a stationary crack". In: *Journal of Applied Mechanics* 24 (1957), pp. 109–114.

[86] Shuman Xia, Laurent Ponson, Guruswami Ravichandran, and Kaushik Bhattacharya. "Adhesion of heterogeneous thin films I: Elastic heterogeneity". In: *Journal of the Mechanics and Physics of Solids* 61.3 (2013), pp. 838–851.

[87] Shuman Xia, Laurent Ponson, Guruswami Ravichandran, and Kaushik Bhattacharya. "Adhesion of heterogeneous thin films II: Adhesive heterogeneity". In: *Journal of the Mechanics and Physics of Solids* 83 (2015), pp. 88–103.

[88] Shuman Xia, Laurent Ponson, Guruswami Ravichandran, and Kaushik Bhattacharya. "Toughening and asymmetry in peeling of heterogeneous adhesives". In: *Physical review letters* 108.19 (2012), p. 196101.

[89] A. R. Zak and Max L. Williams. "Crack point stress singularities at a bi-material interface". In: (1962).

[90] Alan T. Zehnder. "Linear Elastic Stress Analysis of 2D Cracks". In: *Fracture Mechanics*. Springer, 2012, pp. 7–32.